

GENERATION OF CROSSFLOW VORTICES IN A THREE-DIMENSIONAL
FLAT PLATE FLOW

Thesis submitted to the Faculty of the
Virginia Polytechnic Institute and State University
in partial fulfillment of the requirements for the degree of
MASTER OF SCIENCE
in
ENGINEERING MECHANICS

by
LAWRENCE GUIER YEATES

APPROVED:

W.S. Saric, Chairman

T. Herbert

D. Telionis

October, 1984
Blacksburg, Virginia

GENERATION OF CROSSFLOW VORTICES IN A THREE-DIMENSIONAL FLAT-PLATE FLOW

BY

LAWRENCE G. YEATES

(ABSTRACT)

The ability to generate a crossflow vortex pattern on a swept flat plate, that is typical of swept-wing flows, is presented. A swept flat plate with an elliptic leading edge is mounted vertically in the VPI&SU Stability Wind Tunnel opposite to a swept wall-bump; along with floor and ceiling fairings that duplicate the inviscid streamlines. The resulting pressure gradient over the plate produces a crossflow vortex structure.

Detailed three-dimensional measurements, made within the boundary layer using hot-wire anemometry, are supplemented with different flow-visualization techniques. Freestream measurements are carried out to find the variation of the velocity vector along the model and comparisons are made with the theory showing good agreement. Spanwise measurements are conducted within the boundary layer and show a steady vortex structure. Boundary-layer profiles are taken using both a straight-wire and slant-wire probe in order to obtain the

variation of the velocity vector in the region. The components parallel and perpendicular to the freestream velocity vector are extracted, and the perpendicular component is called the crossflow profile. These profiles are compared to the theory. Shape factors and crossflow Reynolds numbers are obtained and analysed.

Two types of flow-visualization techniques are used in the tests. One is the "smoke-wire" technique, where streaklines inside the boundary layer are visualized. This method is not successful in visualizing any vortex structure in the boundary layer. Therefore, the second method was employed: a sublimation technique using trichlorethane and naphthalene is used to visualize the variation of the surface shear stress. A uniform pattern of streaks aligned approximately in the potential flow direction is observed. This pattern has a wavelength on the order of one centimeter which agrees quite well with the theoretical model.

ACKNOWLEDGEMENTS

The author would like to express special thanks to Dr. William S. Saric, advisor and teacher, for his encouragement, motivation and insight throughout the whole period of this work. Also, to everyone involved in the project, for their help and cooperation.

Thanks to Bret Farmer and Skip Alford for their help in the construction of much of the experimental apparatus. Thanks to German Santos, Shyang-Lin Kuo and Jeff Crouch for their endless hours of assistance in the wind tunnel. Thanks to Jeff Carter for his help in developing much of the computer hardware and software. Thanks to Kay Herbert for the many nights he spent on the computer running the theoretical codes for this work. Thanks to Gayle Rose for her help in the software development used for data collection and data reduction. Also thanks to Dr. W. Pfenninger for his helpful suggestions and insight into this problem. Special thanks to Charlotte Hawley for being there until the end. Lastly, thanks to my parents for their guidance and encouragement during this work.

This work was made possible by the support from NASA Grant Number NAG-1-280.

TABLE OF CONTENTS

ABSTRACT	ii
ACKNOWLEDGEMENTS	iv
 <u>Chapter</u>	
	<u>page</u>
1. INTRODUCTION	1
1.1 GENERAL	1
1.2 CROSSFLOW INSTABILITY	2
1.3 CURRENT RESEARCH	3
1.4 MOTIVATION FOR CURRENT WORK	7
2. EXPERIMENTAL APPARATUS AND WIND-TUNNEL FACILITY	11
2.1 WIND-TUNNEL FACILITY	11
2.2 THE SWEEPED FLAT PLATE	14
2.3 WALL BUMP	17
2.4 TRAVERSE MECHANISM	20
2.5 HOT-WIRE STING	21
2.6 SMOKE WIRE	23
2.7 VIBRATING RIBBON	24
3. EXPERIMENTAL PROCEDURES AND RESULTS	27
3.1 MEASUREMENT TECHNIQUES	27
3.2 PRESSURE MEASUREMENTS	28
3.3 MEAN-FLOW MEASUREMENTS	31
3.3.1 Inviscid Flow	31
3.3.2 Boundary-Layer Profiles	33
3.3.3 Spanwise Measurements of Vortices	38
3.4 FLOW VISUALIZATION	39
4. CONCLUSIONS	43
REFERENCES	45

Appendix

	<u>page</u>
A. ELECTRONIC EQUIPMENT	48
B. COMPUTER CODES	55

Chapter I

INTRODUCTION

1.1 GENERAL

The transition process from laminar to turbulent flow over a swept wing is still a very important topic in fluid mechanics today. Transition on a swept wing is generally accepted to be the uncontrolled growth of small disturbances in the boundary layer. In flight conditions the flow is generally turbulent over the wings of the aircraft and this turbulent boundary layer can account for up to 50% of the total drag on the vehicle during cruise. If, however, the aircraft could operate with a laminar boundary layer over the wings, the result would be reduced skin friction and heat transfer, which in turn reduces the fuel consumption of the vehicle. This is essentially the motivation for understanding the transition process in today's energy-conscious society.

The idea of Laminar Flow Control (LFC) (Pfenninger, Reed, & Dagenhart 1980) has become a major topic of research today. Research has been conducted in this case using weak suction on the wing surface where the suction delays the growth of disturbances in the boundary layer thus delaying transition. The theoretical work of Reed and Nayfeh (1984) and experimental work of Reynolds and Saric (1984) put this concept on a firm foundation for two-dimensional flows.

1.2 CROSSFLOW INSTABILITY

The flow over the swept-wing is three-dimensional, due to the wing sweep. This type of flow can break down into turbulence by three different mechanisms. They are leading edge contamination, streamwise instability, and the topic of this paper, crossflow instability. Figure 1.1 shows the top view of a typical swept-wing with the coordinate system used in this discussion, and a streamline pattern. Leading-edge contamination occurs along the attachment line and is caused by disturbances that propagate along the wing edge. Due to the small sweep angle and small leading edge radius in this experiment, leading-edge contamination is not considered. Streamwise instability is associated with the U component of flow and is quite similar to two-dimensional flows, where Tollmien-Schlichting (T-S) waves generally develop from the background freestream disturbances and lead to three-dimensional structures that break down to turbulence. This generally occurs in zero or positive pressure-gradient regions. The focus of this paper is on the crossflow instability, associated with the W component of flow, which occurs in strong negative pressure gradient regions. In the leading-edge region both the surface and flow streamlines are highly curved. The pressure gradient and wing sweep deflects the inviscid flow streamlines, and viscous effects cause crossflow in the boundary layer, which is the development of a velocity component inside the boundary layer that is transverse to the freestream velocity vector. The profile is shaped similar to a bell curve, with a maximum velocity

somewhere in the middle region, going to zero on the plate surface and at the boundary-layer edge. This crossflow profile exhibits an inflection point (a condition which is known to be unstable at large Reynolds numbers) causing so-called crossflow vortex structures to form with their axes in the streamwise direction. These crossflow vortices all rotate in the same direction.

1.3 CURRENT RESEARCH

In the past ten years considerable progress has been achieved in calculating the stability characteristics of three-dimensional flows. The state-of-the-art transition prediction method still involves linear stability theory coupled with an e^N transition prediction scheme. This method was proposed originally by Smith & Gamberoni (1956) and Van Ingen (1956) who used it in two-dimensional and axi-symmetric flows. They show that transition occurs when N approaches 10. That is the amplitude of the disturbance at transition is e^{10} times larger than the amplitude at its initial instability. The method was later extended to three-dimensional flows by Srokowski & Orszag (1977), Nayfeh (1980) and Cebeci & Stewartson (1980). This work was further developed by Malik, Wilkinson & Orszag (1981) to include curvature, where they show for the rotating disk that streamline curvature and Coriolis forces have a very stabilizing effect on disturbances. They obtain an N factor of approximately 11 in the transition correlation scheme which seems quite reasonable and matches the N factors of two-dimensional flows for

transition. Malik & Poll (1984) extended the stability analysis of three-dimensional flows, analysing the flow over a yawed cylinder, to include curvature of the surface and streamlines. They show that curvature has a very stabilizing effect on the disturbances in the flow. This was compared with experimental results of Poll (1984) which showed good agreement with the transition prediction scheme. They also find that the most highly amplified disturbances are travelling waves and not the stationary waves. This is in disagreement with Malik, Wilkinson & Orszag (1981) who showed for the rotating disk that the fixed disturbances produced the highest amplification rates. Here again Malik & Poll (1984) obtain good agreement with Poll's (1984) recent experimental work where he identifies a highly amplified travelling wave around one khz near transition. Malik & Poll (1984) obtain N factors for the fixed frequency disturbances between 11 and 12 which agreed with the work of Malik, Wilkinson & Orszag (1981) on the rotating disk. In both cases (the disk and cylinder) when the extra terms, involving curvature and Coriolis effects, were omitted in the stability analysis, the N factors were much larger and initially placed doubt on the validity of the transition prediction method.

Michel, Arnal & Coustols (1984) develop transition criteria for incompressible two and three-dimensional flows. Particularly for the case of a swept wing with infinite span. They correlate transition onset on the swept wing using three parameters, a Reynolds number based on the displacement thickness in the most unstable direction of

flow, the streamwise shape parameter, and the external turbulence level. However, they simplified the problem by not including curvature effects and assuming locally parallel flow. Even with these simplifications, the comparison with experiment showed good agreement.

Recent experimental work of Poll (1979), (1983) focuses on the leading edge contamination problem. This problem was investigated experimentally by Pfenninger (1977) and Gregory, Stuart & Walker (1965), however the causes of leading-edge contamination were never completely investigated or understood. Poll's (1979) first work studied the effect of placing trip wires normal to the attachment line. He defines a length scale η equal to the square root of

$$\frac{\nu}{(dU_e/dx)_{x=0}}$$

where U_e is the edge velocity in the streamwise direction, ν is the kinematic viscosity and x is in the chord direction. He uses the parameter d/η where d is the diameter of the wire. From this parameter he determined a maximum ratio of 1.55 below which the wire feeds disturbances along the attachment line until turbulence bursts occur. Above this value he discovered that the wire introduces turbulent bursts directly at the trip wire. There is a value of d/η equal to 0.8 or less where the wire has no effect on the transition process. Poll's (1983) recent work defines a Reynolds number based on

the edge velocity V_e parallel to the leading edge and the length scale mentioned earlier. Based on this definition he obtained a critical Reynolds number $Re_c=250$, below which propagation of disturbances along the attachment line does not occur.

The current experimental work of Poll (1984) focuses on the crossflow instability where he shows that increasing yaw has a very destabilizing effect on the flow over a swept cylinder. He characterizes the instability in two ways. One by the fixed disturbances visualized by either surface evaporation or oil-flow techniques. These disturbances are characterized by regularly spaced streaks aligned approximately in the potential flow direction, leading into a "saw-tooth" pattern at the transition location. The other is a large-amplitude high-frequency harmonic wave at frequencies near one khz. At transition near the wall surface he obtains disturbance amplitudes greater than 20% of the local mean velocity. Initially he tries to use two parameters to predict transition. They are the crossflow Reynolds number (Re_{cf}) and a shape factor based on the streamwise profile. However, based on the results of his research, the two parameters alone are not enough to predict transition, and that one needs at least three parameters to accurately describe the crossflow instability.

Michel, Arnal, Coustols & Juillen (1984) present some very good experimental results on the crossflow instability, conducted on a swept airfoil model. By surface visualization techniques they show regularly spaced streaks that are aligned practically in the potential flow

direction, with a "saw-tooth" pattern near the transition area. They perform hot-wire measurements on the stationary waves. Their results show a spanwise variation of the boundary layer before transition that became chaotic in the transition region. The variations are damped in the turbulent region. From their boundary-layer measurements they deduce that the ratio of λ / δ is nearly constant and equal to 4, where λ is the spanwise wavelength and δ the physical boundary-layer thickness. They also find a small peak in the spectra around one khz like Poll, which is due to a streamwise instability. In addition to this they provide some theoretical work on the secondary velocities, and show counter rotating vortices in the streamwise direction. However, when these components are added to the mean velocities the vortices are no longer clearly visible. Even with all this progress there are very little experimental data with which to compare the theoretical models.

1.4 MOTIVATION FOR CURRENT WORK

A major unanswered question concerning swept-wing flows is the interaction of these crossflow vortices with T-S waves. If the vortex structure continues back into the mid-chord region where T-S waves are amplified, some type of interaction could cause premature transition. It is well known that streamwise vortices in a boundary layer strongly influence the behavior of other disturbances. Nayfeh (1981) showed that Görtler vortices produce a double-exponential growth of T-S waves. Herbert & Morkovin (1980) showed that the presence of T-S

waves produce a double-exponential growth of Görtler vortices, while Floryan & Saric (1980) showed a similar behavior for streamwise vortices interacting with Görtler vortices. Reed (1984) analyzed the crossflow / T-S interaction in the leading-edge region by using a parametric-resonance model. She showed that the interaction of the crossflow vortices with T-S waves produces a double exponential growth of the T-S waves. The results of Reed (1984) clearly show the need to experimentally study problems of this kind.

The objective of this experimental program is a basic investigation of the crossflow instability. Future work will cover the crossflow / T-S wave interaction and LFC using suction panels. This work is conducted on a flat-plate model with a swept leading edge using a contoured wall bump opposite the plate to produce a chordwise pressure gradient along the plate. This configuration produces a typical crossflow vortex pattern on the flat plate. With this simple geometry, detailed boundary-layer measurements are conducted. The collected mean-flow data are then compared to the theory. The theory in this case is a three-dimensional boundary-layer code of Kaups & Cebeci (1977). This code solves the laminar, compressible boundary-layer equations for a tapered, swept wing with mass transfer under the conical-flow assumptions.

There are some very good reasons for using the flat plate, wall-bump arrangement instead of an airfoil-shaped model. A sizable investment is required to obtain a quality airfoil model. Also, a new

traverse mechanism would need to be devised for tracking the contour of the airfoil. It should be noted that the boundary layer over the airfoil model is quite a bit thinner than the boundary layer over the flat-plate. The smaller boundary layer restricts the use of hot-wire anemometry and severely limits the amount of obtainable data in the region. Furthermore, selection of a specific airfoil shape would severely limit the range of possible pressure distributions. Since it is important to study a range of C_p distributions in this type of research, one needs a new model for each C_p distribution. On the other hand, the swept flat plate uses many pieces of apparatus already developed at VPI&SU, such as the leading edge and traverse mechanism. The major advantage in the swept flat plate is the wall bump. It is relatively inexpensive to build and by modifying the shape of the bump the pressure distribution attained on the plate is modified. So the swept flat plate, wall-bump setup is a more economical solution to the study of swept-wing flows and eliminates many of the problems encountered with the airfoil model.

Chapter two of this paper gives a detailed description of the apparatus and a complete layout of the test section. Many of the same experimental capabilities refined by Reynolds & Saric (1984), such as the hot-wire sting and vibrating ribbon, are employed, with minor modifications, in this work. Chapter three gives a detailed discussion on data collection, its procedures and some results. The data collection include pressure measurements, freestream measurements, boundary-

layer measurements and flow visualization. The procedures for each of these measurements are described in some detail. Chapter four is a discussion of the results with conclusions. A detailed description of the instrumentation is given in Appendix A, and a brief description of the computer codes used for theoretical models are given in Appendix B.

Chapter II

EXPERIMENTAL APPARATUS AND WIND-TUNNEL FACILITY

2.1 WIND-TUNNEL FACILITY

The experiments are carried out in the VPI&SU Stability Wind Tunnel. This wind tunnel originally was a NACA facility located at Langley Field in Hampton, Virginia. Constructed in 1940, the facility is designed to provide a very low turbulence-level flow for conducting dynamic stability measurements. The wind tunnel was moved to VPI&SU and reconstructed in 1958. Recent studies (Reynolds & Saric 1984) indicate that the tunnel is able to provide very good flow quality. The freestream turbulence levels range between .02% to .04% in the range of test velocities. A list of freestream velocities with corresponding turbulence levels is shown below.

U_{∞} (m/s)	$ u /U_{\infty}$ (%)
9	.018
12	.018
15	.022
20	.028
30	.045

The facility is a closed-loop tunnel and has an air-exchange tower which opens to the atmosphere. A plan view of the facility is shown in figure 2.1. The air-exchange tower is located downstream of the fan and motor assembly and uses a boundary-layer bleed on the entry flow. The continual air exchange provides for temperature stabilization since the flow-loop is otherwise closed and heat exchangers are not used. This air-exchange tower and the external flow-loop configuration have the disadvantages of allowing the environmental conditions to influence the flow conditions. This is overcome by avoiding testing during periods of extreme temperature change and/or gusty wind conditions. During stable environmental conditions the facility provides a remarkably stable mean-flow velocity with no tendency to drift over time, even at very low flow velocities.

The flow is driven by a 4.3m diameter propeller that has eight constant pitch blades. Power for the fan is provided by a 450KW d.c. motor. This system is capable of providing stable, low-turbulence flow in the test section for the velocity range of 4.6m/s to 67m/s. Speed control is accomplished manually by a coarse and fine rheostat control. The fan-motor assembly is mounted on an isolated foundation. Electrical power for the d.c. motor is supplied by a Westinghouse Model No. 28767 motor-generator. The motor-generator is also mounted on its own foundation. However, the generator rotational speed of 900 r.p.m., or 15 Hz, is known to be a source of vibration in the test section.

Turning vanes are located at each corner of the tunnel circuit in order to maintain uniform flow. The turning vanes have streamlined cross sections and are spaced every 0.30m along the diagonal of each corner, except the corner preceding the turbulence screens, where the spacing between vanes is 0.076m. This last set of turning vanes is particularly important in reducing the existing large-scale turbulence in the settling chamber and in this sense functions somewhat like a large-scale honeycomb. The finer vane spacing in the last corner also reduces any large-scale vorticity which may be introduced in turning the flow. The relatively low air velocities in the settling chamber and through the turbulence screens allow the remaining large-scale turbulent eddies to be dissipated. The seven turbulence screens located in the 5.5m by 5.5m settling chamber are of 0.2mm diameter stainless steel wire with a mesh size resulting in an open-area ratio of 0.6. Experiments performed to determine optimum damping-screen mesh size for low-turbulence experiments (Bradshaw 1965), suggest that screens should have an open-area ratio greater than 0.57. Each 5.5m square screen panel is constructed from three 1.83m x 5.5m screens joined together. The two seams in each screen panel are approximately 2mm wide. The screen panel farthest downstream has horizontal seams and alternate upstream panels are rotated 90 degrees. This results in four horizontal and three vertical sets of seams. The screens are drawn very tight and held by clamps around the inside perimeter of the settling chamber walls. The spacing between screens is 0.15m. The

screen clamps are offset from the settling chamber wall, which results in a 25mm space around the perimeter of the screens. Due to the screen blockage, a wall jet is created as the flow leaves the turbulence screens. The settling chamber extends past the screens and allows the remaining small-scale turbulence to dissipate naturally before entering the nozzle. The flow undergoes a 9:1 area contraction as it passes through the nozzle and into the test section.

The test section is 7.3m long with a constant square cross section of 1.83m. Since there is no allowance for the growth of the wall boundary layers, a slight negative pressure gradient of approximately $C_p = 0.3\%$ per meter is present. Since the zero-pressure state is in the settling chamber, the test section is enclosed in an airtight control room. Thus, the air leakage into the test-section flow is minimized. The diffuser angle is 3 degrees per side, and for most tests vortex generators are located at the entrance to ensure efficient diffuser operation.

2.2 THE SWEPT FLAT PLATE

The swept flat-plate model, constructed by Brunswick Corporation in Marion, Virginia is 1.83m x 3.7m with a 25-degree sweep angle. The model is a laminated panel that consists of a 19mm-paper-honeycomb core sandwiched between two, 1mm 6061-T6 aluminum sheets, giving it an overall thickness of 21mm. The construction provides a strong and lightweight model with a very flat test surface. Four cut-away

locations are prefabricated into the model to allow for porous suction panels. Since these panel openings are cut during the fabrication of the model, the edge contour around the cut-away locations is very smooth and a very flat junction is obtained between the model and panels. For the present experiments, the panel openings are covered with smooth aluminum inserts. These can be easily removed and the porous panels inserted for future suction experiments. Figure 2.2 is a diagram of the plate and the cut-away locations. 112 pressure ports are installed to measure static pressure in the span and chordwise directions on the plate. The location of these ports are shown in figure 2.3. A pressure port consists of a 6.3mm diameter cylindrical aluminum insert with an orifice at one end and a copper tube at the other end. This arrangement allows for easy attachment of pressure tubing to the backside of the plate for static-pressure measurements without disturbing the flow. The pressure-port inserts are machined with a 0.01-0.02mm interference and are press-fit into the plate and then secured by potting them on the backside with fiberglass resin. Figure 2.4 is a diagram of the pressure port and figure 2.5 is a cut-away view showing the pressure port installed into the plate with the pressure tubing coming off the backside.

The pressure tubing is then connected to a 48-port manifold and in turn connected into a scanning valve with a ± 690 Pa differential pressure transducer. The transducer voltage is fed into the MASSCOMP 560 computer and converted into a C_p reading which is then plotted on the six-pen HP-7475A plotter.

Along with the pressure ports, other holes are drilled in the plate to provide for smoke-wire fixtures, magnet mounts, and proximeter-probe inserts. The locations of these are shown in figure 2.6. Once these modifications are accomplished the plate is sanded to remove any irregularities in the surface. It is finally finished by using 600-grit sandpaper and polishing compound; then a coat of wax is applied to protect the surface from oxidation. Irregularities in the test surface show no local variations greater than 0.1mm and generally less than 0.03mm.

A 0.34 x 1.83m tapered leading edge is mounted onto the front of the plate which gives a total model length of 4.0m. The leading edge is shown in figure 2.7. The leading edge has an elliptical profile with a ratio of major to minor axes of 67:1. This leading edge profile is chosen to minimize the stagnation-point pressure rise and yet be insensitive to leading-edge separation at slight angles of attack. The elliptical profile is machined from a single piece of aluminum using a numerically controlled milling machine. Tolerances for the profile shape are $\pm 0.03\text{mm}$ near the stagnation region and $\pm 0.1\text{mm}$ near the swept flat-plate junction. A surface finish of $8\mu\text{m}$ r.m.s. is obtained by hand polishing. At the leading-edge plate junction, the leading edge is parallel to the front surface of the plate. Because of the different thermal-expansion coefficients of the two materials, a slight step or gap results at the junction. This step or gap is generally less than 0.02 - 0.05mm and is easily faired by using a polyester patching compound (Bondo).

A trailing-edge flap is added to the end of the swept flat plate in order to control the position of the attachment line on the leading edge. The flap is used to balance the wind-tunnel blockage between each side of the plate in order to control leading-edge separation. The trailing-edge flap is adjustable from zero deflection to a maximum of 33 degrees toward the test side of the plate and has a tapered, sharp trailing edge. The flap is used in this experiment mainly to control the blockage so as to obtain a constant spanwise pressure distribution. Due to the favorable pressure gradient, leading-edge separation is not a problem.

2.3 WALL BUMP

A major part of this work is the design and construction of the wall bump which encloses the three-dimensional traverse mechanism. The wall bump is designed to provide adequate crossflow on the swept plate to simulate flow over a swept wing. Design constraints are imposed to incorporate as much of the existing equipment as possible, as long as these constraints do not conflict with the requirements of the tests. Some of the equipment that is reused includes the leading edge, traverse mechanism, sting, rails for the traverse mechanism, brackets for the plate, and the trailing-edge flap. Using the existing leading edge restricts the sweep angle to approximately 25 degrees or more which is in the range of similar experimental work being carried out at NASA. The only real problem with using the same traverse set up is

that the thickness of the bump has to be large enough to both enclose the traverse and allow for the normal operation of it.

Once these requirements are incorporated into the design, the test-section configuration, without the wall bump, is input into the Inverse Panel-Method Code (May & Saric 1983). This code is a modification of a panel-method code written at NASA Langley Research Center by D.R. Bristow (1980). The Inverse Panel-Method Code is used to calculate the general shape of the bump for a given C_p distribution over the plate. A brief description of the Inverse Panel-Method Code is given in Appendix B, section B.1. Once the design is fixed for the wall bump, the Panel Code (Bristow 1980) is used to calculate the C_p distribution over the test side of the plate for the actual wall-bump geometry. Then a comparison is made between the designed C_p distribution and the actual C_p distribution to make sure the designed wall bump will provide the desired C_p distribution on the test plate. The Panel Code is also described in Appendix B, section B.1. Based on these designs and calculations, a layout of the test section configuration is shown in figure 2.8. This design provides a C_p distribution quit similar to an airfoil, with a very sharp negative pressure rise initially, gradually leveling off, then an increasing pressure region near the end of the model. A very important characteristic of the pressure distribution is that it includes a large area in the middle of the chord where the pressure is constant and the crossflow / T-S interaction can be studied. The calculated C_p distribution from the Panel Code is shown in figure 2.9.

The basic materials for the bump are plexiglass and aluminum angle, except for the contoured section which is constructed out of plywood. The contoured section of the bump is framed out of 16mm plywood and then a 3mm sheet of birch plywood is glued and nailed to the contour of the frame. It is then filled, sanded, and painted to provide a very smooth surface. The middle section of the bump, or the wall-bump extension is 2.5m. long and is designed to provide a zero pressure gradient region on the plate where most of the measurements are made. This section of the bump is shown in figure 2.10. It is constructed of 9.5mm plexiglass and framed with aluminum angle. In the middle of the extension, a slot 0.3 x 1.5m is cut and a 0.56 x 1.58m sheet of plexiglass is placed behind this slot and held in place by teflon guides that allow the insert to move up and down. The slot is reinforced by 6 x 25mm aluminum frame. A drawing of the insert is shown in figure 2.11. In this insert, a 46mm chordwise slot is cut to allow the sting (arm of the traverse) to travel back and forth along the plate. In this slot, a "zipper insert" is placed to eliminate leakage into the test section. The "zipper insert" is made from nylon canvas material that is cut to fit in the frame of the slot and secured by bolts along the length of the slot. A zipper is sewn into the middle of the nylon along the length of the material, then the material is cut to allow the sting to protrude through the zipper. Two sliding pieces that open and close the zipper are attached to the sides of the sting. In this way the zipper is closed everywhere except along the sting. As the

sting moves in the chord direction, one sliding piece opens up the zipper to allow the sting to move forward and the other sliding piece closes the zipper behind. This design works well and does a very good job of eliminating air leakage into the test section. Counter weights are attached to the plexiglass insert to allow normal movement of the traverse with little extra resistance on the stepper motors. Consequently the z-stepper motor easily moves the wall bump insert up and down during movement of the traverse. Due to the insert, traverse movement is restricted to approximately one meter in the chord direction and 0.2m in the span direction.

The final part of the bump angles back to the test section wall, still swept at 25 degrees. This is shown in figure 2.12. It is 1.5m long and constructed out of 9.5mm plexiglass and aluminum angle. It provides a very gradual decrease in the mean velocity, and the delay of separation on the bump.

2.4 TRAVERSE MECHANISM

The three-dimensional traversing mechanism for movement in the x-, y-, and z-directions is shown in figure 2.13. The swept flat plate is mounted in the vertical plane shown also in figure 2.13. The x-traverse guide rods are mounted on the floor and ceiling of the tunnel and are parallel to the tunnel side walls. The device has the following capabilities:

	x(chordwise)	y(normal-to- the-wall)	z(spanwise)
Total travel	1000 mm	100 mm	250 mm
Minimum step size	0.25 mm	0.007 mm	0.10 mm

With boundary-layer thicknesses of the order of 4mm, it is very easy to obtain over 100 measurements across the boundary layer. The MASSCOMP 560 automatically locates and moves the probe within the boundary layer for any series of measurements. The x-traverse is driven by a stepping motor through a chain drive. The y-traverse is operated by a stepping motor that drives a precision lead screw (2.54mm lead, 0.9 degrees per step). The z-traverse is driven by a geared stepping motor connected to a pair of precision lead screws. All three traverses move along precision ground steel rods using self-aligning ball bushings. This support configuration provides low-friction, linear motion and accurate positioning with a minimum of side-to-side motion.

2.5 HOT-WIRE STING

The hot-wire sting is mounted on the y-traverse sliding block and extends 0.61m to the side and 0.61m ahead of the traversing mechanism as shown in figure 2.13. Because almost all hot-wire measurements are taken in the thin boundary-layer region near the model, it is necessary

to minimize the probe vibration. At the same time, the sting thickness has to be kept small to reduce its drag. In order to obtain the needed rigidity and thin profile, a laminated-composite construction is used. The sting was constructed at VPI&SU and consists basically of two parts: the root and the extension. The root of the sting, which attaches to the y-traversing mechanism, is a laminated Kevlar composite. This consists of 20 layers of woven, pre-impregnated Kevlar material, which has an overall post-cure thickness of 4.76mm after being subjected to a high temperature press. The extension arm which holds the probe extension tube, is a laminated-graphite composite that is layered-up from 21 layers of pre-impregnated, monodirectional graphite material. To obtain maximum strength in bending as well as torsion, the plies are layered with the following filament orientation: 0 , 90 , +45 , -45 , 90 , 0 degrees. The resulting post-cure thickness of the graphite extension is 3.17mm after being subjected to a high-temperature press. The two parts of the sting, the root and the extension, are butted end-to-end and laminated between two aluminum facing sheets, which results in a total thickness at the root of 6.35mm. The hot-wire probe is mounted at the end of 4.76mm o.d. stainless steel tube, which in turn is mounted at the end of the sting by a pen-vise arrangement. This sting configuration proves to be quite effective. The degree of vibration encountered is found to be well within tolerable limits, and interference with the hot-wire measurements is not a problem.

2.6 SMOKE WIRE

The smoke wire is patterned after the well-known I.I.T model of Corke, Koga, Drubka & Nagib (1974) except that it is to operate within a 4mm boundary layer. A drop of oil is made to glide down a wire which coats the wire at the same time. The application of a voltage across the wire causes the oil to burn off in the filaments. Figure 2.14 illustrates the present VPI&SU model. This unit has the advantage of accurately locating the wire parallel to the surface at different fixed distances away from the model. This is done through two cap screws that are mounted to the support tubes and rest against the plate. The wire displacement away from the model is measured with "feeler" gauges. Four smoke-wire locations are installed on the model, but there is no practical limit on the position of the smoke wire. A predetermined wire tension can be used with an appropriate take-up spring.

A timing circuit with two 555 timing chips and two 741 op-amp chips provide the delay between the wire voltage and the shutter release. A Mamiya RB-67 camera equipped with either a 120 film holder or a Polaroid film holder is used. Either a 90mm f3.8 Sekor lens or a 180mm f4.5 Sekor lens with between-the-lens shutters are used. A 70mm x 70mm Polaroid-667 print (ASA 3000) is exposed until the appropriate test conditions are met. Then, without losing any exposures, the Polaroid back is interchanged with the 120 film holder and a 60mm x 70mm Tri-X negative (ASA 400) is exposed.

Subsequently, 200mm x 250mm enlargements are made from the negatives.

2.7 VIBRATING RIBBON

The source of the disturbances introduced into the boundary layer is a thin metallic strip which, when placed in a constant magnetic field, oscillates at the frequency of the electrical current passing through it. The ribbon material used is a stainless steel alloy 0.025mm thick and is obtained in precut widths of 2.5mm. In previous experiments a spring-tempered, phosphor-bronze alloy of the same dimensions was used. For additional information see Reynolds (1979). However, the ribbon tensions needed in this experiment are too great for the phosphor-bronze alloy and the stronger stainless steel alloy is needed. Sixty-four electromagnets are mounted on the back of the plate in two parallel rows. The two rows of magnets have opposite polarity, producing uni-directional field lines perpendicular to the magnetic strip. The ribbon tension is applied using a spring scale which is accurate to within 1 Newton. A tension of 25 Newtons is found to be satisfactory at freestream velocities of 15m/s. Ribbon clamps on the back of the model hold the ribbon in tension and provide electrical contact.

The free-vibration length of the ribbon can be varied from 400mm to 900mm, and this length is centered at midspan of the model. However, the ribbon tension required for the ribbon to oscillate in a

first-mode of vibration increases as the free-vibration length increases. For this experiment due to the configuration of the ribbon and magnets at a 25 degree angle from vertical, and the nature of the boundary layer flow, the span of the ribbon is shortened to approximately 400mm requiring only the middle 30 magnets to be used. Each end of the vibrating length of the ribbon is held a distance of 0.2mm from the plate by glass rods, and the remaining stationary portion of the ribbon is isolated electrically from the plate by a single layer of cellophane tape. Measurements of the ribbon amplitude and frequency as a function of the magnetic field strength and ribbon current provide a direct indication of the disturbances introduced by the ribbon. These measurements are accomplished by means of an inductance probe which is mounted in the model surface, directly under the ribbon at midspan. A description of the probe is given in Appendix A, section A.14.

A number of characteristics are important concerning the type of disturbances introduced by the ribbon. Special care is taken to apply a uniform tension and to avoid any static friction in the system. Teflon guides are used at the top and bottom of the plate to minimize static friction and help obtain a uniform tension on the ribbon. Serious problems with a ribbon twisting mode can occur if one is not careful. It is only through these methods that one can operate at freestream velocities of 15m/s. Measurements of the peak ribbon amplitude and spanwise phase are an indication of the uniformity of displacement. A spanwise plot of the ribbon phase relative to the driving signal

indicates a first-mode ribbon vibration. Spectrum analysis of the ribbon vibration also indicates that harmonics of the fundamental driving frequency are not present at the low ribbon amplitudes used in this experiment. For each installation of the ribbon, linear and nonlinear frequency response curves are generated in order to verify uniform, first-mode oscillation.

Frequency spectra of typical oscillator outputs show the presence of harmonics on the order of 1% of the fundamental. Since these harmonics lie closer to the ribbon resonant frequency, they are amplified more on the ribbon and can appear to the same order as the fundamental in the flow. Fourth-order low-pass filters are used to minimize the unwanted harmonics to a level well below $10e^{-3}$ of the fundamental. Even with this precaution, the ribbon excites the harmonics to some extent.

Chapter III

EXPERIMENTAL PROCEDURES AND RESULTS

3.1 MEASUREMENT TECHNIQUES

The objectives of these experiments are to visualize and measure properties of crossflow vortices. The visualization is carried out by the smoke-wire technique (Weber et al. 1980), in which wave patterns in the boundary layer are observed, and a sublimation method where surface flow patterns are studied. Various properties of the flow are measured in a pre-programmed fashion by hot-wire anemometry, using the MASSCOMP 560 computer.

Three independent constant temperature anemometer channels are used to measure the disturbance and mean flow velocities. Each channel consists of a DISA 55D01 Constant Temperature Anemometer (CTA), and a DISA 55D10 Linearizer. A schematic of the hot-wire anemometry layout is shown in figure 3.1. The linearizers are used to obtain a voltage signal proportional to the velocity being measured. Hot-wire probes have to occasionally be relinearized due to temperature fluctuations since they are not temperature compensated. The calibration of the probe to obtain a linear voltage output proportional to velocity is done by the MASSCOMP 560 computer. The MASSCOMP is described in Appendix A, section A.3.

The basic type of hot-wire probe used in the experiment is the boundary-layer probe which enables measurements to be taken very

close to the surface of the model. The probe consists of a 3mm long, 5 μ m diameter platinum-plated tungsten wire with gold plated ends. The sensing portion of the wire is 1.25mm long, ($L/D = 250$) isolated from the support prongs by the gold coated portion of the wire at each end. A sketch of both the straightwire and slantwire probes is shown in figures 3.2 and 3.3.

3.2 PRESSURE MEASUREMENTS

Some preliminary measurements are needed in order to match the experiment with the theoretical model. The primary requirement of the theory, due to the conical-flow assumption, is to obtain a uniform chordwise pressure gradient with constant pressure in the span direction over the flat plate. In the experiment, the boundary-layer flow must be laminar over the plate in the region of interest, implying minimal freestream turbulence and no leading-edge contamination. Due to the low velocities and small sweep angle, leading edge contamination is not a problem. Through the sublimation technique, turbulent wedges are observed at the floor and ceiling junction of the leading edge, but there are no signs that these disturbances propagate along the edge of the plate. However, the mean-flow quality was a major obstacle to control in this experiment, due to the large amount of blockage imposed in the test section. An unsteadiness in the freestream was caused by separation off the floor contour at the end of the test section. The separation bubbles created at the beginning of the diffuser grew

extremely large before reaching the first set of turning vanes. These unsteady regions of flow were too large to diffuse and continue all the way around the loop of the tunnel. Many attempts were carried out to alleviate the separation with no real solutions. Vortex generators and flow directors were used with minimal success on the back portion of the test section. They did move the detachment point further downstream, but separation still occurred somewhere near the beginning of the diffuser. Also the floor contour was extended so that an angle of diffusion between 4.5 and 5 degrees was obtained. Still the large separation bubbles were not completely controlled. With the final design, the fluctuations of the mean-flow velocity in this experiment were between 1 - 1.5%. The freestream spectra showed the mean-flow fluctuations were below 1hz. It was concluded that the design of the diffuser is inadequate for this type of experiment. The problems associated with the mean-flow fluctuations were solved by sampling all the hotwire data over a long enough period of time so the quantities being measured converged to a steady value. The final test section configuration is shown in figure 3.4.

Initially the wall bump and plate are installed in the test section. Pressure measurements are conducted on the plate by a series of static pressure ports, shown in figure 2.3. Chordwise measurements are conducted along the two rows of pressure ports located at $z = \pm 15\text{cm}$. The spanwise measurements are conducted along the four rows of pressure ports located at $x = 65, 125, 179, \text{ and } 232\text{cm}$. The original

test section configuration is shown in figure 3.4a. The 112 pressure ports are connected to 48 port manifolds and in turn connected to a scanivalve which relays the pressure signal to a differential pressure transducer with a full scale range of ± 5.2 mm Hg. The scanivalve and transducer are described in Appendix A sections A.15 and A.13. Blockage effects between the front and back sides of the plate are controlled by the use of a trailing-edge flap. Chordwise and spanwise pressure measurements are conducted using this initial test configuration with varied flap settings. These data are plotted in figures 3.5 thru 3.10. With this configuration, the spanwise C_p readings are not constant and show a strong gradient opposing the crossflow. The gradients in both the chord and span directions are reduced as the flap is opened towards the test side. They are at a maximum when the flap is set at 0 degrees. This indicates that the flap helps control the spanwise pressure gradient at the cost of reducing the chordwise pressure gradient. The cause of the opposing spanwise pressure gradient is due to the wall effects from the floor and ceiling.

The Kaups-Cebeci code (Kaups & Cebeci 1977) is run with the experimental chordwise C_p readings to calculate the deflections of the inviscid streamlines along the plate, as if it was an infinite swept wing. For more information on the Kaups-Cebeci code see Appendix B, section B.2. A plot of the streamline deflection, in centimeters along the plate, is shown in figure 3.11. With this information, floor and ceiling

contours made out of polystyrene are installed to obtain increased cross-flow and to provide a constant spanwise pressure gradient (ie. to eliminate end effects on the model caused by the walls). The contour of the floor and ceiling is shown in figure 3.12. With this modification to the test section, a relatively constant spanwise pressure distribution is obtained. Both the spanwise and chordwise pressure distributions are shown in figures 3.13 and 3.14. For the downstream spanwise C_p measurements a slight dip above and below the centerline is observed. It is felt that the cause of this is due to slight separation around the wall bump insert, which is recessed .95cm from the rest of the bump. The difference between the calculated C_p distribution from the Panel Method code (figure 2.9) and the experimental chordwise C_p distribution (figure 3.14) is due to separation on the initial contour of the wall bump. This separation causes the negative pressure rise to continue in the experiment further downstream and also causes the magnitude of the C_p to differ, with the experimental C_p having a larger negative rise than predicted with the theory.

3.3 MEAN-FLOW MEASUREMENTS

3.3.1 Inviscid Flow

Detailed measurements of the mean-flow velocities (U, W) in the chordwise and spanwise directions are conducted using a hot-wire anemometer. Straight-wire and slant-wire probes are used to obtain the velocity components (U, W). The U and W velocities with respect to the

plate coordinates are shown in figure 3.4. The vector sum of U and W forms the freestream velocity vector or the edge velocity, which describes the inviscid streamlines over the plate. Θ is the direction of the edge velocity with respect to the x -axis. Where applicable, the experimental results are compared to the theoretical codes.

Initial hot-wire measurements are conducted in the freestream along the plate. Chordwise measurements are carried out at three different spanwise locations ($z = -10, 0, 10\text{cm}$). Figures 3.15 and 3.16 show the variations of U and W along the plate for all three z locations. Due to the unsteadiness of the tunnel the data have to be sampled for a period of time, and then averaged to obtain steady readings. Thus each point in the figures is the averaged quantity from 1200 readings sampled over a period of one minute. These results indicate that the flow is very uniform in the spanwise direction. Figures 3.17 thru 3.19 show the variations of U and W and the angle between them with the theoretical calculations superposed on each, for one z location. Even though the differences seem quite large, in part due to the scaling, the agreement is very good considering the angle of the inviscid-flow vector differs by only about one degree, which is within the tolerance of the floor and ceiling fairings. The largest difference between the theory and experiment comes from the U component of flow, which would indicate a small magnitude difference in the freestream velocity vectors. This error is most likely due to the location of the Pitot tube. Initial

calculations are conducted to insure the Pitot tube is located in an undisturbed region of flow upstream. That is the pressure reading from the Pitot tube can be considered a reference pressure, not affected by the blockage in the test section. However, due to the installation of floor and ceiling fairings, the pressure at the Pitot tube changes as a result of increased downstream blockage in the test section. Because of the wind-tunnel design, the Pitot tube can not be moved any further upstream. So except for the slight magnitude difference, in the velocity vector, the trends in all three graphs (U,W, and Theta) show good agreement with the theory.

3.3.2 Boundary-Layer Profiles

Boundary-layer profiles are taken at different locations along the plate with both the slant-wire and straight-wire probes. Reduction of both the straight-wire and slant-wire data at one location produces a crossflow profile which in turn gives a crossflow Reynolds Number. This again provides comparison with the theory.

Initially a boundary-layer profile is taken with a straight-wire probe and then repeated with a slant-wire probe. Both the slant-wire and straight-wire probes are linearized to 1 volt in the freestream. The probes are automatically positioned by the MASSCOMP 560 around $u/U = 0.1$ and stepped out 10mm from this starting position. A variable step size is used so that a fine spacing is used near the wall and gradually increased as the probe is stepped out.

The first step in the data reduction is to obtain the actual y locations from the plate for the voltage readings that are recorded: in other words, to find the distance between the first data point and the plate. A linear fit using six points provides consistent results. Once this is done the voltage arrays for the two wires have to be matched up at the same y locations. This is done using a linear interpolation scheme on the straight-wire voltage readings. Next, the velocity components (U, W) have to be extracted from the data. This is done by multiplying the voltage arrays by the upstream velocity at the Pitot tube and the freestream voltage for that x and z location. Thus, the U velocity component of flow is simply the new straight-wire voltage reading, and the W velocity component of flow is equal to the new slant-wire voltage minus the new straight-wire voltage reading. The velocity components (U, W) are then transformed by the angle θ , placing the new component U in the direction of the freestream velocity vector. These new components will be called U_t and W_t . The angle θ is obtained from the freestream calculations for that particular x and z location ($\theta = \arctan(W/U)$). Finally boundary layer profiles parallel and transverse to the freestream velocity vector are obtained. The transverse profile is called the crossflow profile. By definition, since the crossflow profile is perpendicular to the edge velocity, the crossflow velocity is zero in the freestream. From this profile a crossflow Reynolds Number is calculated (Pfenninger 1977). It is defined as

$$R(cf) = \frac{d(10) * W_{tmax}}{v}$$

where $d(10)$ is the height at which the crossflow velocity is 10% of the maximum value, and W_{tmax} is the maximum crossflow velocity. Another parameter defined by the crossflow profile is the crossflow shape factor H_c defined as

$$H_c = \frac{Y(W_{tmax})}{d(10)}$$

where $Y(W_{tmax})$ is the height above the model surface at which the crossflow profile has its maximum velocity.

Figures 3.20 thru 3.22 are normalized boundary layer plots of U_t and W_t at $x=100, 120, 170$ cm respectively, with a reference velocity of 10m/s. Figures 3.23 thru 3.25 are plots of W_t/U_{et} at the same locations and velocity, where U_{et} is the edge velocity at the particular x location. Similar measurements were taken every 5cm in the chord direction and the data shown here are representative of the total data collection. These results are compared with the theoretical calculations of the Kaups-Cebeci code using the experimental pressure distribution. The experimental results at $x=100$ cm tend to agree in the magnitude of the crossflow and the location above the test surface where the

maximum crossflow occurs. At $x=120\text{cm}$ the magnitude of crossflow begins to differ, but the location of the max crossflow is still in good agreement. However, the slight reversal of flow near the wall in both these cases does not appear in the theory and could be due to experimental error in trying to extract out such small differences in the data. The final profile at $x=170\text{cm}$ differs widely from the theory in both magnitude and location of the maximum crossflow. Figures 3.26 and 3.27 are more boundary layer profiles of U_t and W_t at $x=100\text{cm}$ and 140cm with a reference velocity of 14m/s . Figures 3.28 and 3.29 are plots of W_t/U_{et} at the same locations and velocity.

The scatter in all the data is due to resolving small differences of large numbers after each is interpolated from a straight-wire and slant-wire profile and then transformed into the U_t and W_t directions. The increasing disagreement in the theory and experiment aft of 100cm can be attributed to the fact that the experimental streamline deflection angle along the plate is larger than predicted, causing the crossflow velocity to increase faster than the theory. The following table shows the calculated crossflow Reynolds numbers and shape factors for the previously mentioned boundary-layer data, along with the theoretical calculations from the Kaups-Cebeci code.

REFERENCE VELOCITY 10m/s

x location	EXPERIMENT		THEORY	
	R_{cf}	H_c	R_{cf}	H_c
100cm	100	.48	112	.331
120cm	272	.33	120	.333
170cm	600	.29	135	.336

REFERENCE VELOCITY 14m/s

x location	EXPERIMENT		THEORY	
	R_{cf}	H_c	R_{cf}	H_c
100cm	161	.37	145	.288
140cm	291	.36	139	.362

The experimental results clearly show that the crossflow is increasing through the measurement region and that a strong crossflow instability occurs. The Re_{cf} at $x=170\text{cm}$ is a factor of four larger than predicted by the Kaups-Cebeci code. The decrease in the experimental shape factors along the plate indicate that momentum is increasing near the wall. Note also that the shape factors for the theory show an opposite trend, with the location of the maximum crossflow velocity moving away from the plate surface. The large differences in the theory and experiment point to the conclusion that the experimental model does not represent an infinite swept wing.

Figure 3.30 is a composite of W_t/U_{et} for three x locations (100,120,170cm) at the reference velocity of 10m/s. Figure 3.31 is a composite of W_t/U_{et} at $x=100,140\text{cm}$ with a reference velocity of 14m/s.

These two figures show the increase in crossflow along the plate and the shift in the maximum crossflow velocity towards the wall.

3.3.3 Spanwise Measurements of Vortices

Disturbance measurements of the mean flow are conducted within the boundary layer by making a z-traverse of the hot wire at a constant y location with respect to the plate. Good results are obtained using a z spacing of 1mm and a sampling period of 5 seconds. These measurements are carried out at many different x and y locations using two different mean velocities. The results show a steady vortex structure with a spanwise wavelength of approximately 0.5cm. This wavelength does not agree with the flow visualization results of the next section nor the theoretical calculations of the Maria code (Dagenhart 1981). At this time the reason for the disagreement is unknown. Figures 3.32 thru 3.40 show many of the typical spanwise structures at different x locations for reference velocities of 10 and 14m/s. At x= 85cm the structure is well defined and shows the largest spanwise variations. Moving back in x the spanwise variations decrease and the structure begins to show signs of unsteadiness. These changes are thought to be due to some type of interaction with weak growing T-S waves. The corresponding spectra for these disturbance measurements are shown in figures 3.41 thru 3.49. They show a sharp peak at a wavelength of about 0.5cm, but they also show broad peaks at larger wavelengths, generally at a lower amplitude. The cause of these broad peaks at the larger wavelengths is not known at this time.

The vibrating ribbon is used to introduce T-S waves into this region where crossflow vortices are known to exist. The ribbon is placed at $x=115\text{cm}$ at a distance of 0.2mm off the plate. Then the largest attainable amplitudes are introduced into the flow where a negative pressure gradient still exists. However, the disturbances are damped out before they reach the constant pressure region. There are very little signs of T-S waves in the hot-wire output spectra nor in the photographs of the streaklines from the smokewire technique. Due to the limited amount of wind tunnel time, very little data is taken and no conclusions can yet be drawn. The test section configuration will have to be modified in order to allow introducing the T-S waves in the zero pressure gradient area, or the amplitude of disturbances introduced by the ribbon will have to be increased dramatically.

3.4 FLOW VISUALIZATION

There are two types of flow visualization techniques used in the experiment. One is the "smoke-wire" technique, (Weber et al. 1980) in which a stainless steel wire 0.076mm in diameter is positioned inside the boundary layer. A thin layer of oil is distributed along the wire, then a voltage is applied to burn the oil off the wire. The streaklines that develop are then photographed by a camera outside the test section. In this experiment the smoke wire is positioned at the sweep angle. Due to gravity and the smallness of the boundary layer, a different technique is developed to coat the wire with oil. A small piece of tin is

wrapped around the wire, the interior is stuffed with cotton and then oiled. Thin monofilament line is attached to the "oiler" and strung from the floor and ceiling to the control room. Once the test conditions are set, oil is applied along the wire by the oiler from outside the test section, and, in the usual manner, a photograph of the streaklines is taken. This technique allows the smoke-wire method to be used at higher velocities than before and also allows the positioning of the smoke-wire much closer to the plate surface.

The objective of the visualization technique is to place the wire in the critical layer of the boundary layer where the wave speed and the phase speed are equal. The oil is then burned off the wire and the smoke particles roll over as they propagate down the plate. This technique provides the best visualization of the wave forms. However, in this experiment many attempts were carried out at four x -locations along the plate, ($x = 70, 110, 140, 170\text{cm}$), positioning the wire at different heights above the plate, with no signs of any vortex structure. Based on previous experience with this technique we conclude that the crossflow vortices are still too weak to visualize with smoke particles. This is because the v' and w' components of the disturbance velocity are smaller than u' by the order of $1/Re$. Thus, the large changes in u that are observed are caused by a redistribution of streamwise momentum by the weak v' and w' components. The visualization of natural disturbances in the boundary layer is only one way of using the smoke-wire technique.

The vibrating ribbon is used to introduce known disturbances into the boundary layer. The smoke-wire is then used to visualize the interaction of T-S waves with crossflow vortices. The ribbon is placed at $x = 115\text{cm}$ then excited at the most unstable frequency, based on downstream hot-wire measurements. Again the wire is positioned at the critical layer in the boundary layer. Very weak T-S waves are visualized, but no spanwise wavelength is observed. The reason for this is due to the location of the ribbon. The T-S waves decay rapidly in the decreasing pressure region and disappear before reaching the constant pressure region, where amplification of the T-S waves occurs. Again it must be emphasized that future experiments must be modified so that disturbances are introduced in the zero pressure gradient region where T-S waves and crossflow vortices are thought to interact.

The second type of flow visualization employed in the experiment is similar to the "china-clay evaporation" method of Richards and Burstall (1945). In this experiment a solution of trichlorethane and naphthalene is sprayed directly on the plate surface. The trichlorethane acts as a solvent when mixed with the solid naphthalene crystals. Once the solution is sprayed on the plate the solvent quickly evaporates leaving the solid naphthalene. The test conditions are set and visualization of surface patterns on the plate are observed and photographed as the naphthalene sublimates. A mixture of 0.1 liters of naphthalene to one liter of trichlorethane is sprayed, using paint spray equipment, on the plate over the area of interest. Once a very even

coat is applied, a fine cloth is used to wipe off excess leaving a very smooth, uniform film on the surface. The sublimation rate of the naphthalene is very temperature dependent and the best results are obtained when the temperature is around 20-25 degrees C. At temperatures above this range, the sublimation rate is extremely fast and visualization of the surface patterns are very difficult. Temperatures below this range provide good results, but utilization of the tunnel is very poor due to the long periods of time required for the naphthalene solution to sublime. This flow visualization technique shows that there exists a crossflow vortex structure on the swept flat plate. The creation of the vortex structure is due to the pressure gradient generated by the wallbump. Figures 3.50 and 3.51 show typical surface patterns that develop. This vortex structure is made visible because of the differential sublimation of the naphthalene according to variations of the surface shear stress. The pattern of disturbance vortices are nearly equally spaced and aligned approximately in the potential-flow direction. The wavelength of the vortices is on the scale of 1 cm and this spacing agrees quite well with the calculated wavelength from the MARIA code. For more information on the MARIA code see Appendix B, section B.3.

Chapter IV

CONCLUSIONS

An experiment to investigate the crossflow instability has been conducted at VPI&SU. This initial experimental investigation has helped to identify the major difficulties in this work, such as: wall effects opposing the crossflow and separation due to large amounts of blockage. Crossflow on a swept flat plate has been demonstrated using a wall bump. Future experiments should be able to expand upon this technique, along with studying the interaction of T-S waves with crossflow vortices and laminar flow control using suction panels. The comparison of the theory and experiment has shown some agreement, but differences exist, for example in the observed wavelength and the amount of crossflow, and the reasons are still unknown.

Initially floor and ceiling fairings were installed to match the theoretical streamlines from the Kaups-Cebeci code. With this modification, a relatively constant spanwise pressure gradient was obtained on the plate. The verification of this was accomplished by static pressure measurements on the plate and also freestream hot-wire measurements. Measurements were conducted in the freestream to calculate the magnitude and direction of the velocity vector and showed agreement with the theory.

Boundary layer profiles were taken with a slant-wire and straight-wire, then the data was reduced to obtain the crossflow

profile. Comparison with the theory showed some agreement at $x=100\text{cm}$, but tend to differ at downstream chord locations. The experiment showed an increase in crossflow and a decrease in the shape factor for the crossflow profile as the waves propagate along the plate.

Spanwise boundary layer measurements were conducted and show a steady variation in the mean flow with a wavelength of about 0.5cm . Flow visualization using a sublimation technique showed a fixed surface pattern with a spanwise wavelength of about 1cm . This wavelength agrees quite well with the theoretical Maria code.

These initial measurements have shown that the crossflow instability can be studied on a swept flat plate. The wall bump has presented itself as an innovative and inexpensive tool for research in conjunction with the plate. With a few modifications made to the existing experimental capabilities this experiment should provide lots of valuable data on the crossflow instability.

REFERENCES

- Bradshaw, P. 1965 "The effect of wind tunnel screens on nominally two-dimensional boundary layers," *J. Fluid Mech.* 22, pp. 679-688.
- Bristow, D. R. 1980 "Development of panel-method codes for subsonic analysis," NASA Contractor Report 3234, NASA Langley Research Center, Hampton, Va.
- Cebeci, T. & Stewartson, K. 1980 "On stability and transition of three-dimensional flows," *AIAA Journal*, Vol. 18, No. 4, pp. 398-405.
- Corke, T., Koga, D., Drubka, R. & Nagib, H. 1974 "A new technique for introducing controlled sheets of smoke streaklines in wind tunnels." *Proc Int'l Cong. on Instr. in Aero. Sim. Fac. IEEE Pub.* 77 CH 1251-8, AES, 74-80.
- Dagenhart, J. 1981 "Amplified crossflow disturbances in the laminar boundary layer on swept wings with suction." NASA Technical Paper 1902.
- Floryan, J. M. & Saric, W. S. 1980 "Wavelength selection and growth of Gortler vortices," *AIAA Paper No.* 80-1376.
- Gregory, N., Stuart, J. T., & Walker, W. S. 1955 "On the stability of three-dimensional boundary layers with applications to the flow due to a rotating disk," *Philosophical Transactions of the Royal Society of London*, Vol. A248, pp. 155-199.
- Herbert, Th. & Morkovin, M. V. 1980 "Dialogue on bridging some gaps in stability and transition research," In: *Laminar-Turbulent Transition* (eds. R. Eppler & H. Fasel), Springer-Verlag, pp. 37-46.
- Jaffe, N. A., Okamura, T. T. & Smith, A. M. O. 1970 "Determination of spatial amplification factors and their application to transition," *AIAA Journal*, Vol. 8, pp. 301-308.
- Kaups, K. & Cebeci, T. 1977 "Compressible laminar boundary layers with suction on swept and tapered wings," *J. Aircraft*, Vol. 14, No. 7, pp. 661-667.
- Malik, M. R. & Poll, D. I. A. 1984 "Effect of curvature on three-dimensional boundary layer stability," *AIAA Paper No.* 84-1672.

- Malik, M. R., Wilkinson, S. P. & Orszag, S. A. 1981 "Instability and transition in rotating disk flow," AIAA Journal, Vol. 19, No. 9, pp. 1131-1138.
- May, C. L. & Saric, W. S. 1983 "A panel-method code to design wind-tunnel modifications for pressure gradients on models," Part I. Inviscid Analysis. VPI&SU Report, VPI-E-83.25.
- Michel, R., Arnal, D., Coustols, E. & Juillen, J. C. 1984 "Experimental and theoretical studies of boundary layer transition on a swept infinite wing," 2nd IUTAM Symposium on Laminar-Turbulent Transition, Novosibirsk, U.S.S.R.
- Michel, R., Arnal, D. & Coustols, E. 1984 "Stability calculations and transition criteria in two- or three-dimensional flows," 2nd IUTAM Symposium on Laminar-Turbulent Transition, Novosibirsk, U.S.S.R.
- Nayfeh, A. H. 1980 "Stability of three-dimensional boundary layers," AIAA Journal, Vol. 18, No. 4, pp. 406-416.
- Nayfeh, A. H. 1981 "Effect of streamwise vortices on Tollmien-Schlichting waves," J. Fluid Mech. 107, pp. 441-453.
- Pfenninger, W. 1977 "Laminar flow control laminarization," Special course on concepts for drag reduction, AGARD-R-654, pp. 3-1 - 3-75.
- Pfenninger, W., Reed, H. L. & Dagenhart, J. R. 1980 "Design considerations of advanced supercritical, low-drag suction airfoils," In: Viscous flow drag reduction, Gary Hough (ed.), AIAA Progress in Astronautics and Aeronautics, Vol. 72, pp. 249-271.
- Poll, D. I. A. 1979 "Transition in the infinite swept attachment line boundary layer," The Aeronautical Quarterly, Vol. XXX, pp 607-628.
- Poll, D. I. A. 1983 "Transition description and prediction in three-dimensional flows," College of Aeronautics Report 8332, Cranfield, England.
- Poll, D. I. A. 1984 "Some observations of the transition process on the windward face of a yawed cylinder," College of Aeronautics Report 8407, Cranfield, England.
- Reed, H. L. 1984 "Wave interactions in swept-wing flows," AIAA Paper No. 84-1678.

- Reed, H. L. & Nayfeh, A. H. 1984 "A numerical perturbation technique for determining the stability of flows over plates with porous suction Strips," accepted AIAA Journal. (See also: Stability of flow over plates with porous suction strips. AIAA Paper No. 81-1280.).
- Reynolds, G. A. & Saric, W. S. 1984 "Experiments on the stability of the flat-plate boundary layer with suction," accepted AIAA Journal, AIAA Paper No. 82-1026.
- Reynolds, G. A. 1979 "Experiments on the stability of the Blasius boundary layer," M.S. Thesis, ESM Dept., VPI & SU, June 1979. Also NASA-CR-157256.
- Richards, E. J. & Burstall, F. H. 1945 "The 'china clay' method of indicating transition," ARC report and memorandum 2126.
- Smith, A. M. O. & Gamberoni, N. 1956 "Transition, pressure gradient, and stability theory," Douglas Aircraft Company, Inc., Rep. No. ES 26388.
- Srokowski, A. J. & Orszag, S. A. 1977 "Mass flow requirements for LFC wing design," AIAA Paper No. 77-1222.
- Van Ingen, J. L. 1956 "A suggested semi-empirical method for the calculation of the boundary-layer transition region," Dept. of Aero. Eng., Univ. of Technology, Delft, Holland, Repts. VTH-71 and 74.
- Weber, D. L., Saric, W. S., Reynolds, G. A., Tice, G. L. & Woodbridge, R. D. 1980 "Visualization of Tollmien-Schlichting waves," Bull. Amer. Phys. Soc. 25, 1081.

Appendix A
ELECTRONIC EQUIPMENT

A.1. DISA ANEMOMETRY. Three independent anemometry channels are used. Each channel consists of:

A.1.1. DISA 55DOL Constant Temperature Anemometer (CTA).

The anemometer is operated with a bridge ratio of 1:20 using a probe cable length of 5m. For high resolution measurement of low-level signals, the hot wires and cables are balanced at a gain of 11 and operated at a gain of 7. The anemometer output voltage V is related to the air velocity U by King's Law (King 1914): $V^2 = V_o^2 + B*U^n$, where V_o^2 , B , and n are functions of temperature. The hot wires are calibrated through the MASSCOMP 560.

A.1.2. DISA 55D10 Linearizer. All anemometer outputs are processed through this unit to obtain a voltage signal which is linearly proportional to the velocity being measured. The unit is calibrated by a plot of $\log U$ vs. $\log((V/V_o)^2 - 1)$ from the anemometer. This procedure is handled through the MASSCOMP 560.

A.1.3. DISA 55D35 RMS Voltmeter. A true r.m.s. and squared r.m.s. is obtained in the range of -60 dB to 50 dB over one volt. The integrator time constant is variable in the range of 0.3 to 100 seconds. Analog output is available for input to the MASSCOMP 560.

A.2. DISA HOT-WIRE PROBES.

A.2.1. DISA 55PO5 Boundary-Layer Probe. The sensor consists of a 5 μ m diameter Platinum-plated tungsten wire with an overall length of 3mm and a sensitive wire length of 1.25mm ($L/D = 250$). Sensor-support prong isolation is provided by a copper and gold plating at the wire ends to a diameter of approximately 30 μ m.

A.2.2. DISA 55P71 Parallel-Array Turbulence Probe. This is a two wire probe with parallel sensors separated by 0.4mm. The probe sensors measure freestream turbulence at essentially the same point and thus allow elimination of electronic noise from the two independent channels.

A.2.3. DISA 55P02 Slant-Wire Probe. This is used in conjunction with another probe to measure the w' fluctuations.

- A.2.4. DISA 55P51 X-Array Probe. This is used for two-component velocity measurements in the mean flow.
- A.2.5. DISA 55A12 and 55A13. Spot-Welding Mechanism for Hot Wires. This unit is used to repair broken hot wires and to build special wires for special applications.
- A.3. MASSCOMP 560. This system provided two ultra-high speed, 16-channel, data sampling capabilities. This enabled real-time data-processing capabilities with output via floppy disk, printer, CRT display, and digital plotting. This system controlled the whole experiment and data acquisition. This system, built around a real-time UNIX operating system is the state-of-the-art in data acquisition. All hot-wire calibrations, mean-flow measurements, proximeter calibrations, 3-D traverse control, conditional sampling, freestream turbulence levels, and boundary-layer disturbance measurements are interfaced into the MASSCOMP 560. The signals from the constant-temperature, hot-wire anemometers are conditioned using the usual assortment of linearizers, oscillators, tracking filters, phase meters, r.m.s. meters, and log converters described below. The traverse mechanism and the HP 5420A Spectrum Analyzer are also operated with this unit either in a programmed fashion or in response to the hot-wire signal. The MASSCOMP 560 has:

1 MB RAM
 1 MB floppy disk
 27 MB Winchester disk
 floating-point accelerator
 1 MHz, 16-channel A/D
 8 channel, simultaneous sample/hold
 500 KHz/channel, 4 channel D/A
 16 lines parallel digital I/O
 IEEE-488 interface
 8 lines RS-232C I/O mux (independent access ports)
 graphics processor (800 x 600 x 2 x 2 pixels)
 data acquisition/control processor and STD + bus
 console/CRT
 matrix alphanumeric/graphics printer

- A.4. HP 5420A DIGITAL SIGNAL ANALYZER. This is a 2-channel, digital, Fast Fourier Transform spectrum analyzer which provides time and frequency domain analysis of analog signals in the range of DC to 26 KHz. Analog data is input through the HP 54410A Analog/Digital Converter, and anti-aliasing is provided by a HP 54470 Digital Filter. Unfiltered hot-wire signals are analyzed in conjunction with the MASSCOMP 560. Both steady and triggered modes are possible.
- A.5. HP 3960 INSTRUMENTATION TAPE RECORDER. This unit is portable, 4-channel, 3-speed tape recorder which uses 6.35 mm magnetic tape. The recorder could be operated in either FM mode or direct record mode. It is used in FM mode which provides a DC to 5 KHz frequency bandwidth.

- A.6. HONEYWELL MODEL 5600B TAPE RECORDER. Two of these units provide 24 channels of either direct or FM-mode continuous records. These units, when used with the MASSCOMP 560 computer system, give a failsafe backup to the real-time data analysis.
- A.7. SPECTRAL DYNAMICS SD121 TRACKING FILTER. This unit is a phaselocked servo, narrow band-pass filter which is tuned to the reference-signal input. It is used with a bandwidth of 1 Hz, while bandwidths of 2, 10, 50, and 200 Hz are also available (three independent filter channels are available).
- A.8. SPECTRAL DYNAMICS SD131 PHASE METER. Relative phase between any two measured signals is monitored with this unit. Typical usage is the measurement of the phase between the vibrating ribbon signal and the anemometer signals in order to determine the wavelength of the disturbance.
- A.9. TRAVERSE CONTROLLER. Pulses to all three traversing mechanismstepping motors are provided by a Superior Electric ST103 Translator. This unit is supplemented by a controller/counter which provides convenient selection of motor stepping modes available though the ST103. These include half-step/full-step, low-speed/high-speed, and continuous-run/single-step options. Motor steps are also counted by the Traverse Controller and are output in a binary LED display as well as a

front-panel mounted DVM and its corresponding analog voltage output. This unit is also operated by the MASSCOMP 560 system.

- A.10. TEKTRONIX MODEL 5113 OSCILLOSCOPE. This is an 8-channel scope with 2-channel storage capabilities.
- A.11. HP 5300A/5302A FREQUENCY COUNTER. This counter provides frequency measurements with a resolution of 0.1 Hz for a ten-second sample period.
- A.12. BRUEL & KJAER 2427 AUTORANGING DIGITAL VOLTMETER. This voltmeter provides a true r.m.s., average, or peak reading for input signals in the range of 0.5 Hz to 500 KHz.
- A.13. SETRA-SYSTEMS MODEL 239E DIFFERENTIAL PRESSURE TRANSDUCER. This is a ± 0.1 psid (± 5.2 mmHg) transducer which provides a linear DC output of ± 2.5 volts. It is used for static-pressure measurements on the model surface. Other transducers with ranges of ± 0.01 and ± 0.25 psid were available.
- A.14. BENTLY-NEVADA SERIES 190 PROXIMETER PROBE/SERIES 3000 SIGNAL CONDITIONER. This is an inductance-type probe which has a linear measuring range of 0.0 - 1.1mm with a nominal output of 0.0 to -14 volts DC. The frequency response is DC to 10 KHz, $\pm 1\%$. Two of these transducers are used to monitor sting vibration and ribbon vibration.

- A.15. SCANIVALVE MODEL D. This solenoid operated mechanism provides for serial sampling of 48 pressure inputs. The selected pressure input is then available for pressure-transducer measurement. Two of these units were available for use.
- A.16. MISCELLANEOUS. The usual collection of multimeters, strip-chart recorders, low-pass and band-pass filters, differential amplifiers, signal generators, power supplies, and (x,y,y') analog plotters are available.

Appendix B

COMPUTER CODES

B.1. PANEL METHOD CODE & INVERSE PANEL-METHOD CODE

These two programs developed at Virginia Tech (May & Saric 1983) are modifications to a panel-method program written at NASA Langley Research Center. This program is a Multi-element Analysis Design code (MAAD) which solves flow problems that are two-dimensional, inviscid, irrotational and incompressible. The panel method code solves an internal-flow problem. Given the geometry of the test section and the freestream test conditions a pressure distribution is calculated over the test side of the plate. The inverse panel-method code takes a desired pressure distribution on the test side of the plate and generates a bump on the opposite wall. This is accomplished by inputting the prescribed pressures and plate coordinates. Then the wind-tunnel wall coordinates are generated based on one-dimensional flow and a comparison is made between the desired and calculated pressure distributions. Finally, an iteration scheme is used to obtain the desired pressure distribution to within error bounds of the calculated pressure distribution.

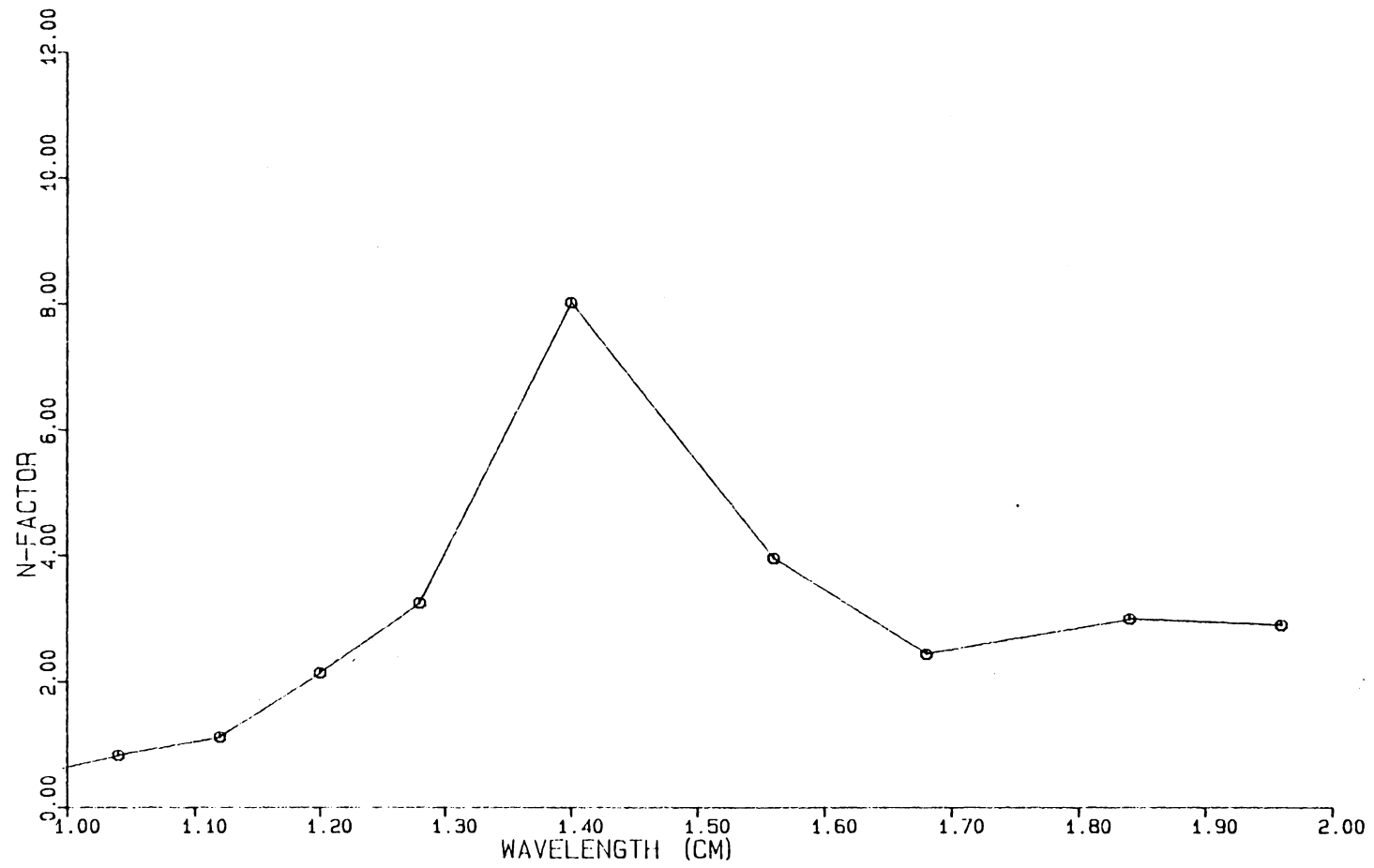
MAAD uses surface panels coupled with incompressible potential-flow theory to obtain and solve a surface integral equation. An object such as the plate or wallbump is modeled by a distribution of singularities on the boundary. A uniform freestream is superimposed on the singularities to form solid bodies. MAAD employs a combination of sources and doublets, chosen for accuracy and numerical stability.

B.2. KAUPS-CEBECI CODE

This code solves the three-dimensional, compressible laminar boundary-layer equations with or without suction for swept and tapered wings. The conical-flow assumption is used, that is pressure isobars are located along constant percent-chord lines. The analysis ignores the wingtip and wingroot since they do not obey the conical-flow assumption. Also, wing twist is not considered, so geometrical similar sections are obtained along the span of the wing. Due to the assumption of a zero spanwise gradient the three-dimensional boundary-layer equations are transformed into a two-dimensional form by similarity transformations. The equations are then solved by Keller's box method. This is a precise and able numerical method used for solving parabolic partial differential equations.

B.3. MARIA CODE

This code studies the amplified disturbances in a laminar boundary layer on an infinite swept wing with or without suction. The code is an alternative to more complex codes such as the SALLY stability code of Srokowski and Orszag (1977). The SALLY code studies the growth of disturbances in the laminar boundary layer utilizing small disturbance theory. This is applied to the Orr-Sommerfeld equation which when coupled with its boundary conditions form an eigenvalue problem. The solution of the eigenvalue problem is very time consuming to solve on the computer. The MARIA code bypasses the eigenvalue problem by developing an algorithm that approximates the disturbance growth rates based on a range of known solutions of the Orr-Sommerfeld equation. The Kaups-Cebeci code supplies the needed three-dimensional laminar boundary layer data for the MARIA code. From this input the maximum growth rates of naturally occurring disturbances are calculated for a given set of wavelengths.



Integrated maximum growth rates vs. wavelength

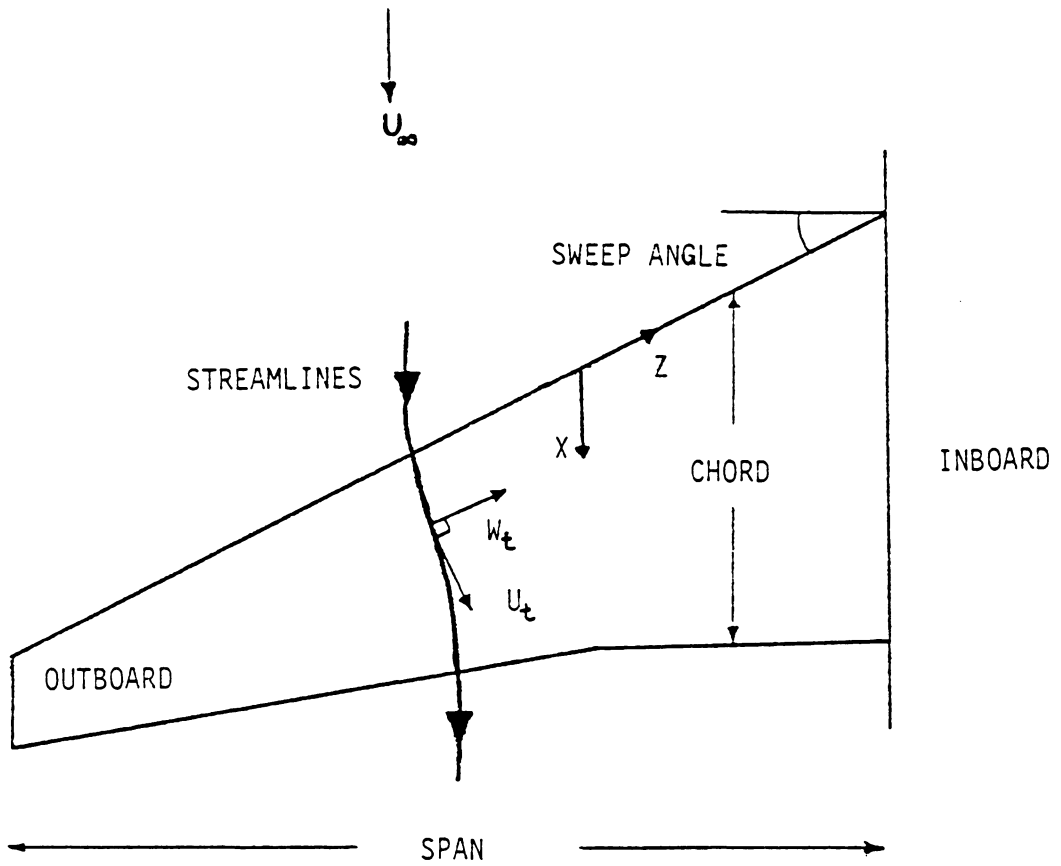


Figure 1.1 Top view of a typical swept wing.

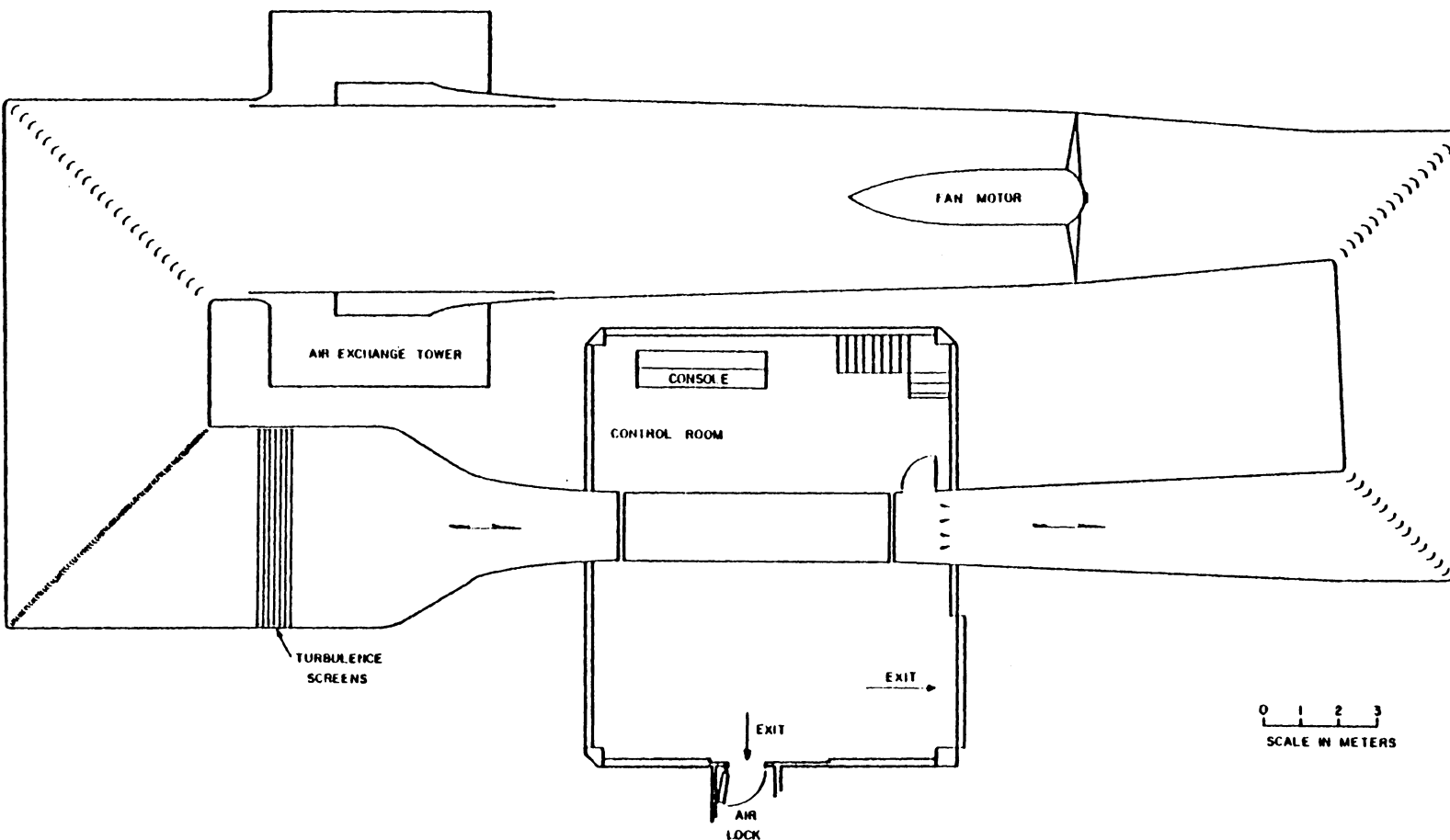


Figure 2.1 Cut-away view of V.P.I. & S.U. Stability Wind Tunnel showing turning vanes, turbulence screens, control room, and test section.

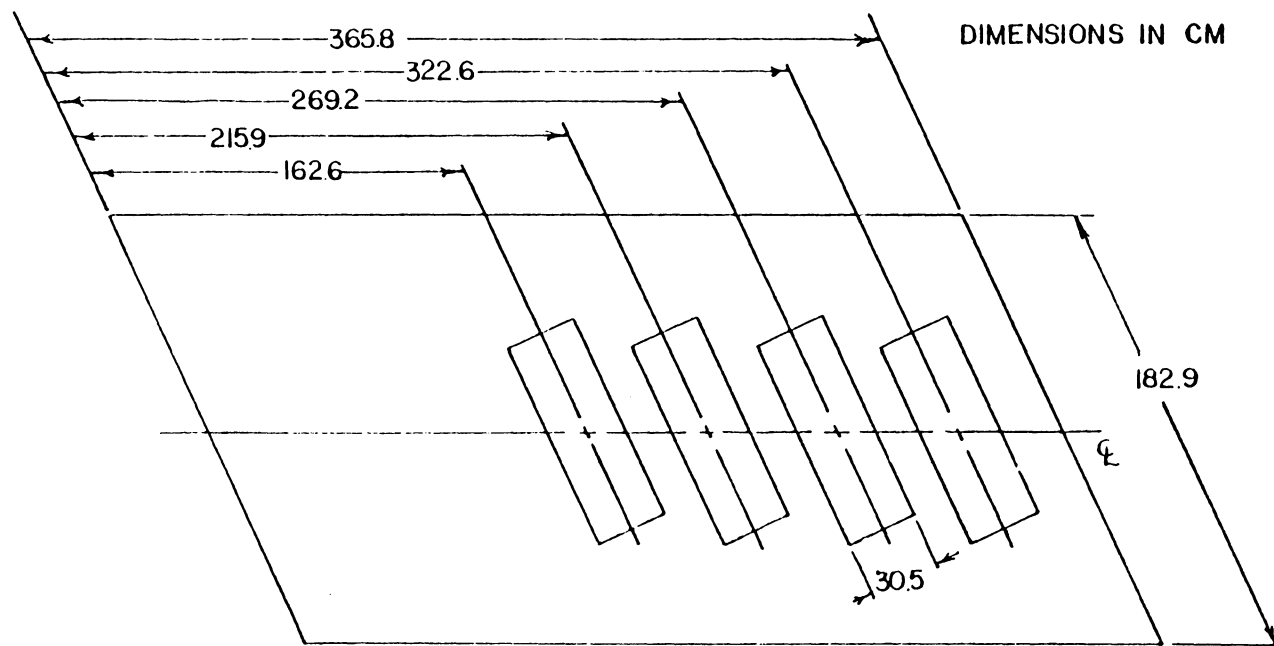


Figure 2.2 Swept flat plate with cut-away locations.

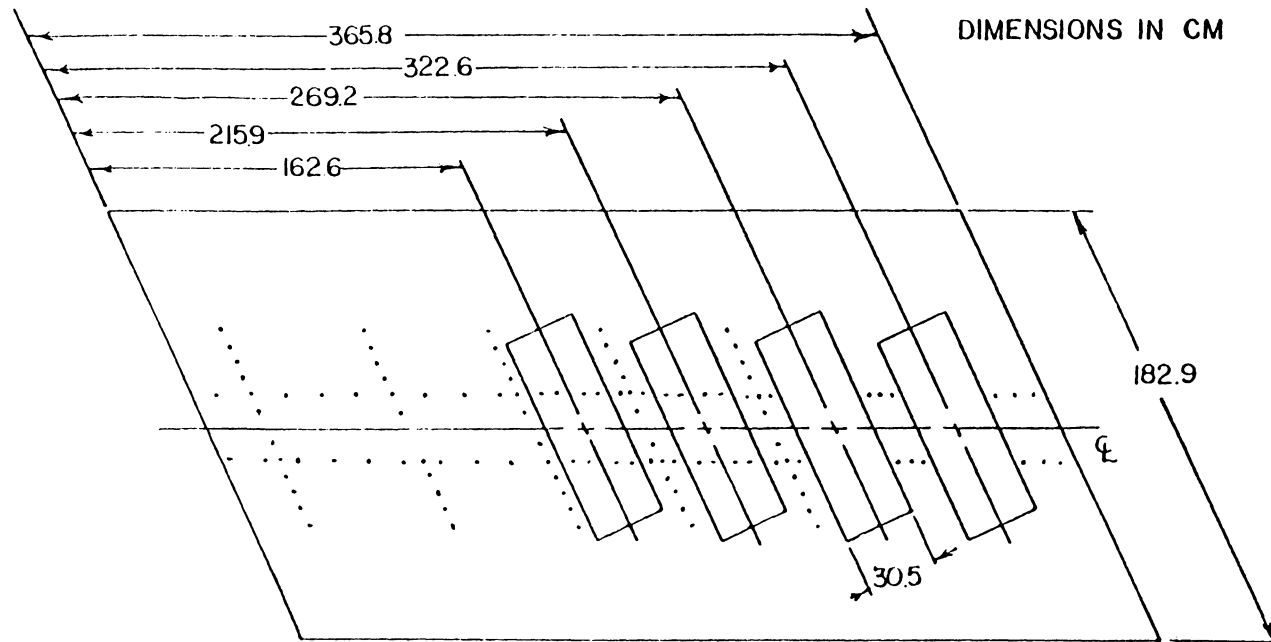


Figure 2.3 Swept flat plate with static pressure port locations.

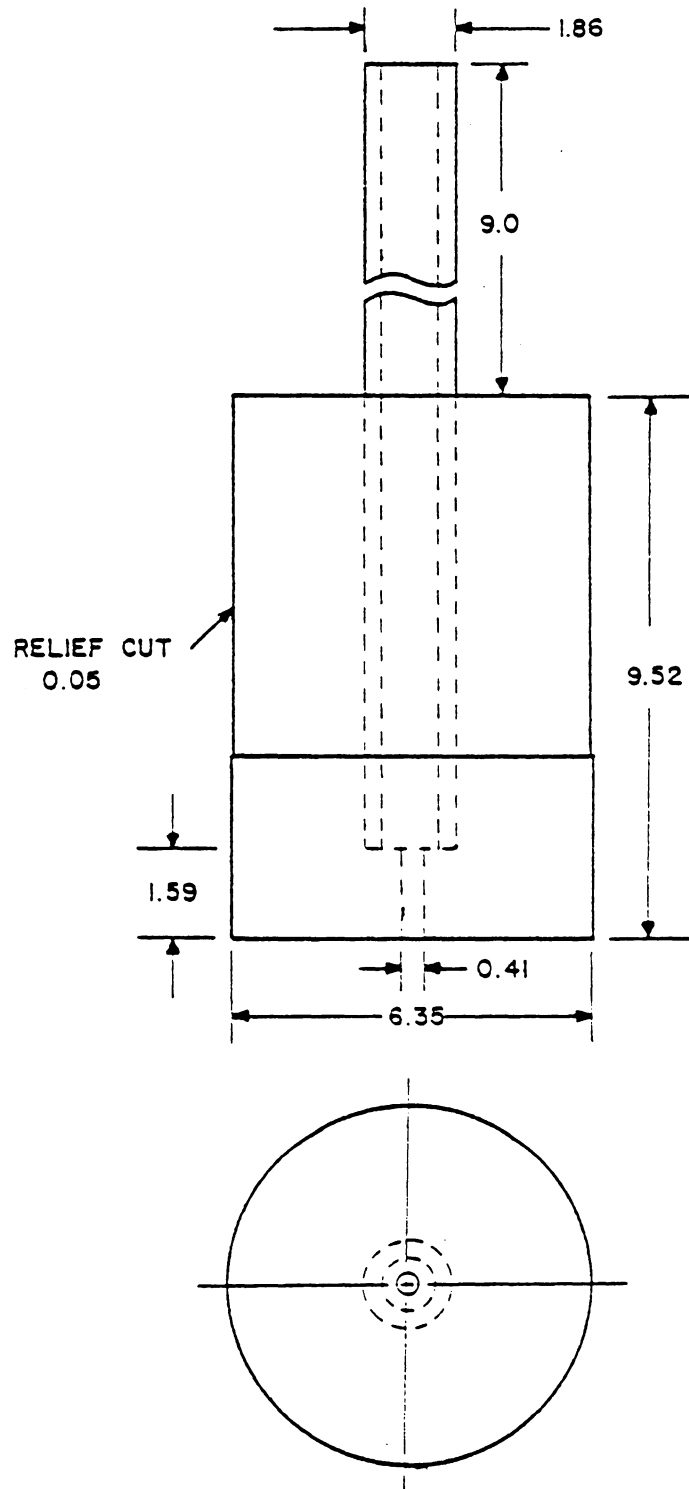


Figure 2.4 Static-pressure-port insert. All dimensions given in millimeters.

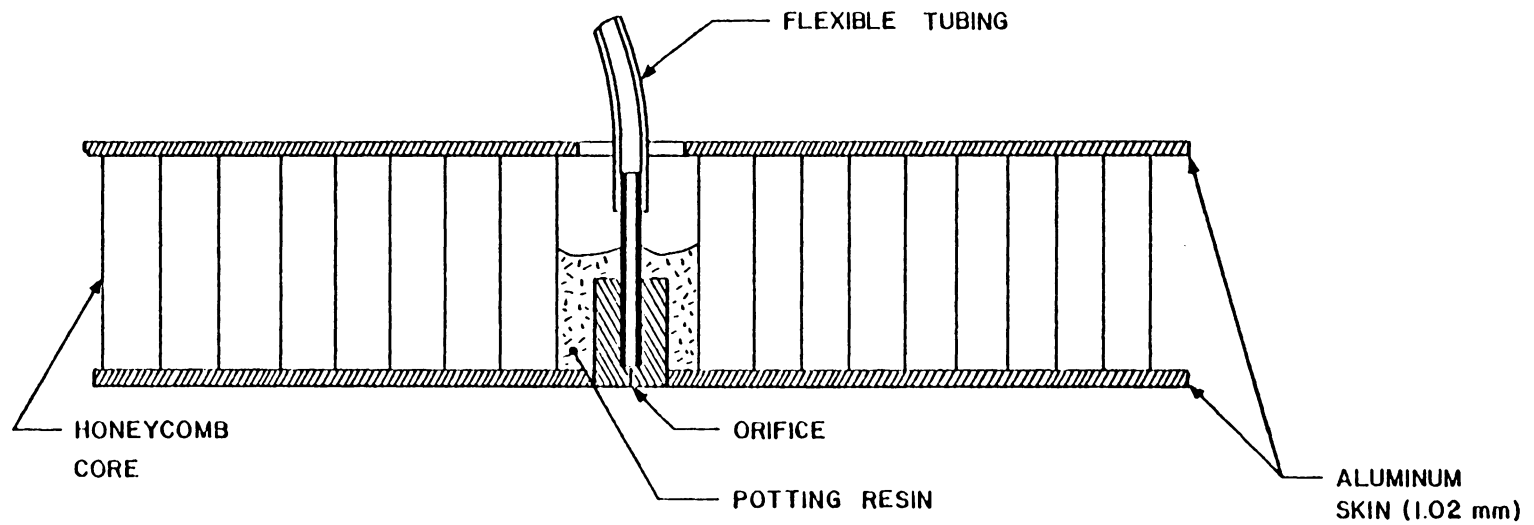


Figure 2.5 Static-pressure-port assembly and plate cross section.

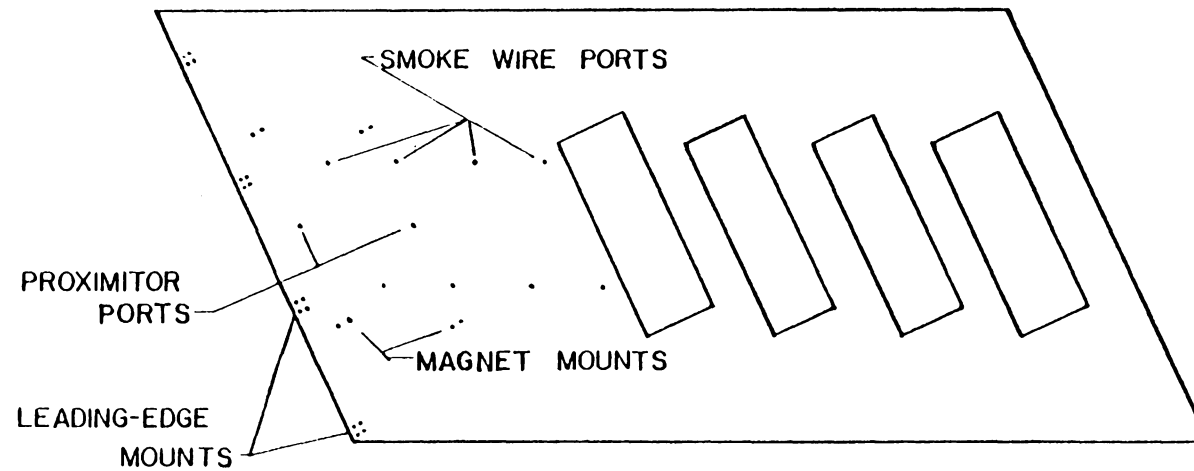


Figure 2.6 Plate modifications and their locations.

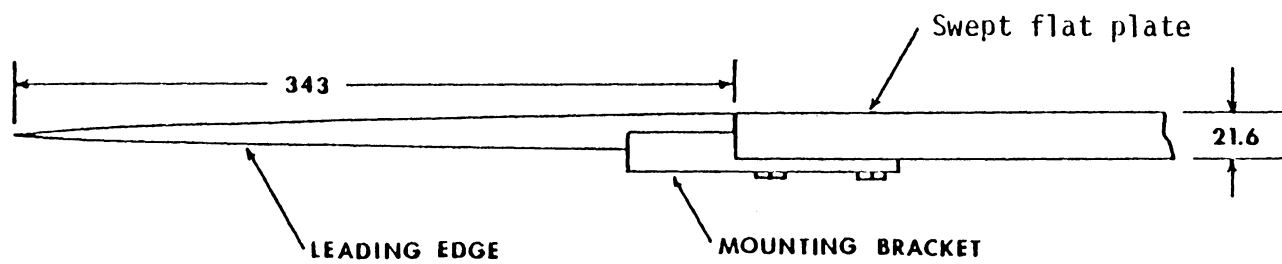


Figure 2.7 Leading edge, swept flat plate junction. All dimensions in mm.

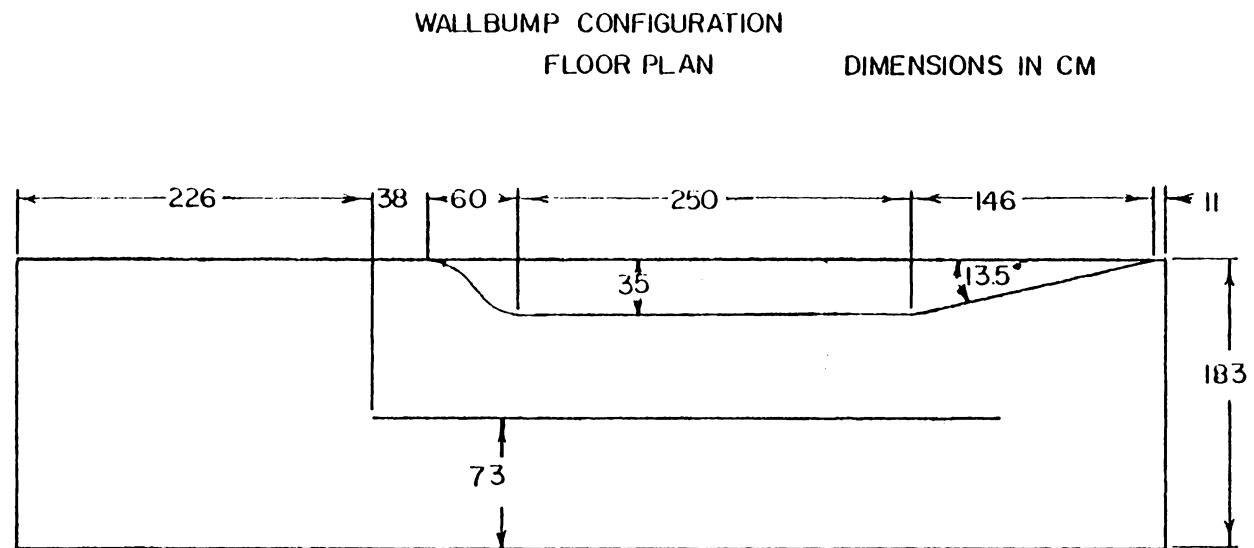


Figure 2.8 Initial test section configuration based on the Inverse Panel Code.

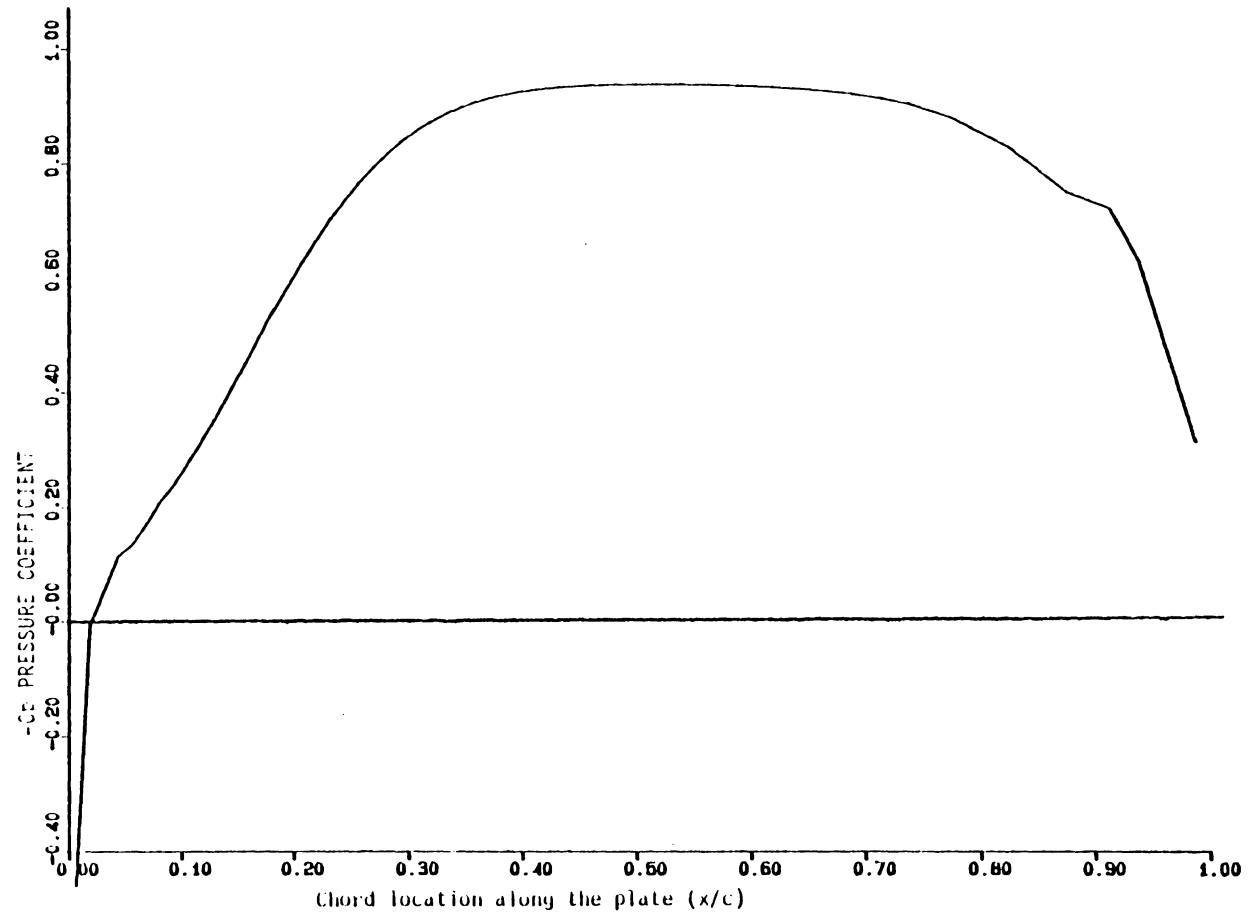
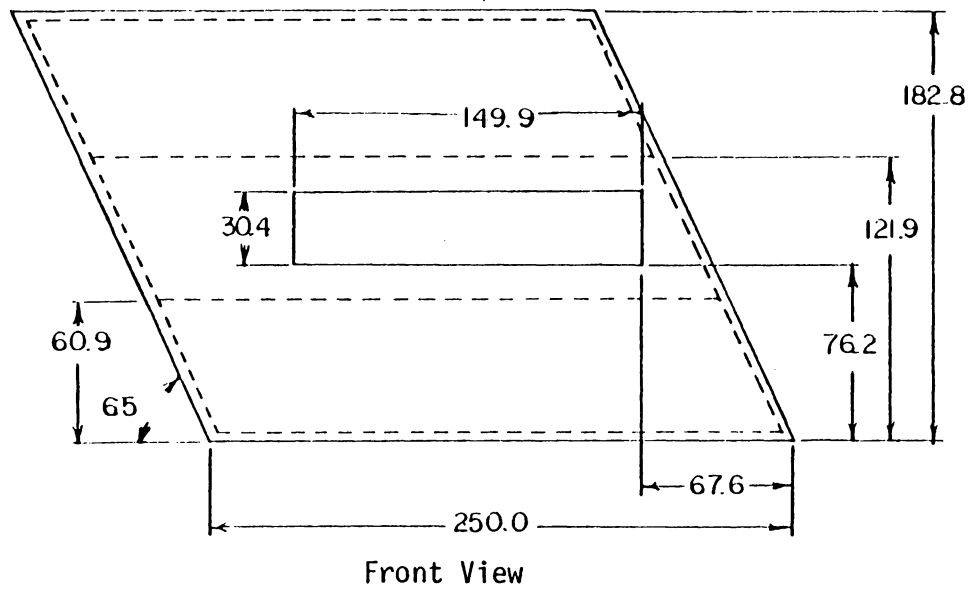


Figure 2.9 C_p distribution along the plate calculated from the Panel Code.

WALLBUMP EXTENSION
(MAIN SECTION)



Side View

Figure 2.10 Middle section of the wall bump. All dimensions in cm.

WALLBUMP INSERT PANEL

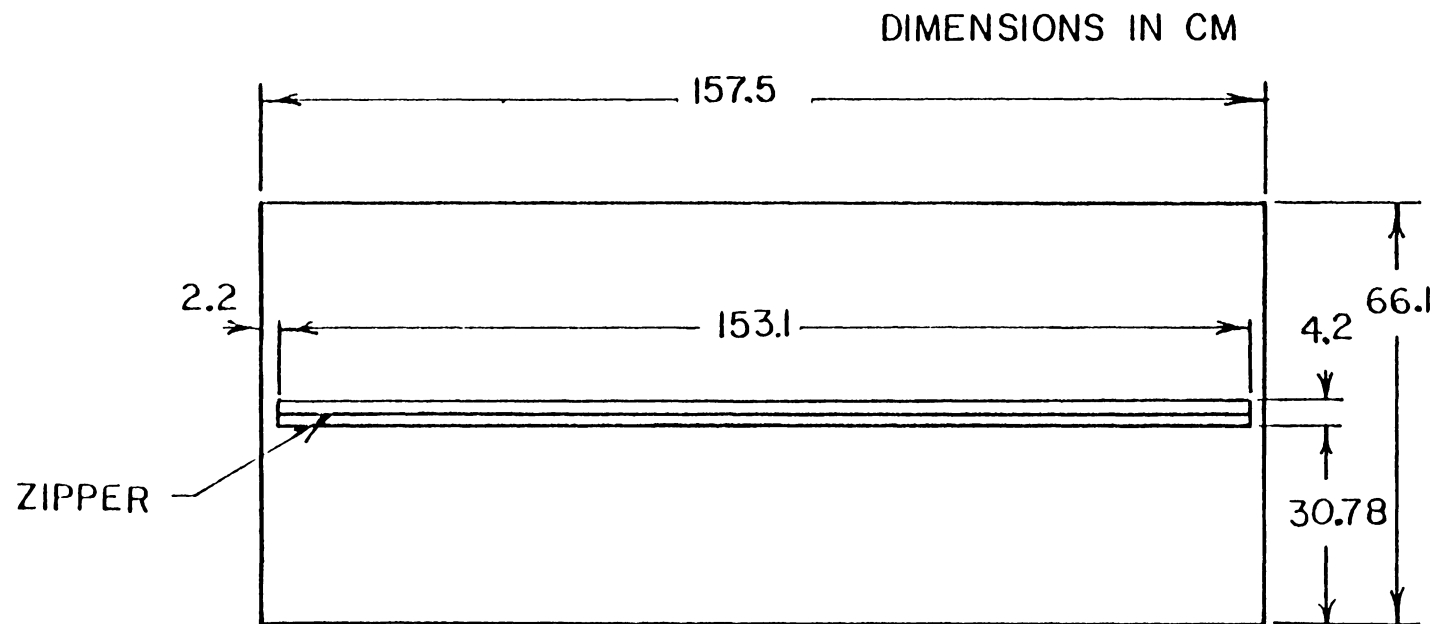
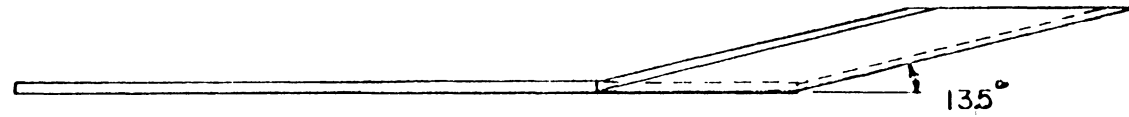


Figure 2.11 Panel insert for the wall bump.

WALLBUMP EXTENSION (TOTAL)



DIMENSIONS IN CM

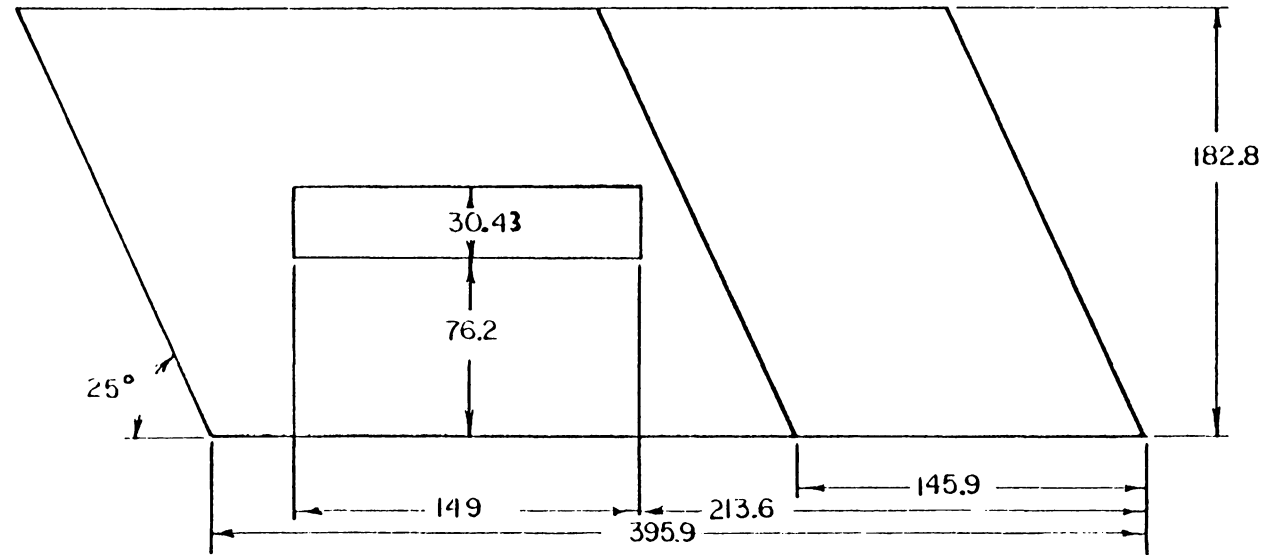


Figure 2.12 Wall bump extension.

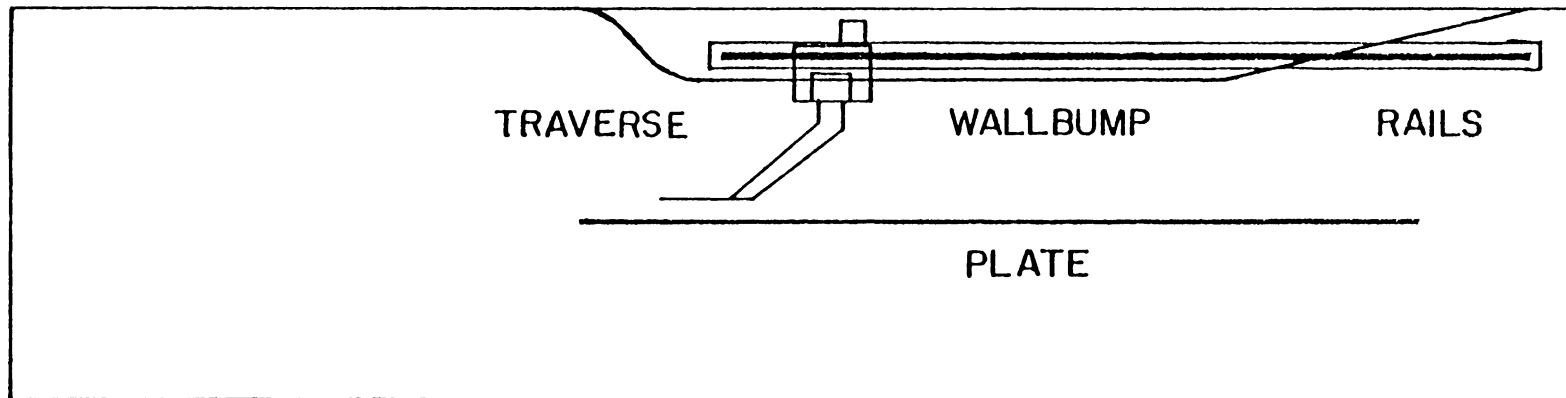


Figure 2.13 Location of the traverse with respect to the plate and wall bump.

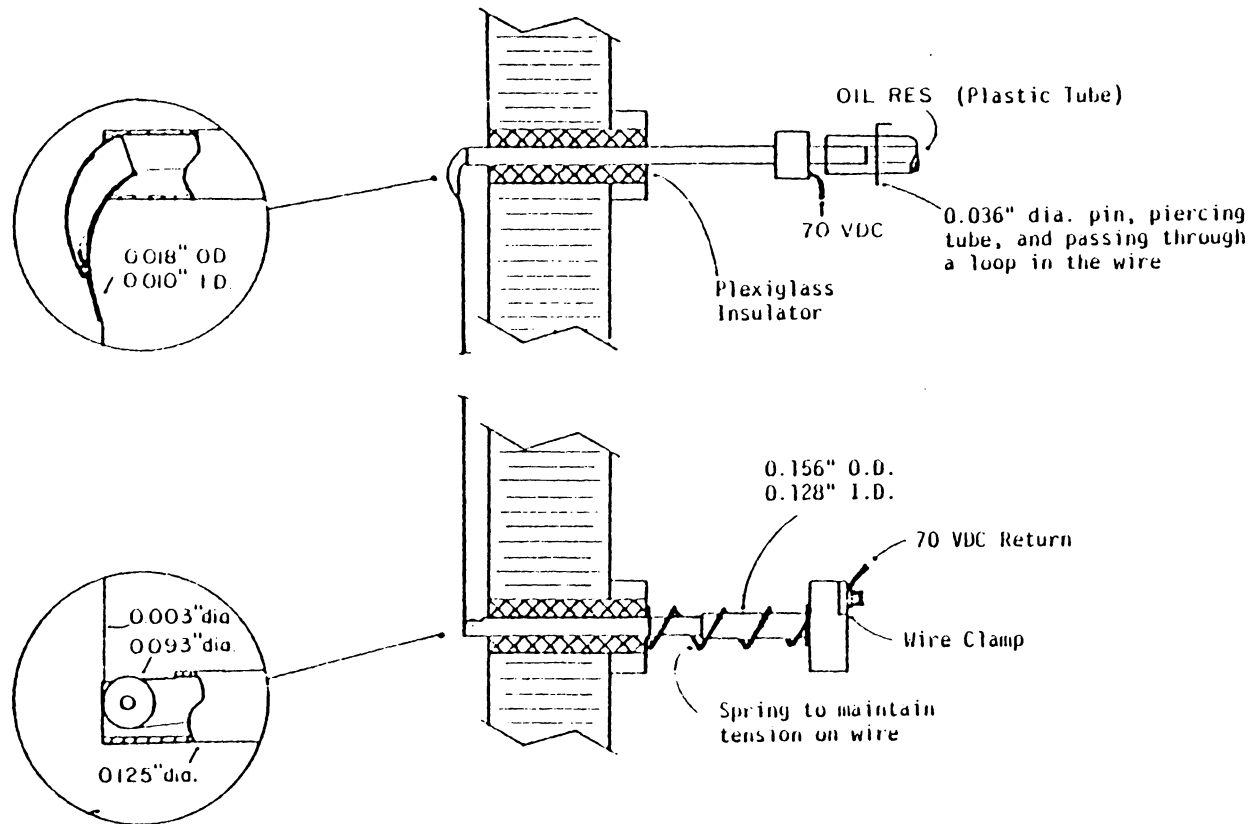


Figure 2.14 Smoke wire installation on the swept flat plate.
Span: 50 cm.
Wire: 0.076 mm (#40 AWG) stainless steel.

SCHEMATIC OF THE HOT-WIRE
ANEMOMETER SIGNAL PROCESSING

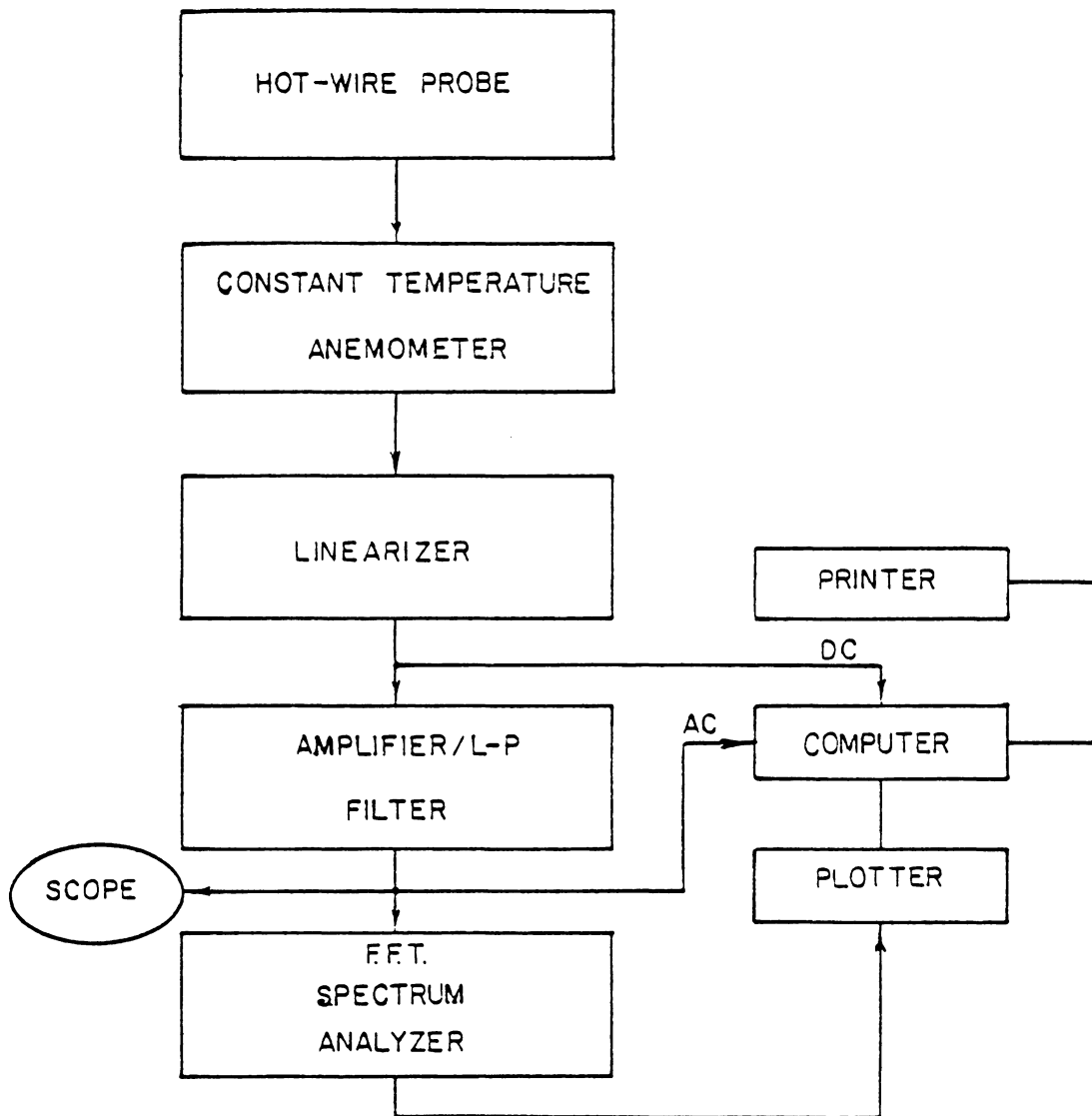


Figure 3.1 Schematic of the hot-wire anemometer signal processing.

BOUNDARY-LAYER PROBE
STRAIGHT-WIRE

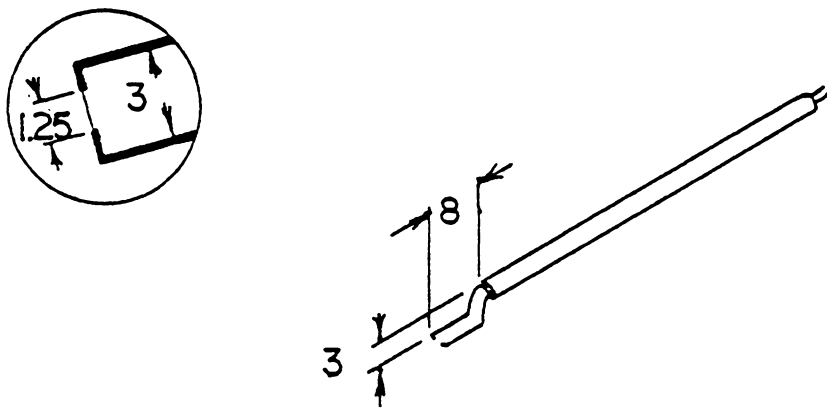


Figure 3.2 Diagram of the boundary layer probe.
All dimensions in mm.

BOUNDARY-LAYER PROBE
SLANT-WIRE

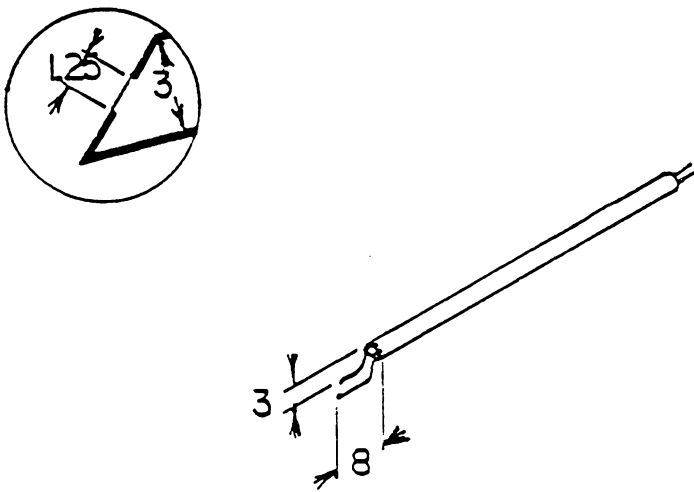


Figure 3.3 Diagram of the boundary layer probe.
All dimensions in mm.

TEST SECTION CONFIGURATION
SIDE VIEW AND FLOOR PLAN
DIMENSION IN CM.

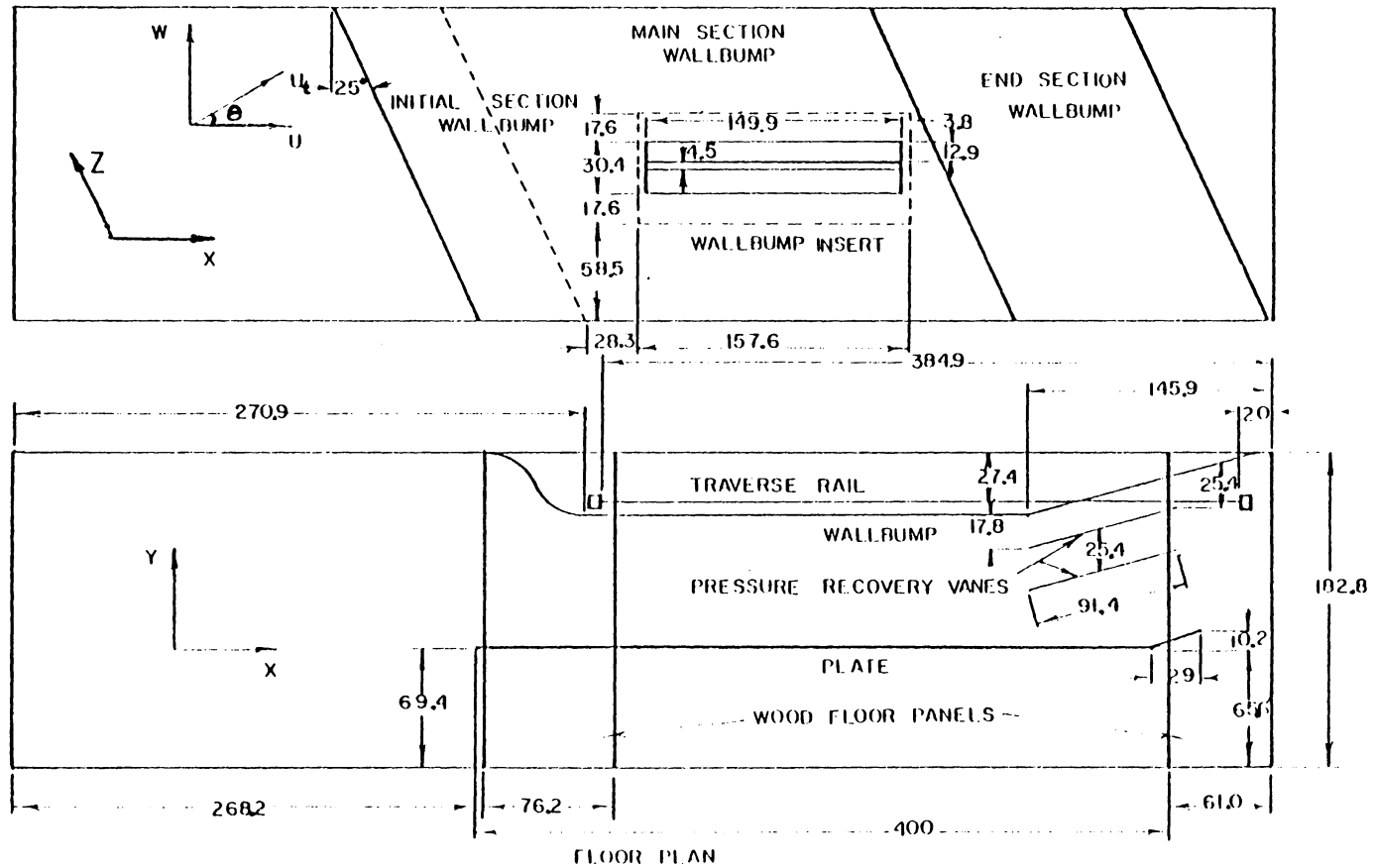


Figure 3.4 Final test section configuration.

TEST SECTION CONFIGURATION
SIDE VIEW AND FLOOR PLAN

DIMENSIONS IN CM

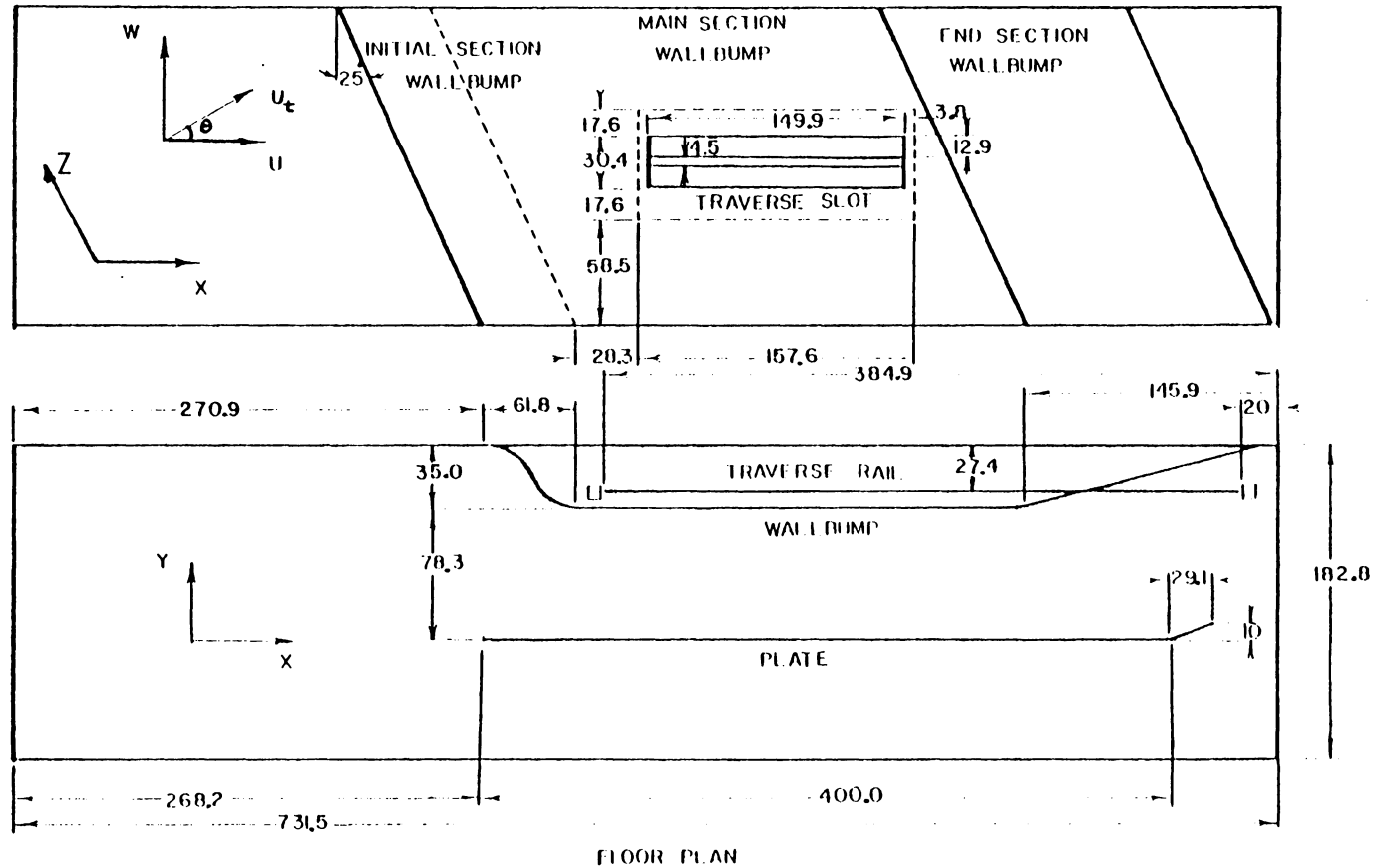


Figure 3.4a Original test section configuration.

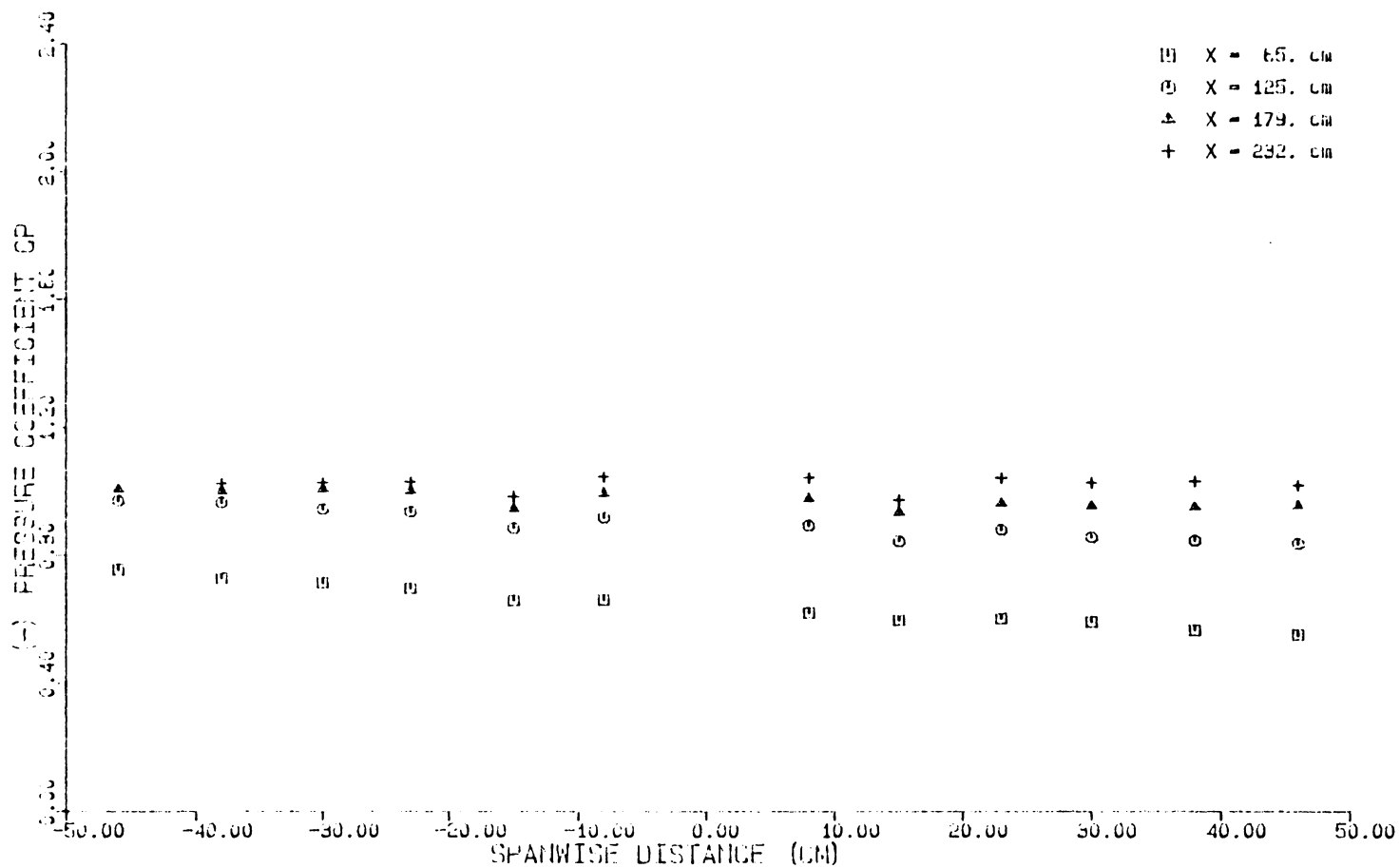


Figure 3.5 Spanwise pressure distribution at four chord locations.
Trailing edge flap set at 0.0 cm.

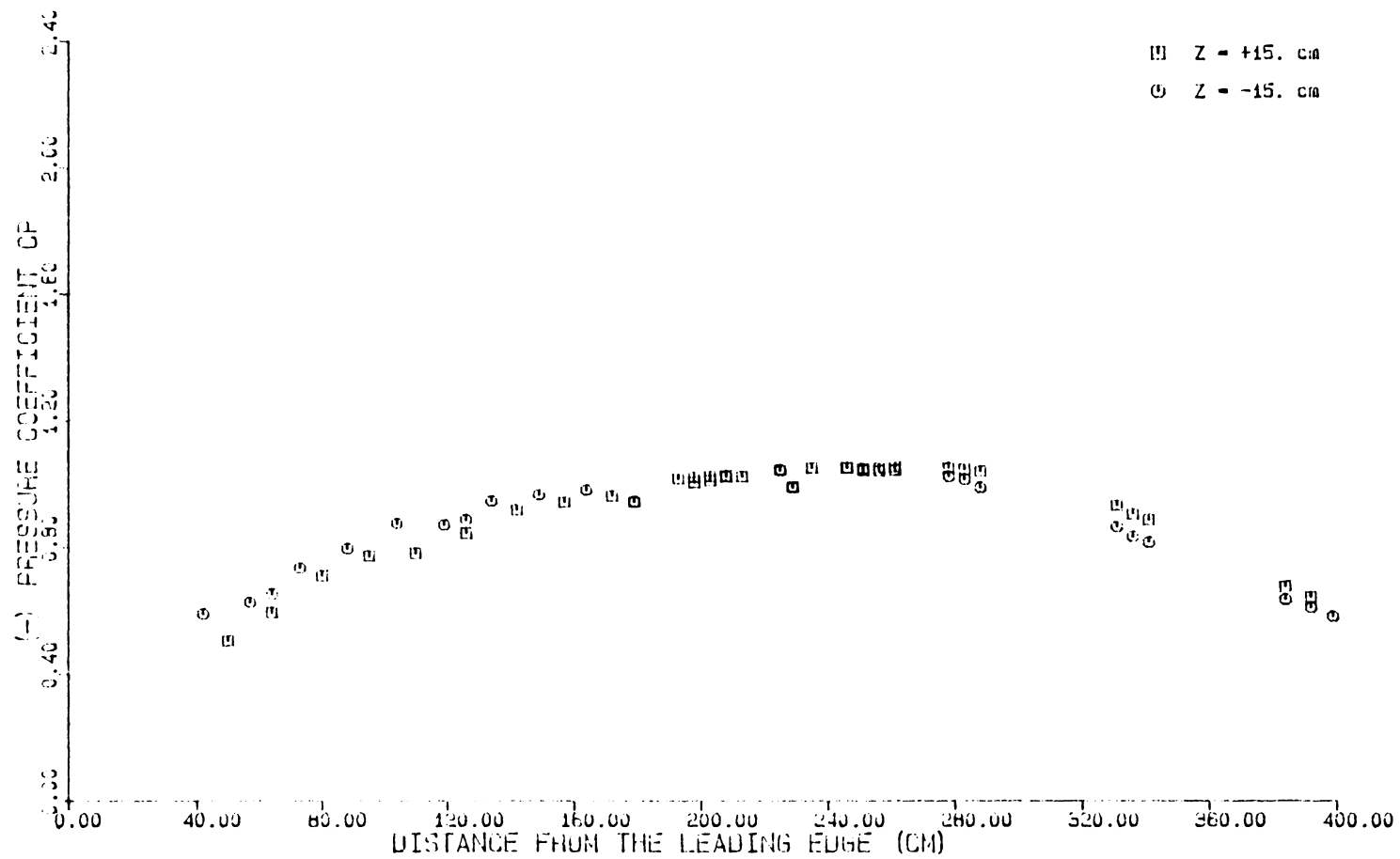


Figure 3.6 Chordwise pressure distribution at two span locations.
Trailing edge flap set at 0.0 cm.

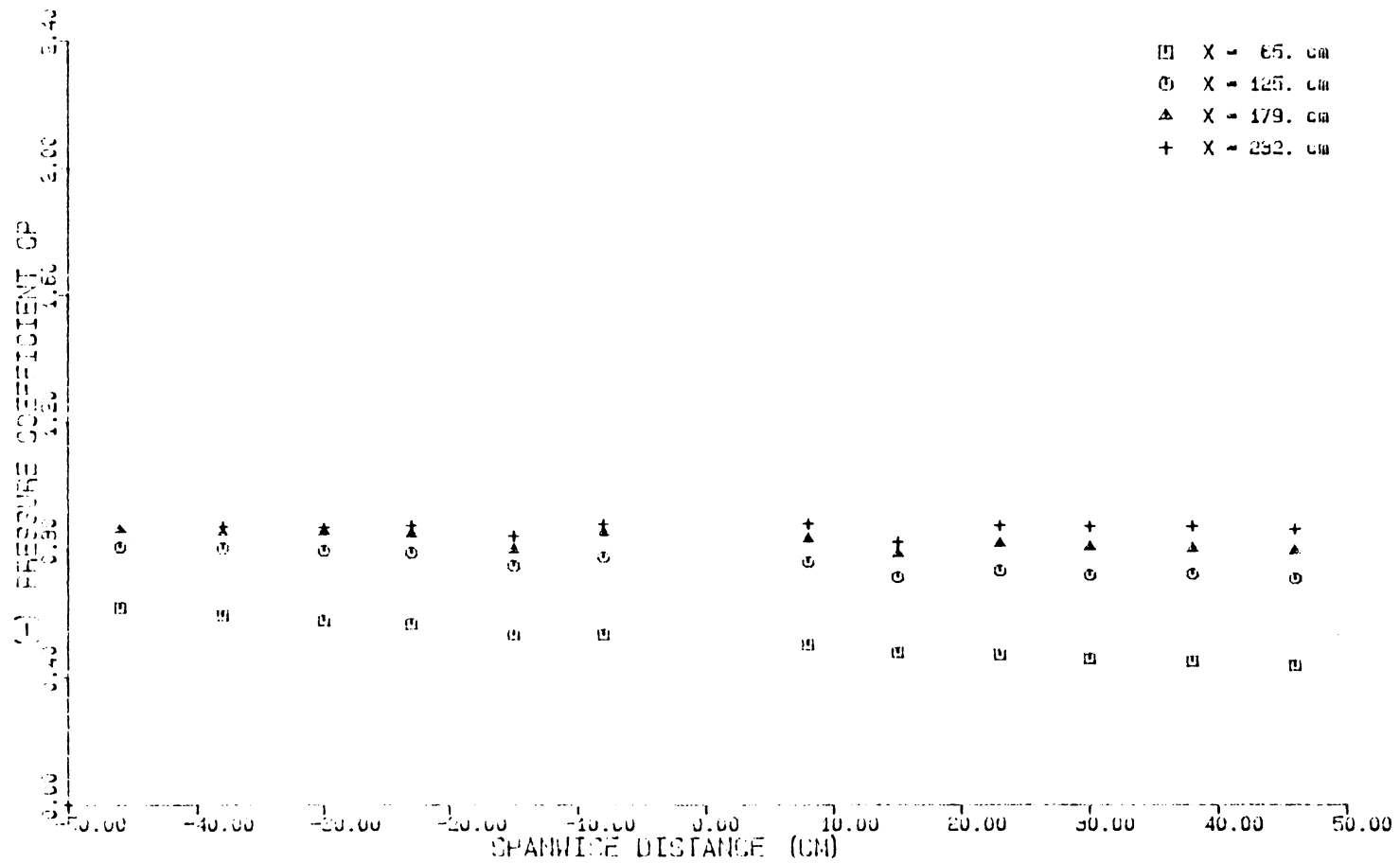


Figure 3.7 Spanwise pressure distribution at four chord locations.
Trailing edge flap set at 5.0 cm.

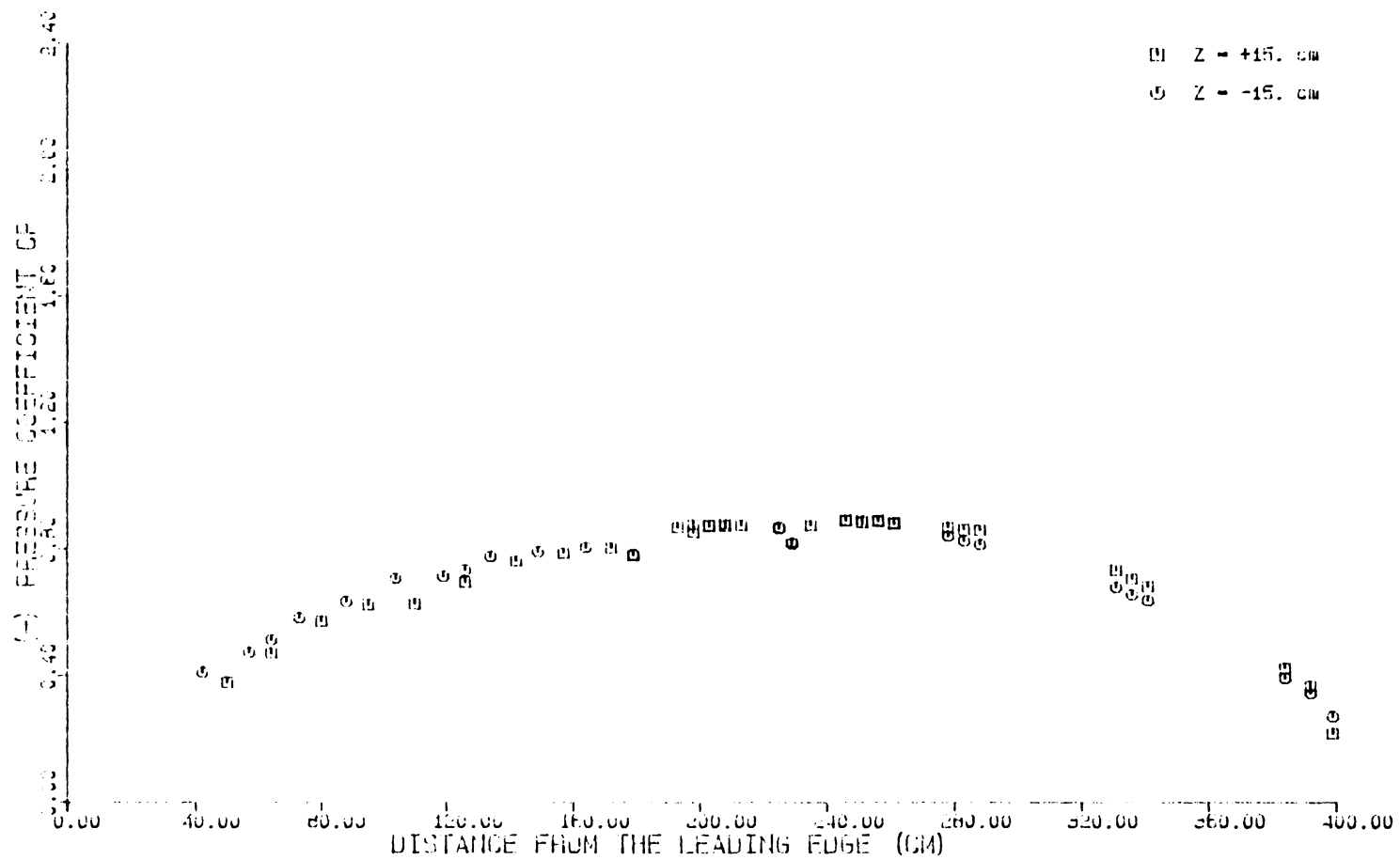


Figure 3.8 Chordwise pressure distribution at two span locations.
Trailing edge flap set at 5.0 cm.

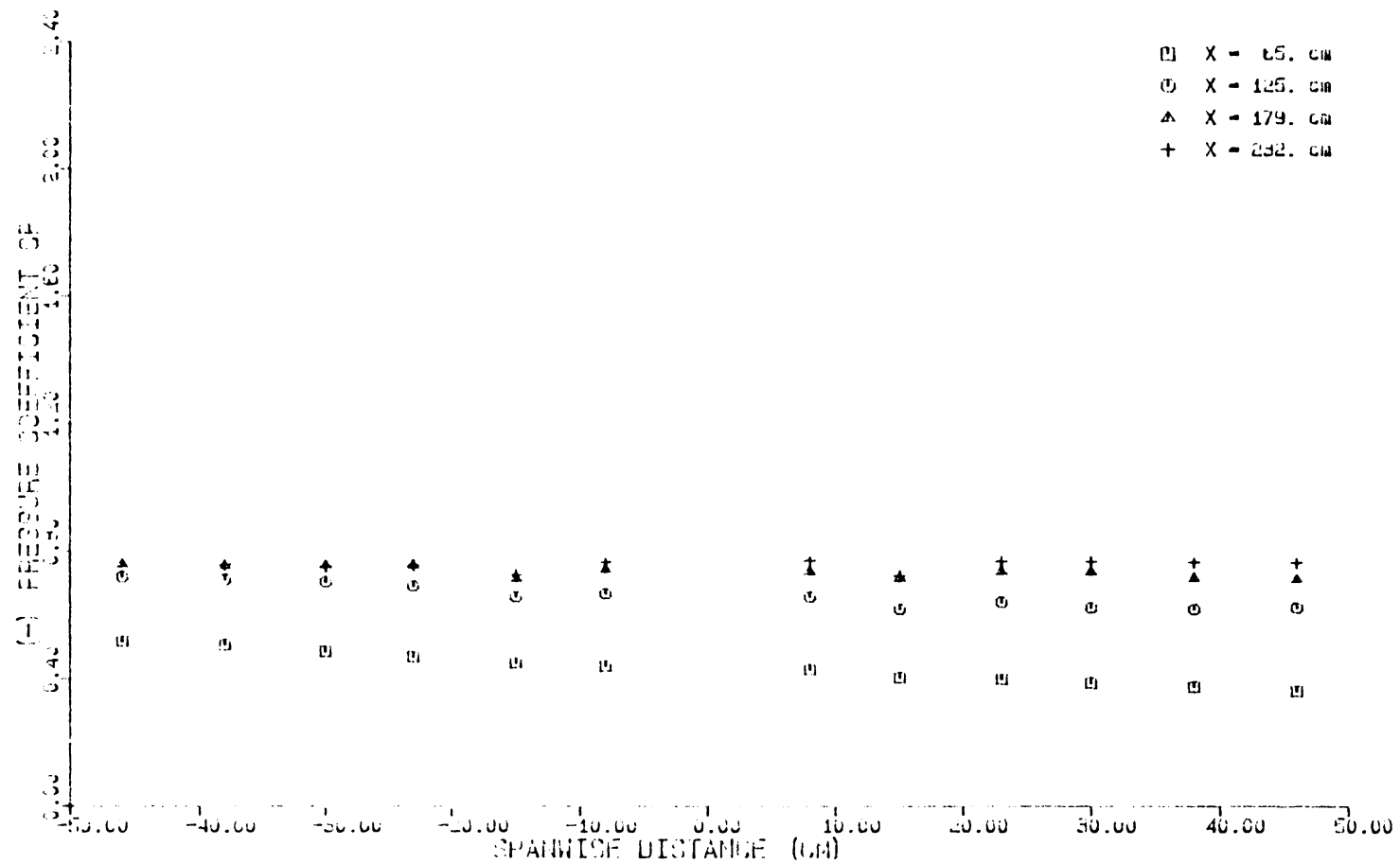


Figure 3.9 Spanwise pressure distribution at four chord locations.
Trailing edge flap set at 10.0 cm.

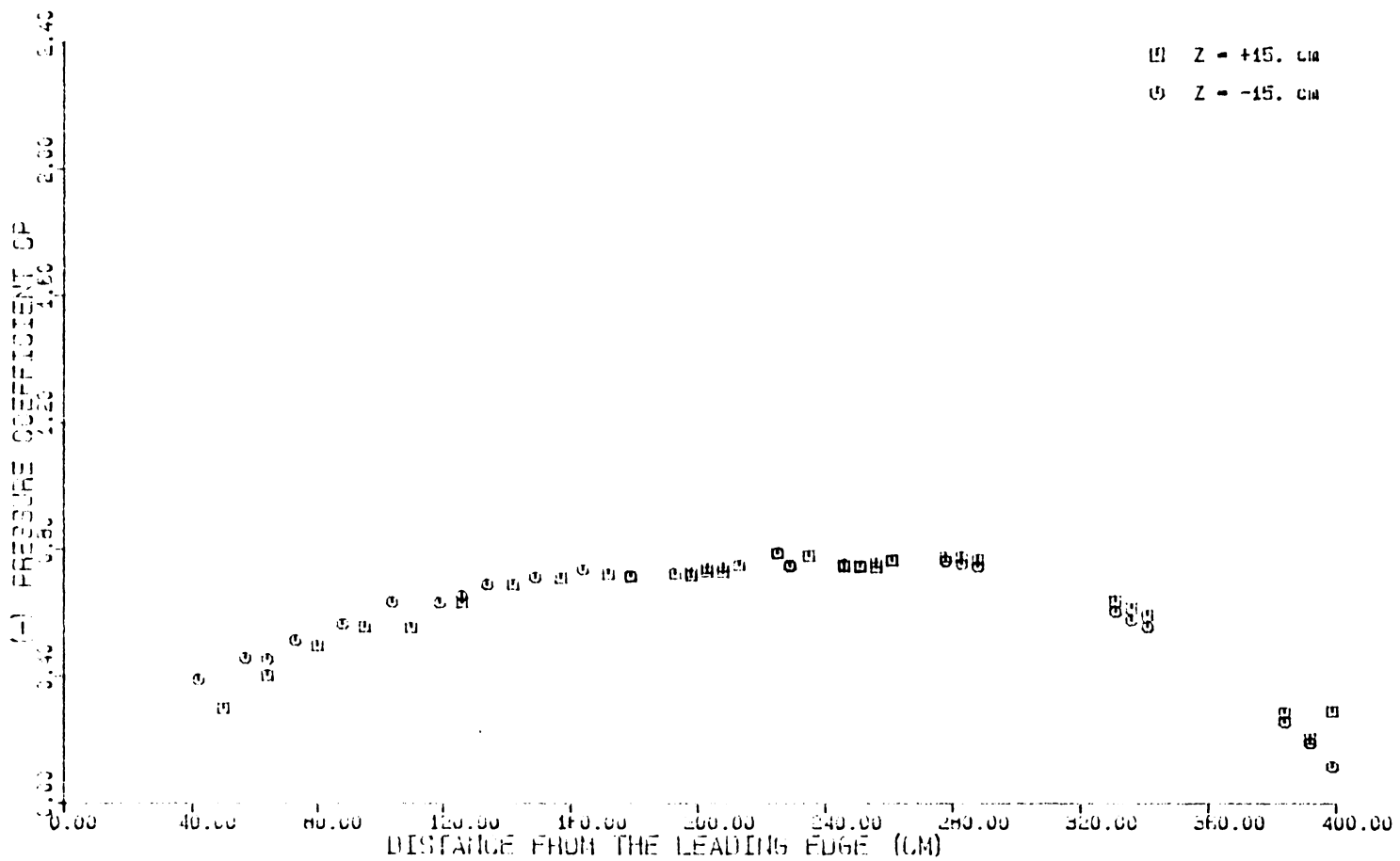


Figure 3.10 Chordwise pressure distribution at two span locations.
Trailing edge flap set at 10.0 cm.

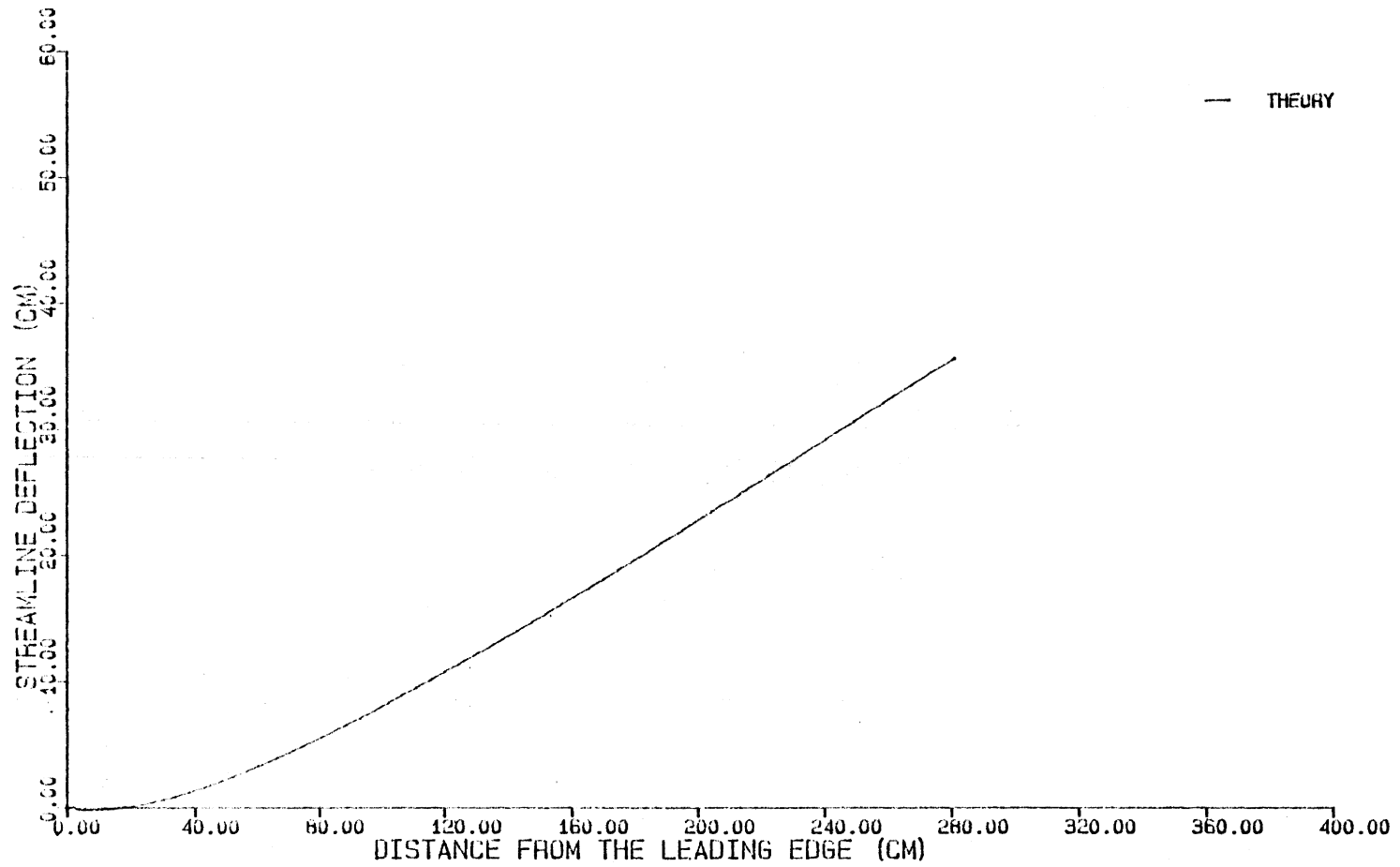


Figure 3.11 Streamline deflection along the plate in cm.

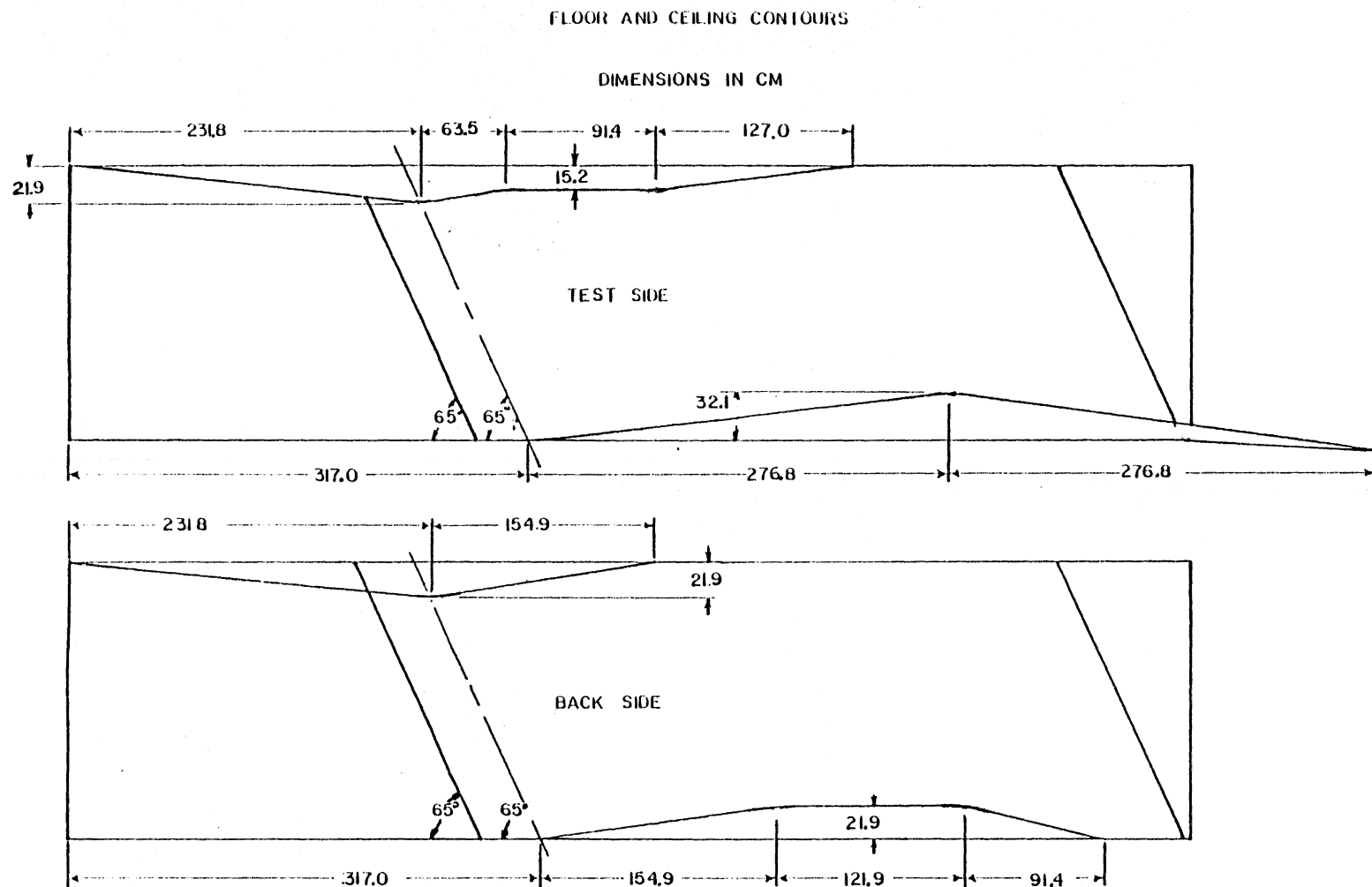


Figure 3.12 Floor and ceiling contours based on the inviscid streamlines.

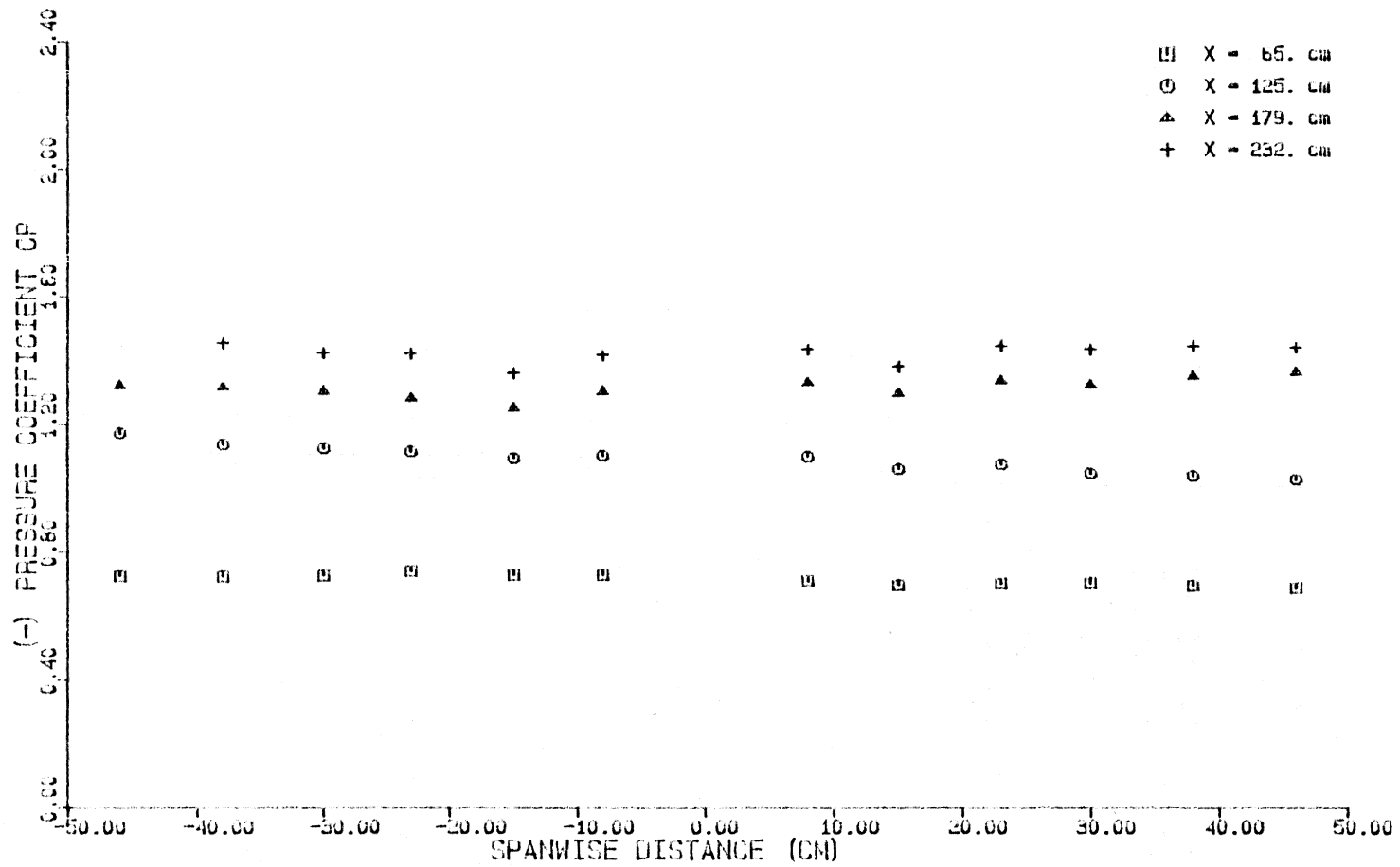


Figure 3.13 Spanwise pressure distribution at four chord locations.

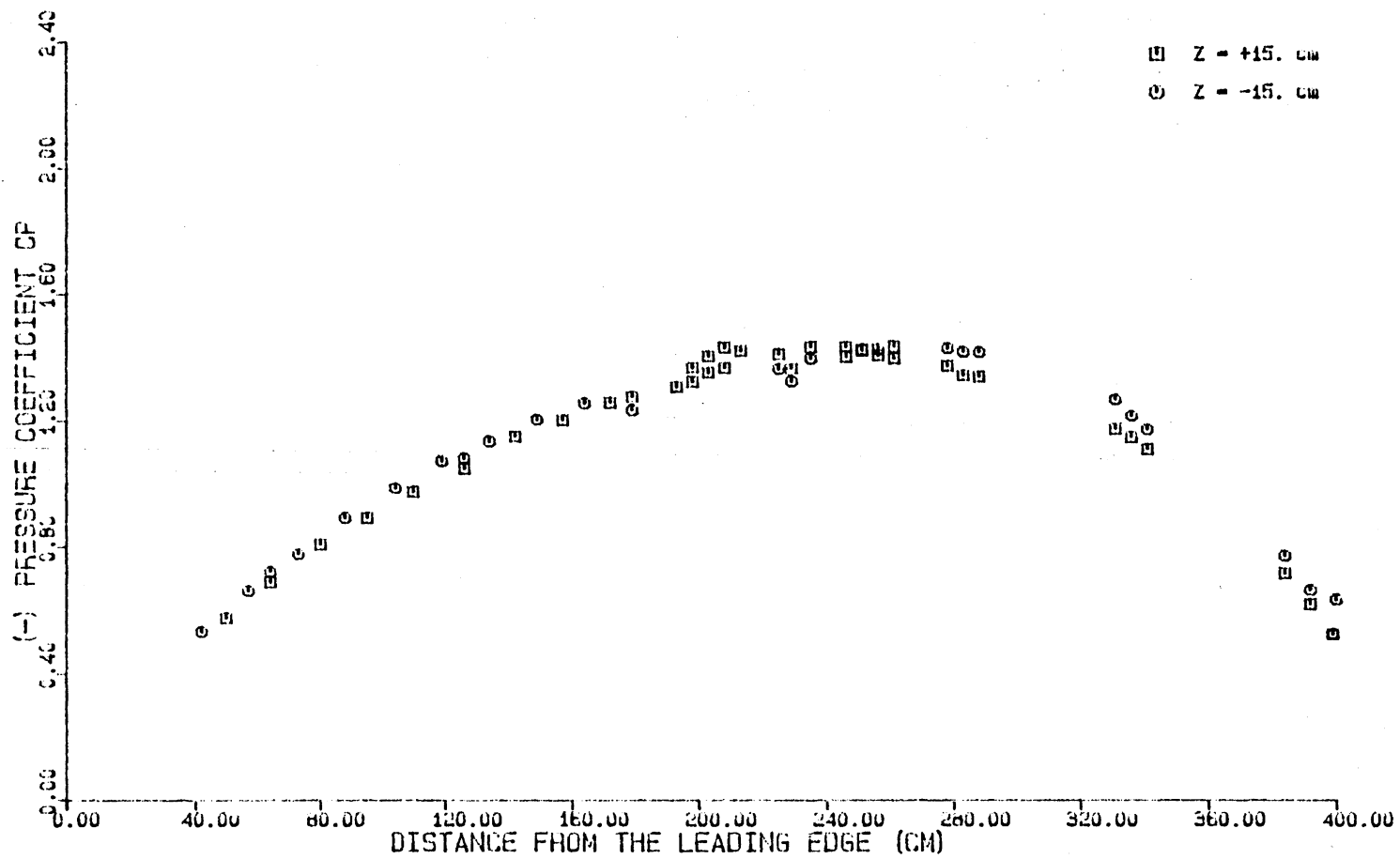


Figure 3.14 Chordwise pressure distribution at two span locations.

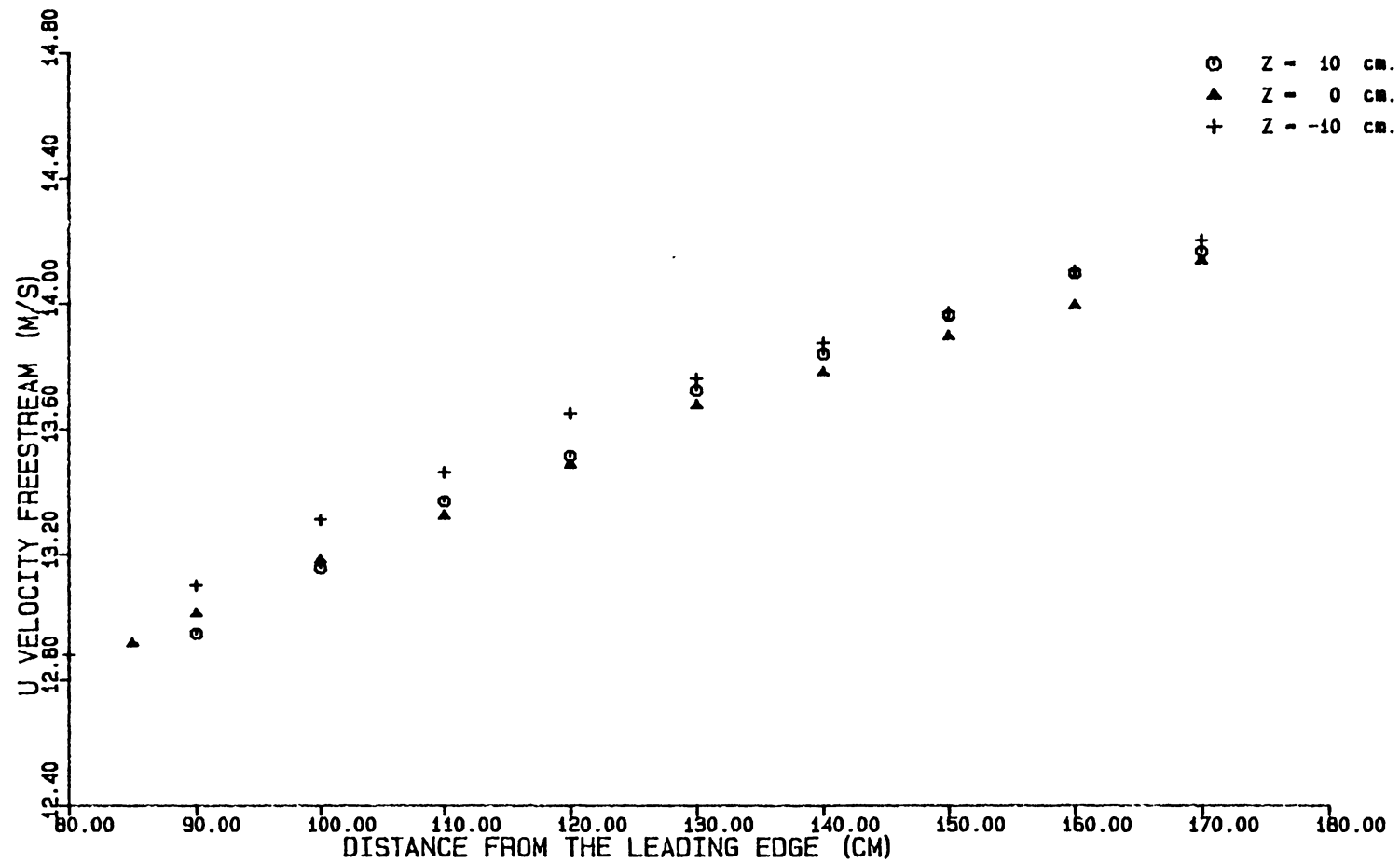


Figure 3.15 Variation of the U-velocity along the plate at three span locations. Reference velocity of 10 m/s.

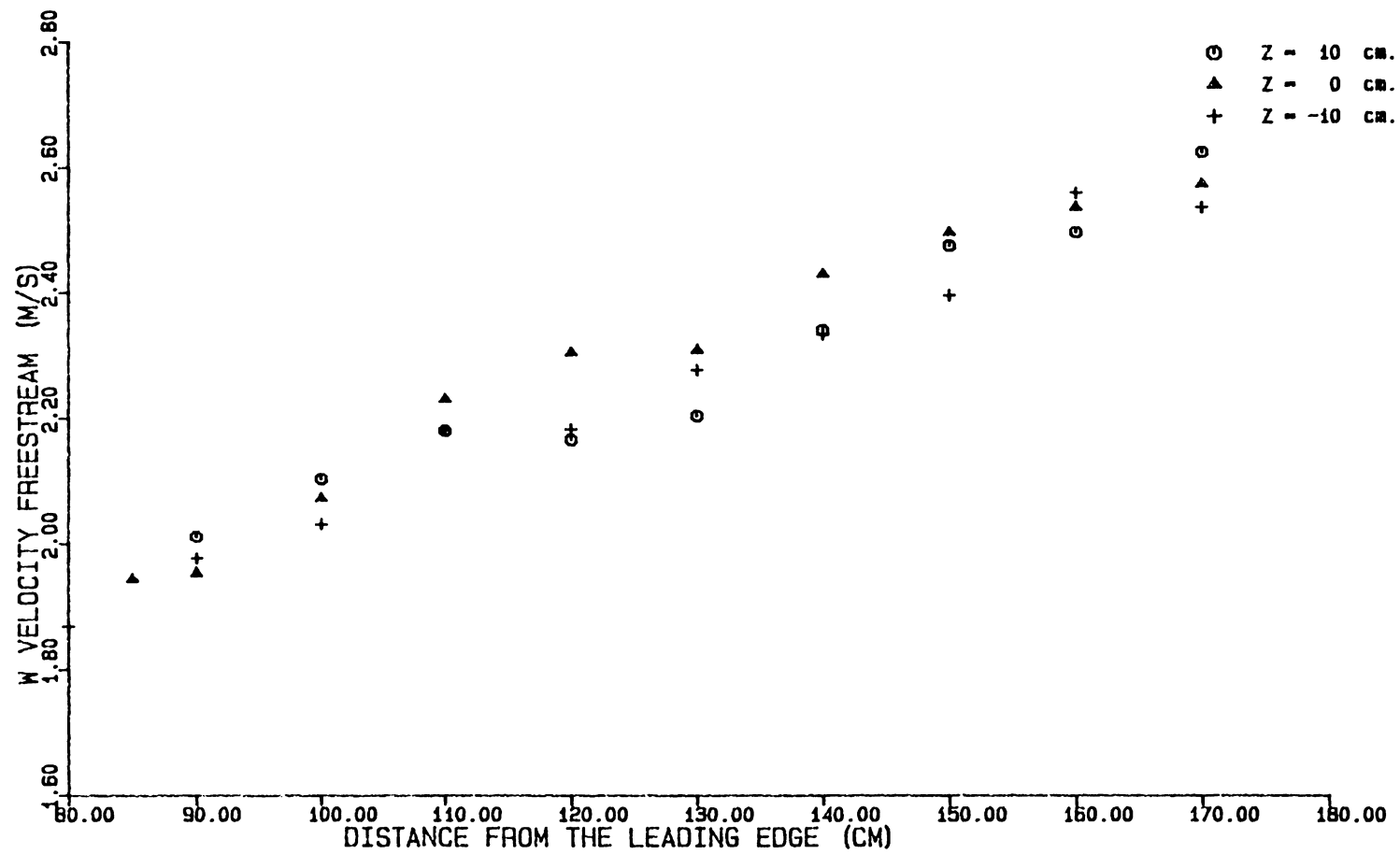


Figure 3.16 Variation of the W-velocity along the plate at three span locations.
Reference velocity of 10 m/s.

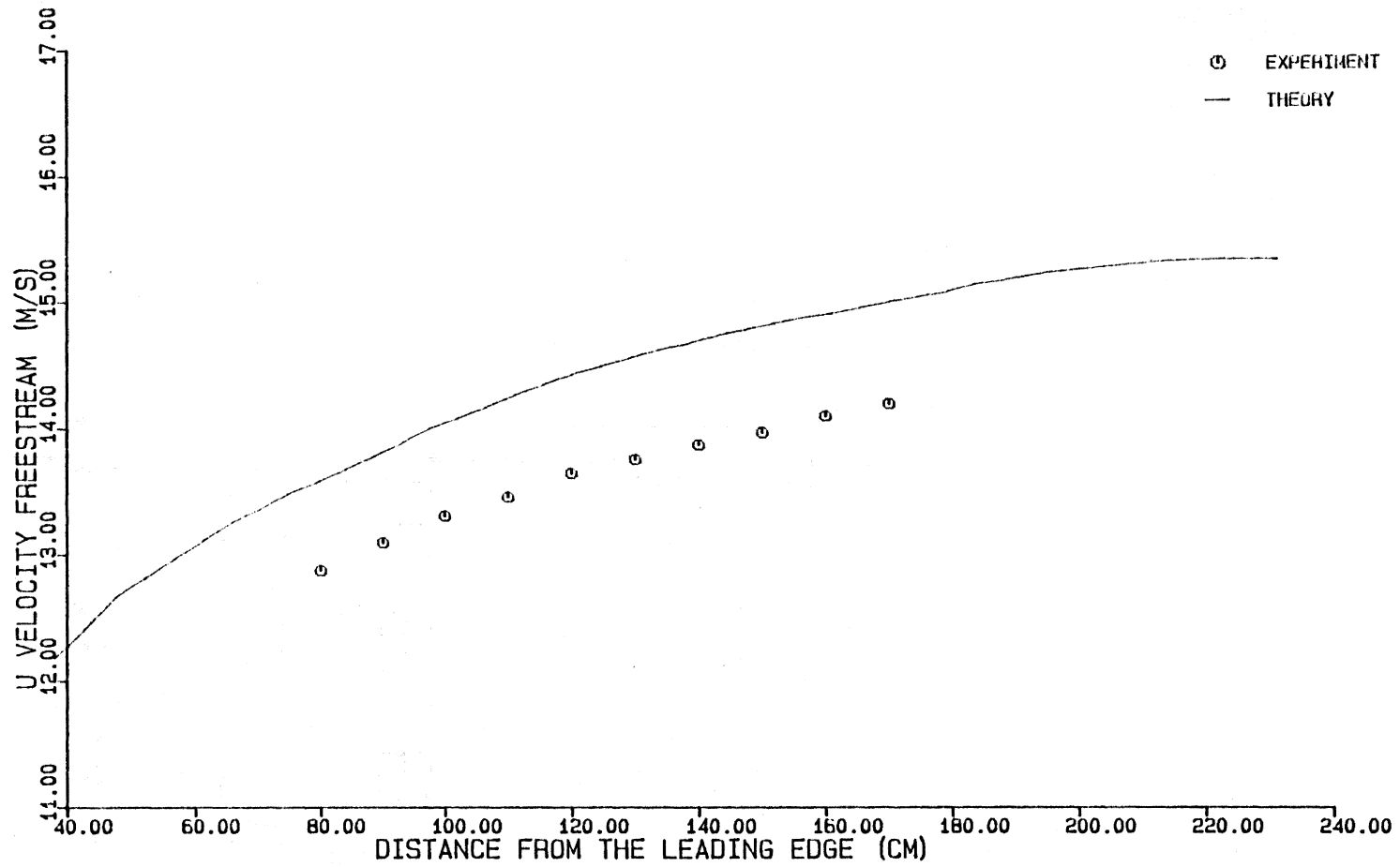


Figure 3.17 U-velocity along the plate at a reference velocity of 10 m/s.

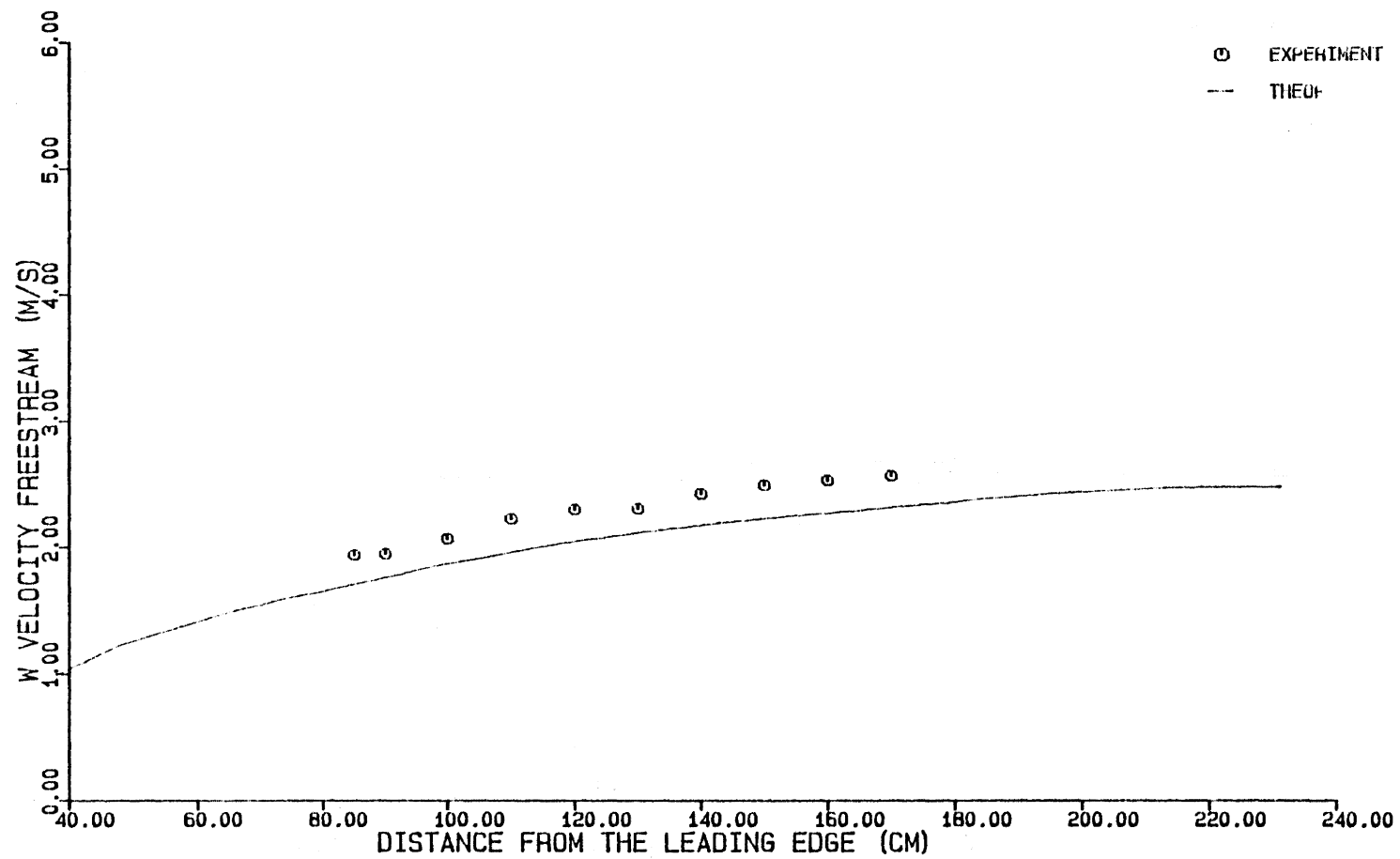


Figure 3.18 W-velocity along the plate at a reference velocity of 10 m/s.

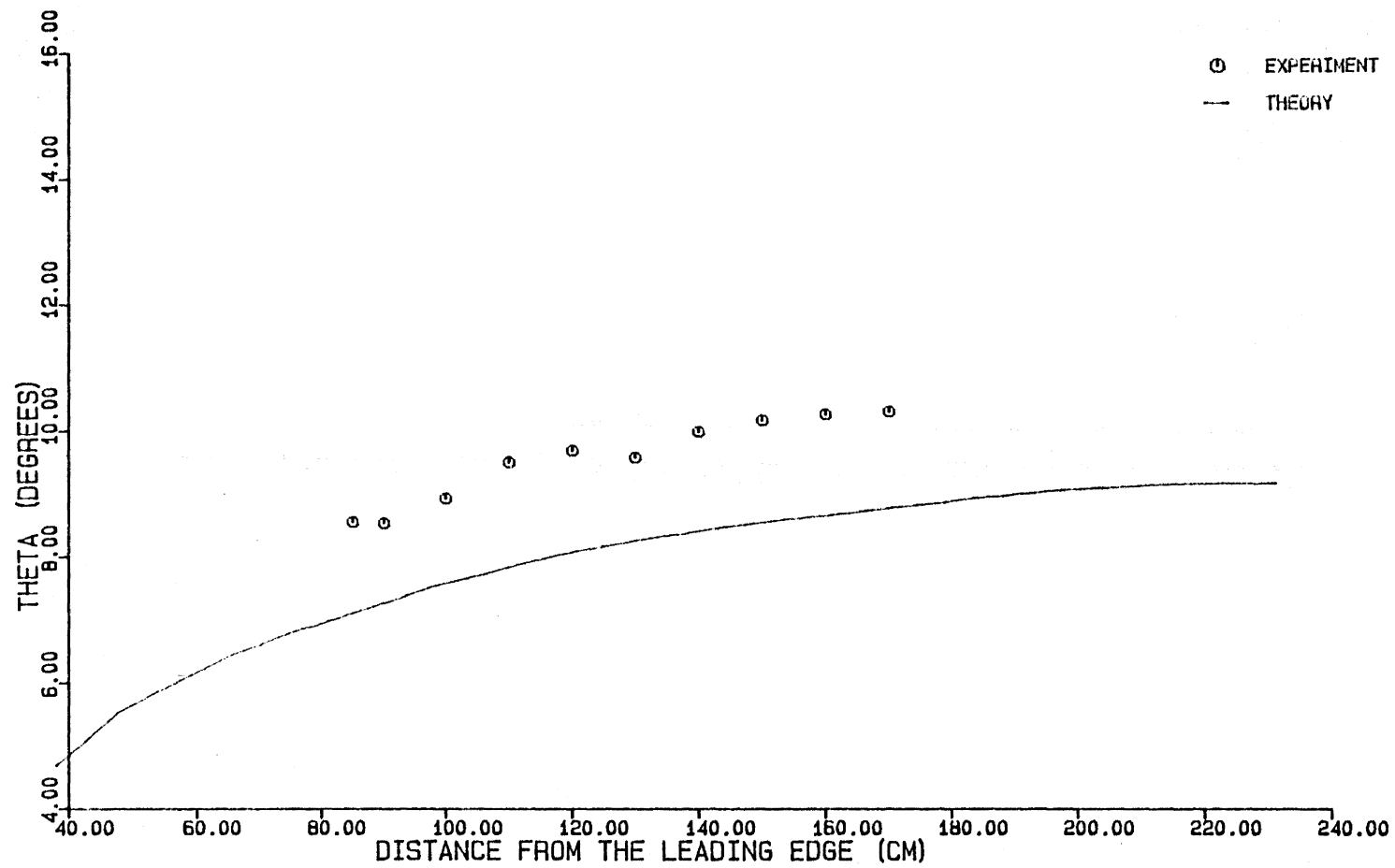


Figure 3.19 Angle of the streamlines along the plate at a reference velocity of 10 m/s.

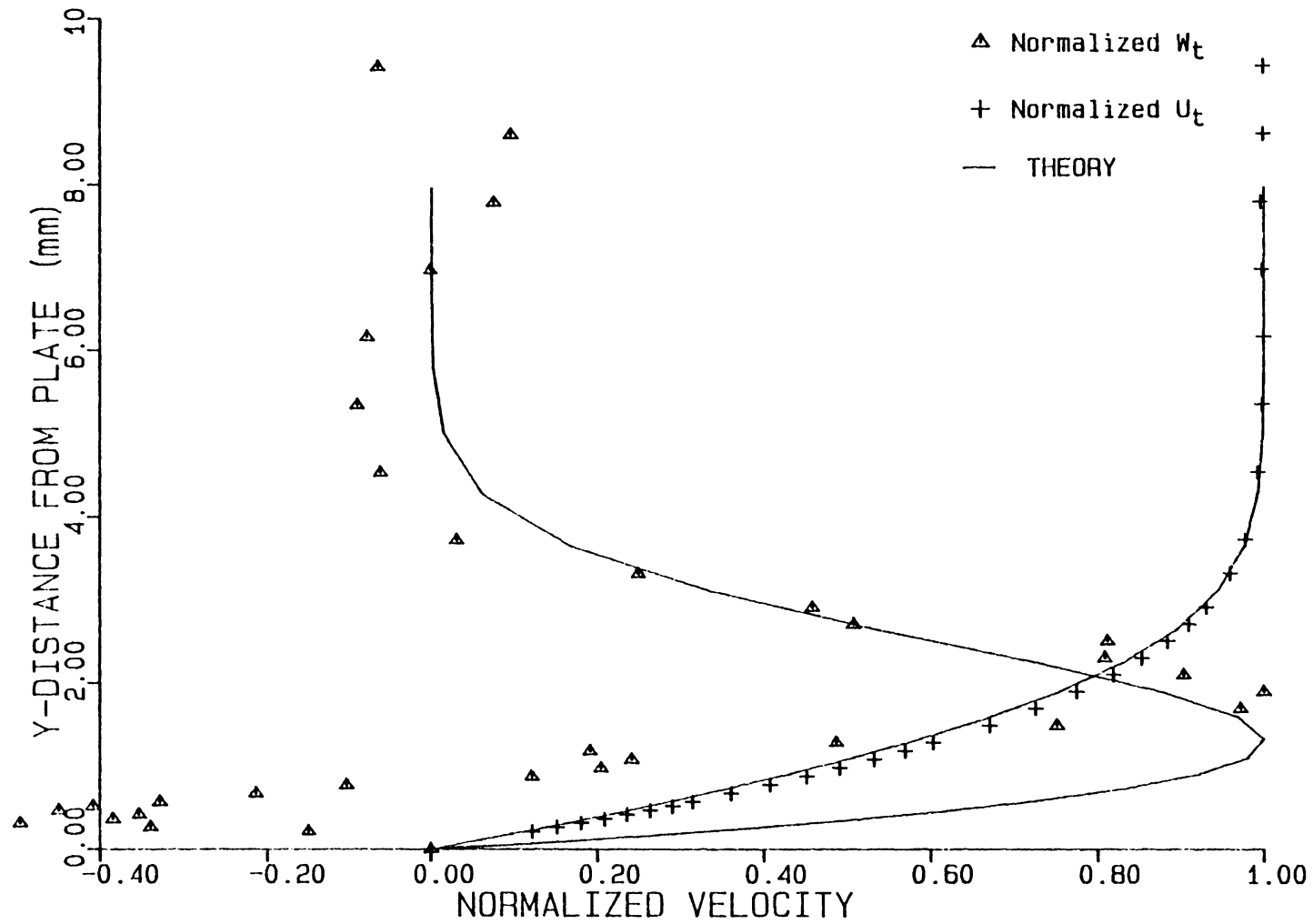


Figure 3.20 Tangential-flow velocity U_t/U_{et} and crossflow velocity W_t/W_{tmax} at $x=100$ cm and a reference velocity of 10 m/s.

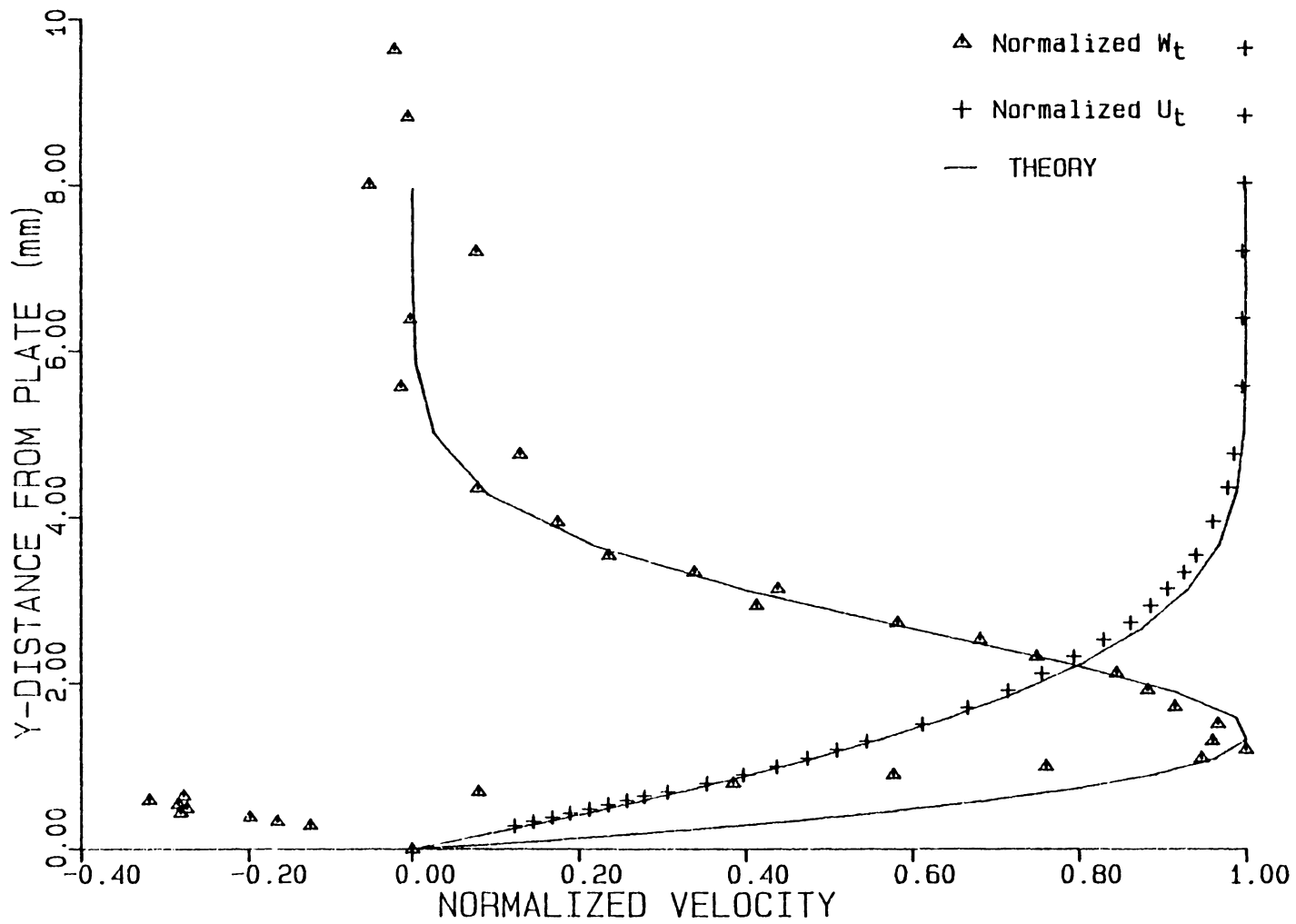


Figure 3.21 Tangential-flow velocity U_t/U_{et} and crossflow velocity W_t/W_{tmax} at $x=120$ cm and a reference velocity of 10 m/s.

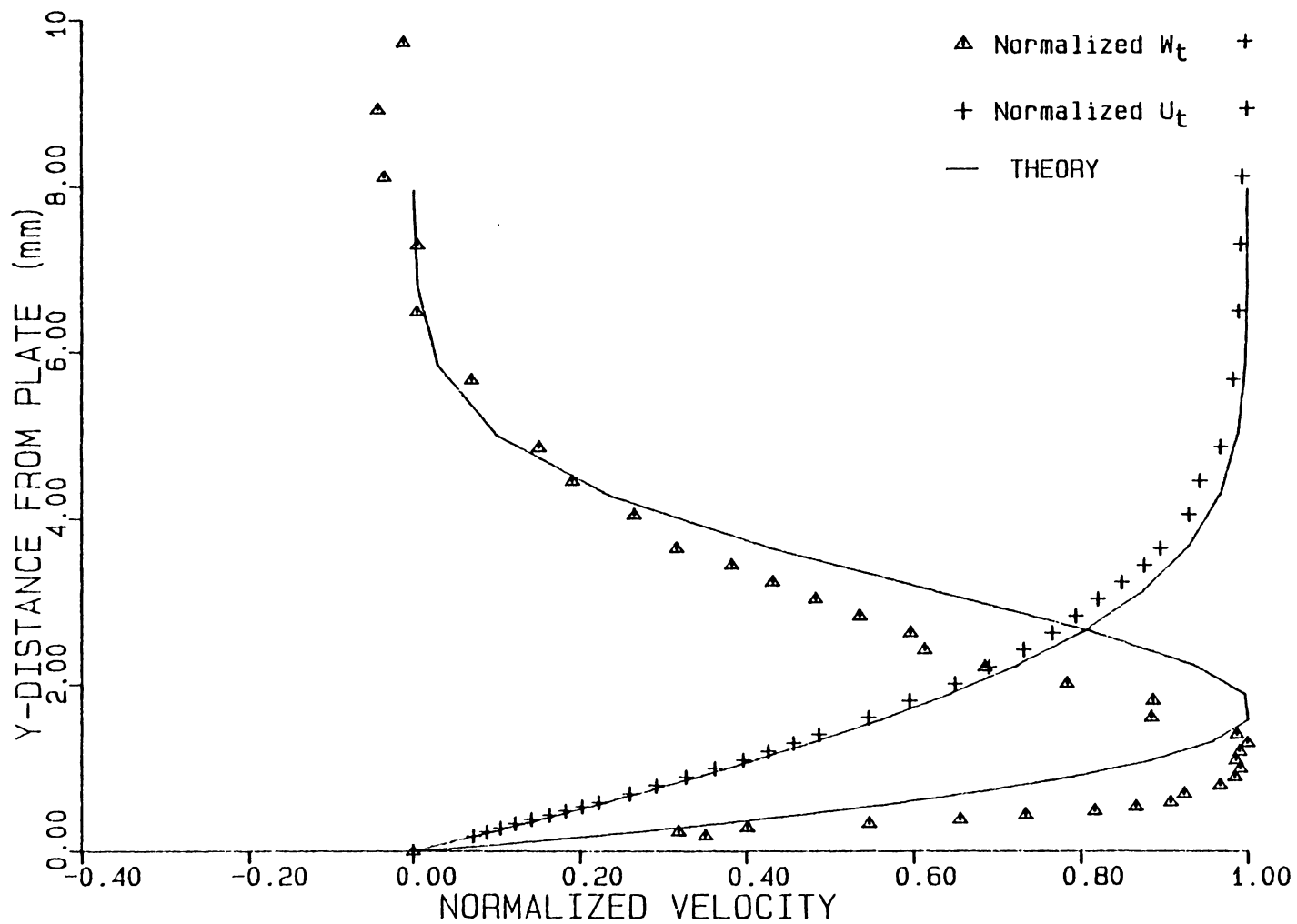


Figure 3.22 Tangential-flow velocity U_t/U_{et} and crossflow velocity W_t/W_{tmax} at $x=170$ cm and a reference velocity of 10 m/s.

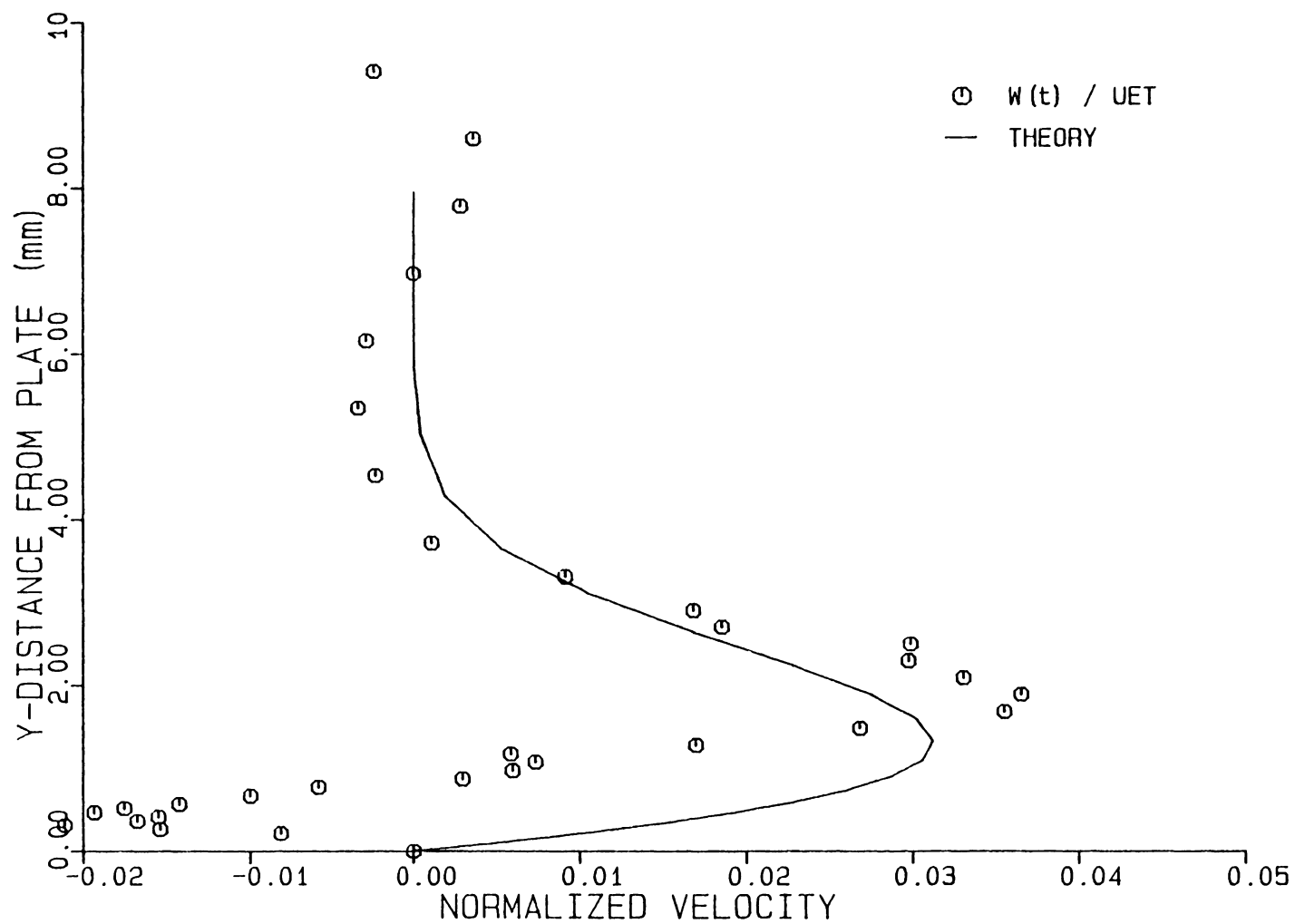


Figure 3.23 Crossflow velocity W_t/U_{et} at $x=100$ cm and a reference velocity of 10 m/s.

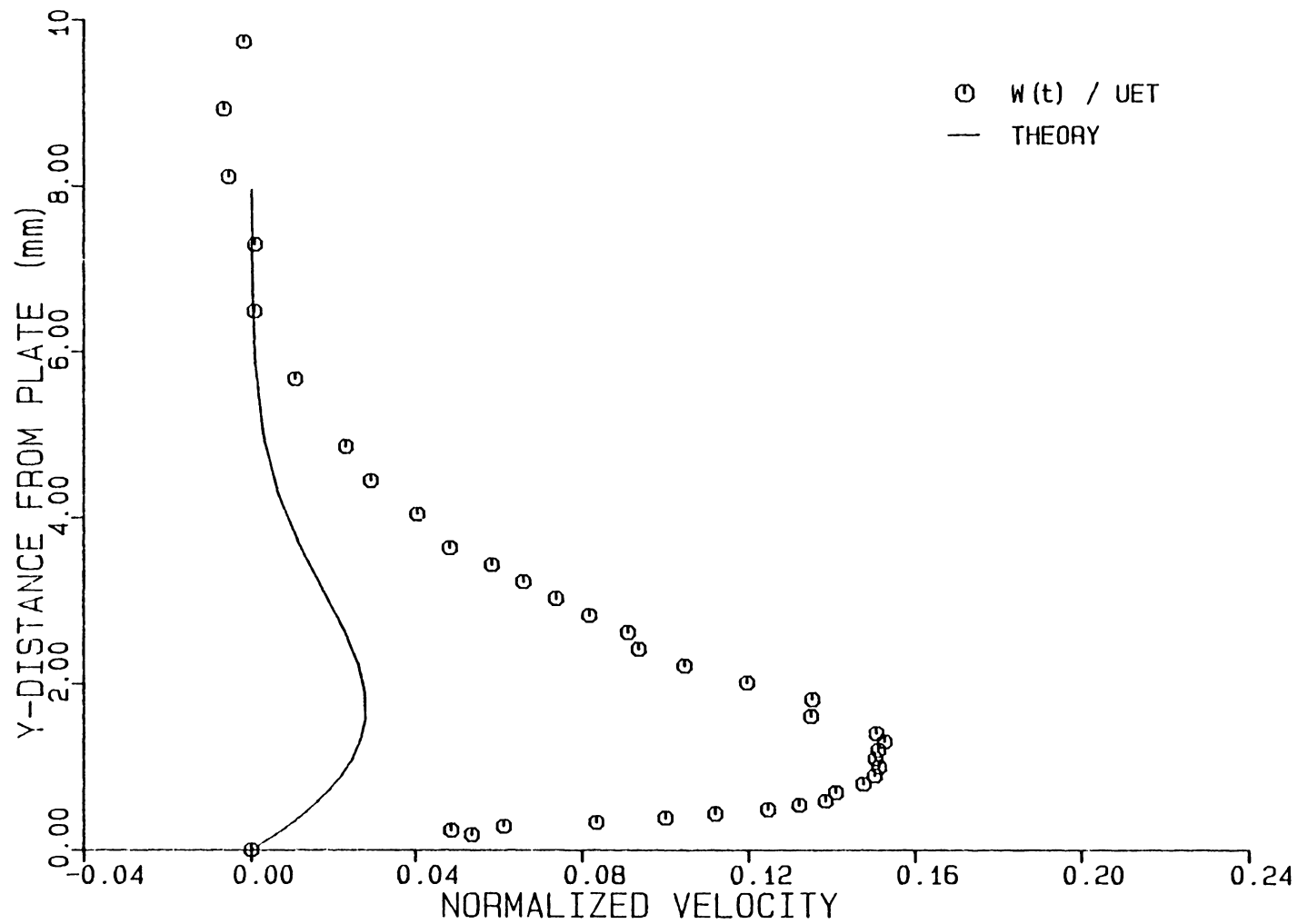


Figure 3.25 Crossflow velocity W_t/U_{et} at $x=170$ cm
and a reference velocity of 10 m/s.

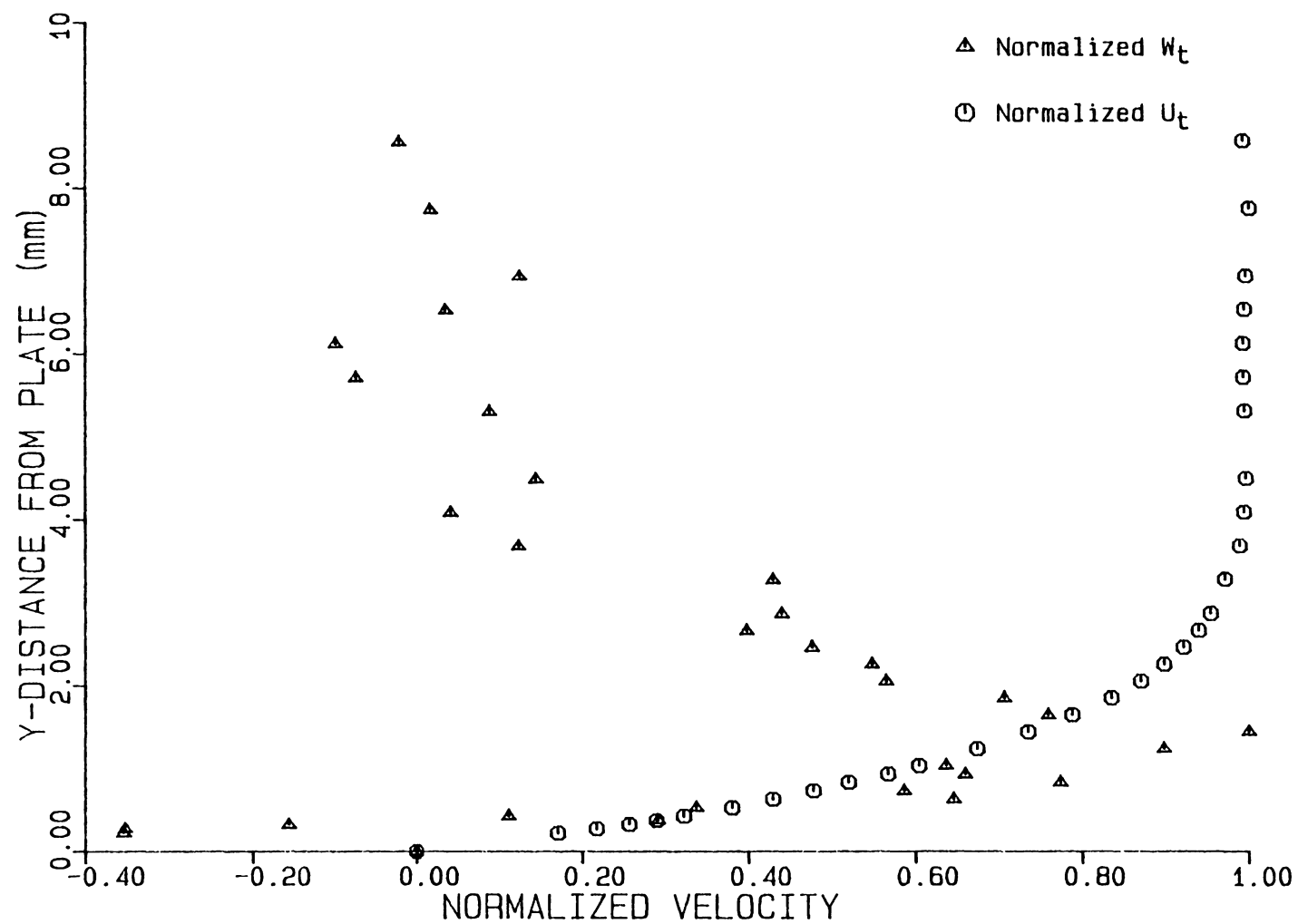


Figure 3.26 Tangential-flow velocity U_t/U_{et} and crossflow velocity W_t/W_{tmax} at $x=100$ cm and a reference velocity of 14 m/s.

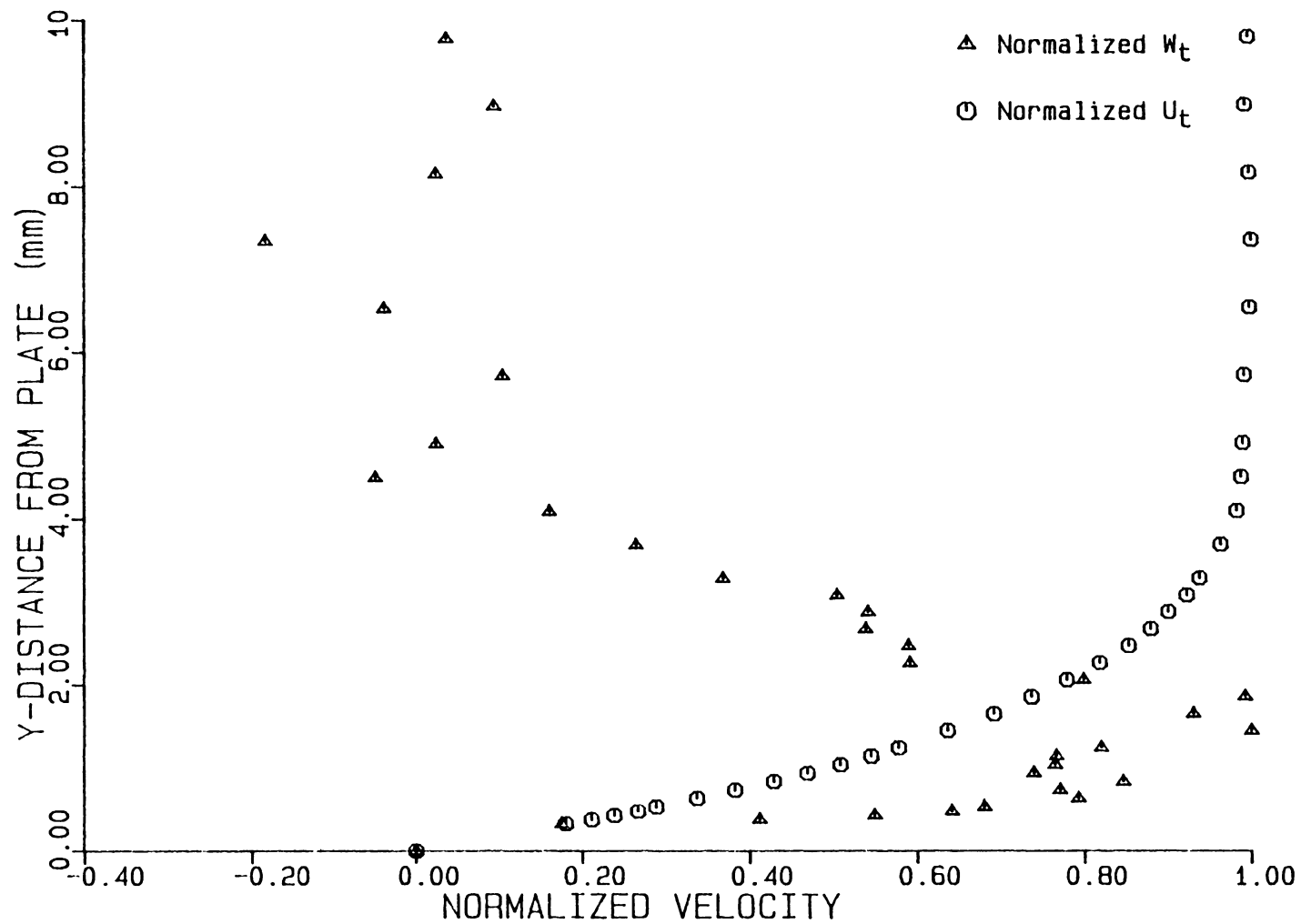


Figure 3.27 Tangential-flow velocity U_t/U_{et} and crossflow velocity W_t/W_{tmax} at $x=140$ cm and a reference velocity of 14 m/s.

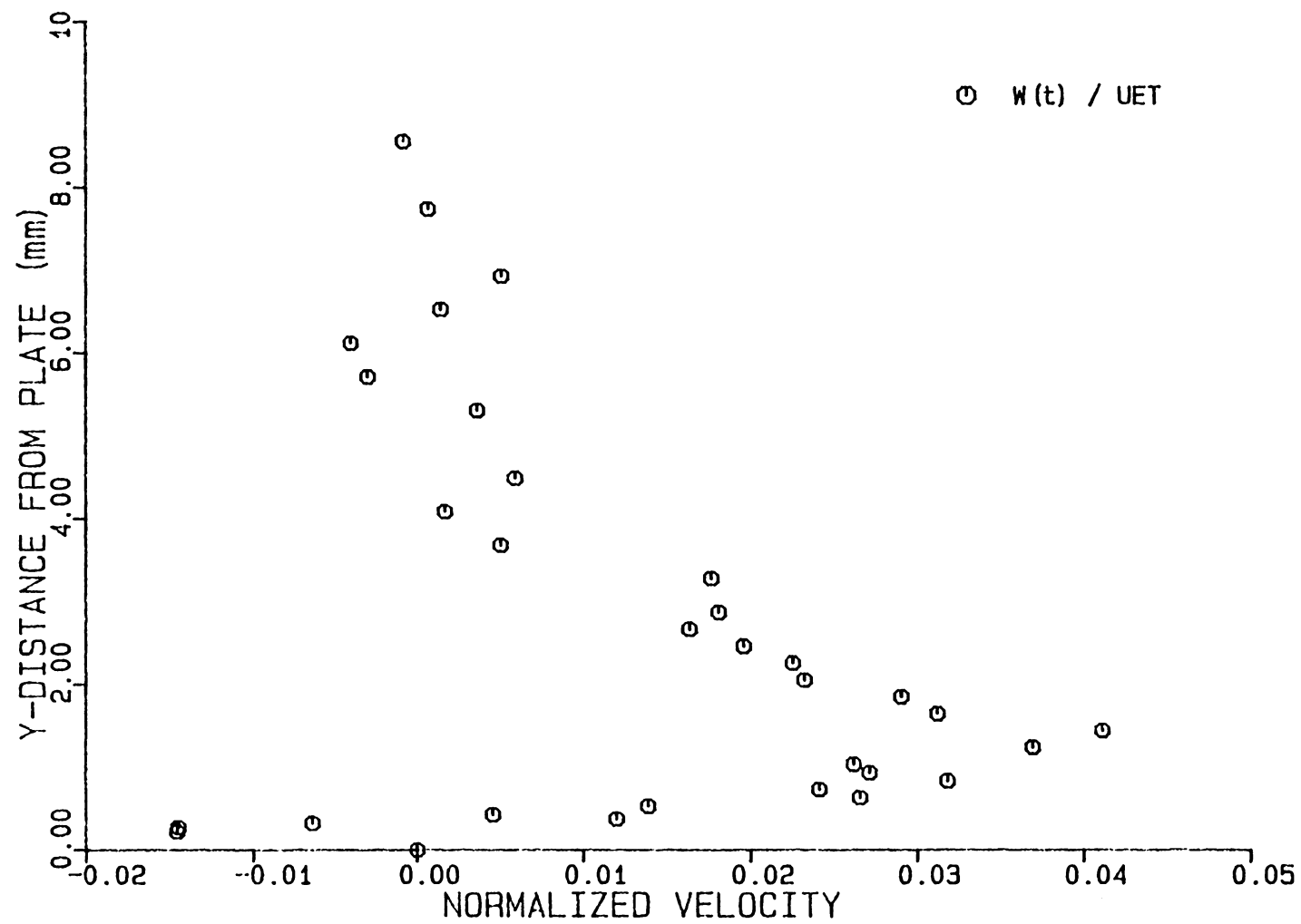


Figure 3.28 Crossflow velocity W_t/U_{et} at $x=100$ cm and a reference velocity of 14 m/s.

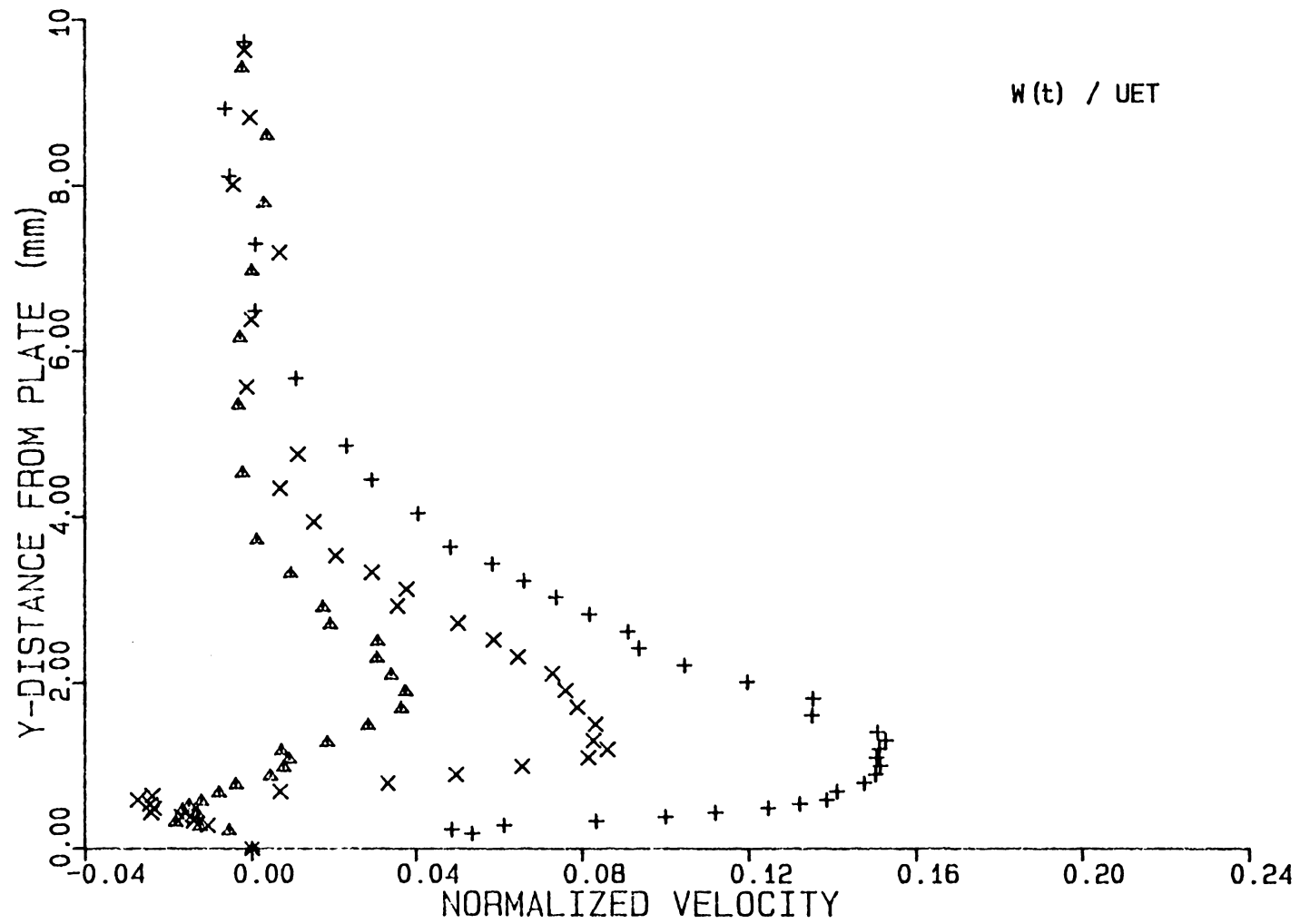


Figure 3.30 Crossflow velocity W_t/U_{et} at $x=100, 120$ and 170 cm and a reference velocity of 10 m/s.

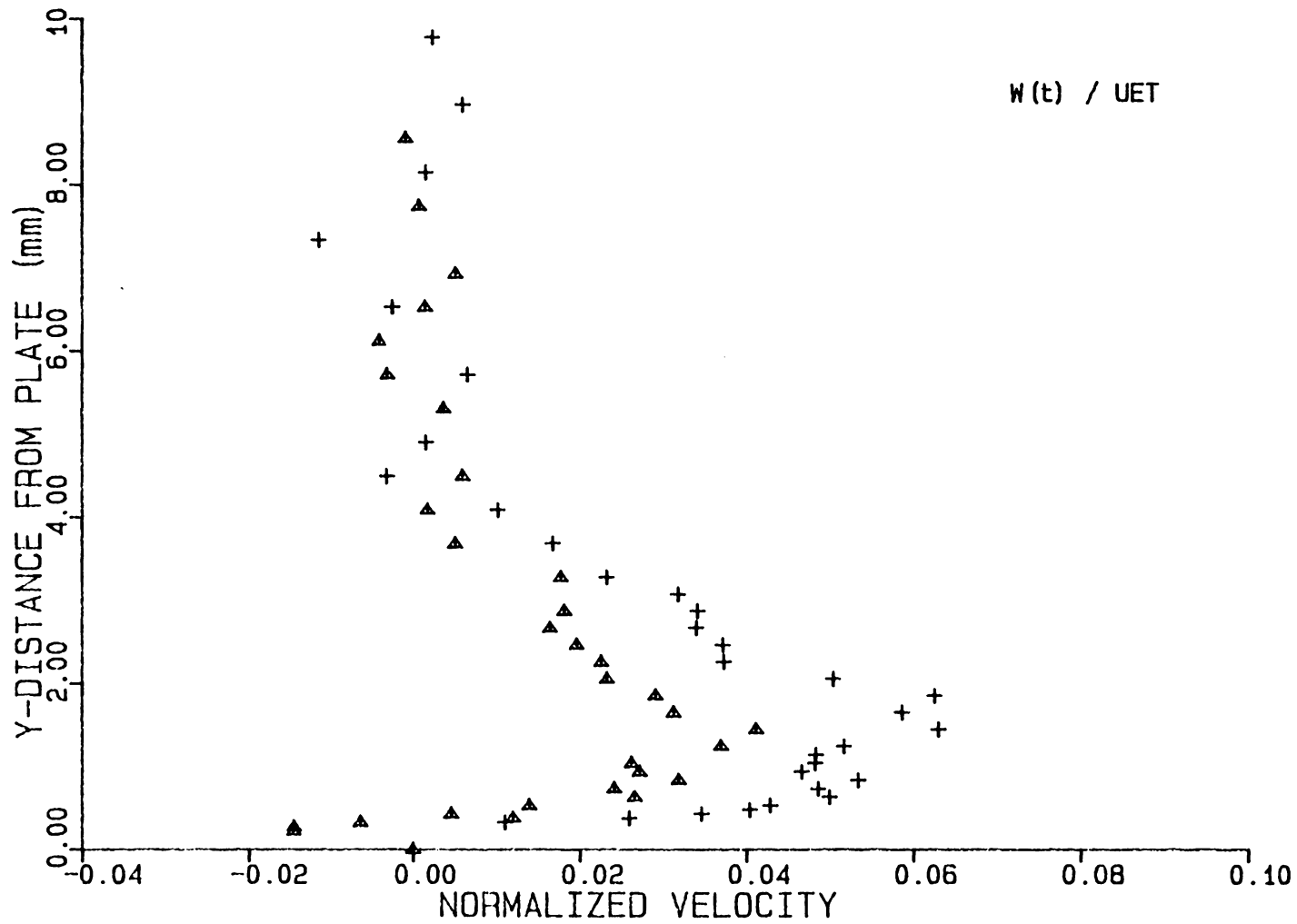


Figure 3.31 Crossflow velocity W_t/U_{et} at $x=100$ and 140 cm at a reference velocity of 14 m/s.

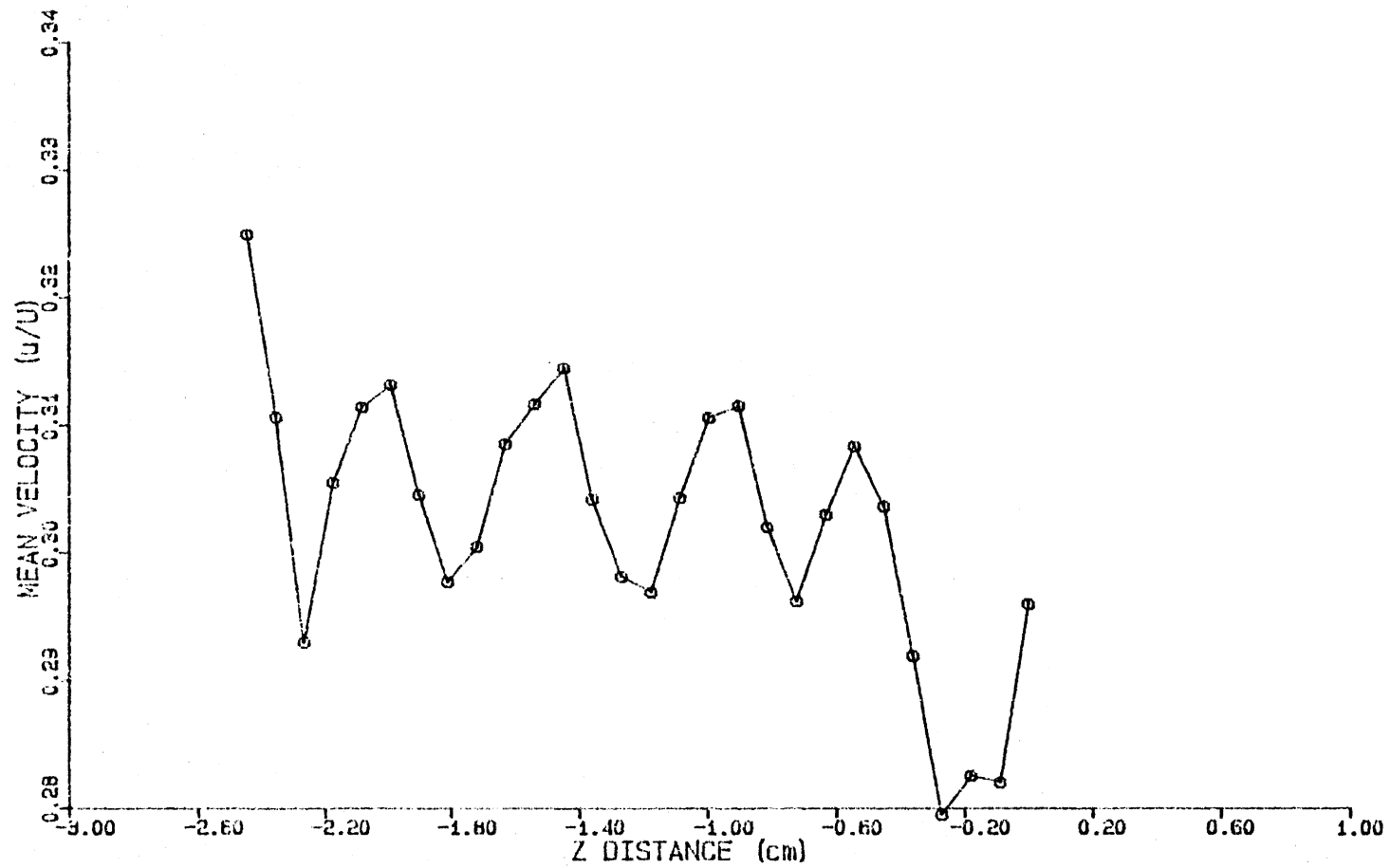


Figure 3.32 Spanwise variation of mean flow at $x=85$ cm.
Reference velocity of 10 m/s.

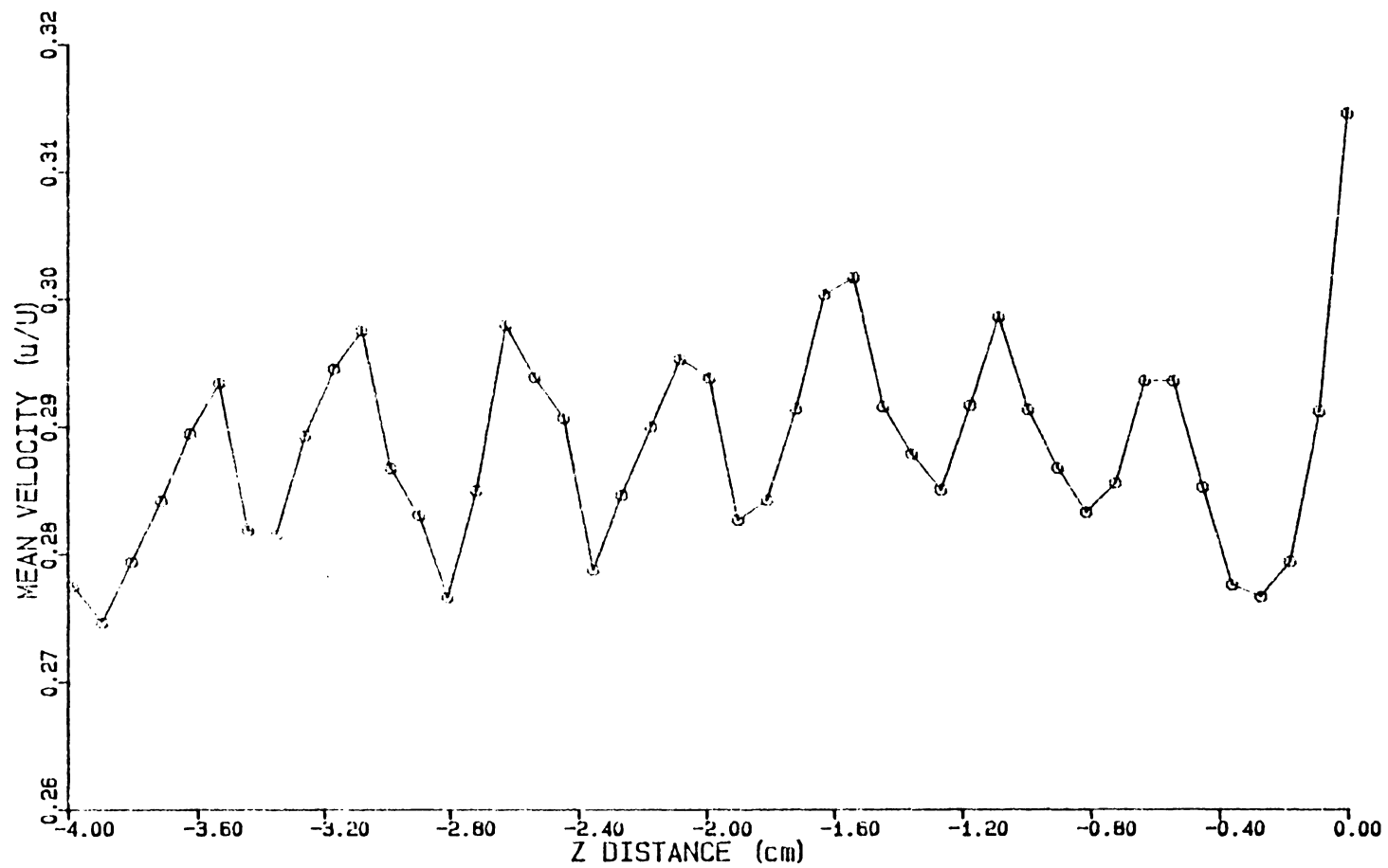


Figure 3.33 Spanwise variation of mean flow at $x=100$ cm.
Reference velocity of 10 m/s.

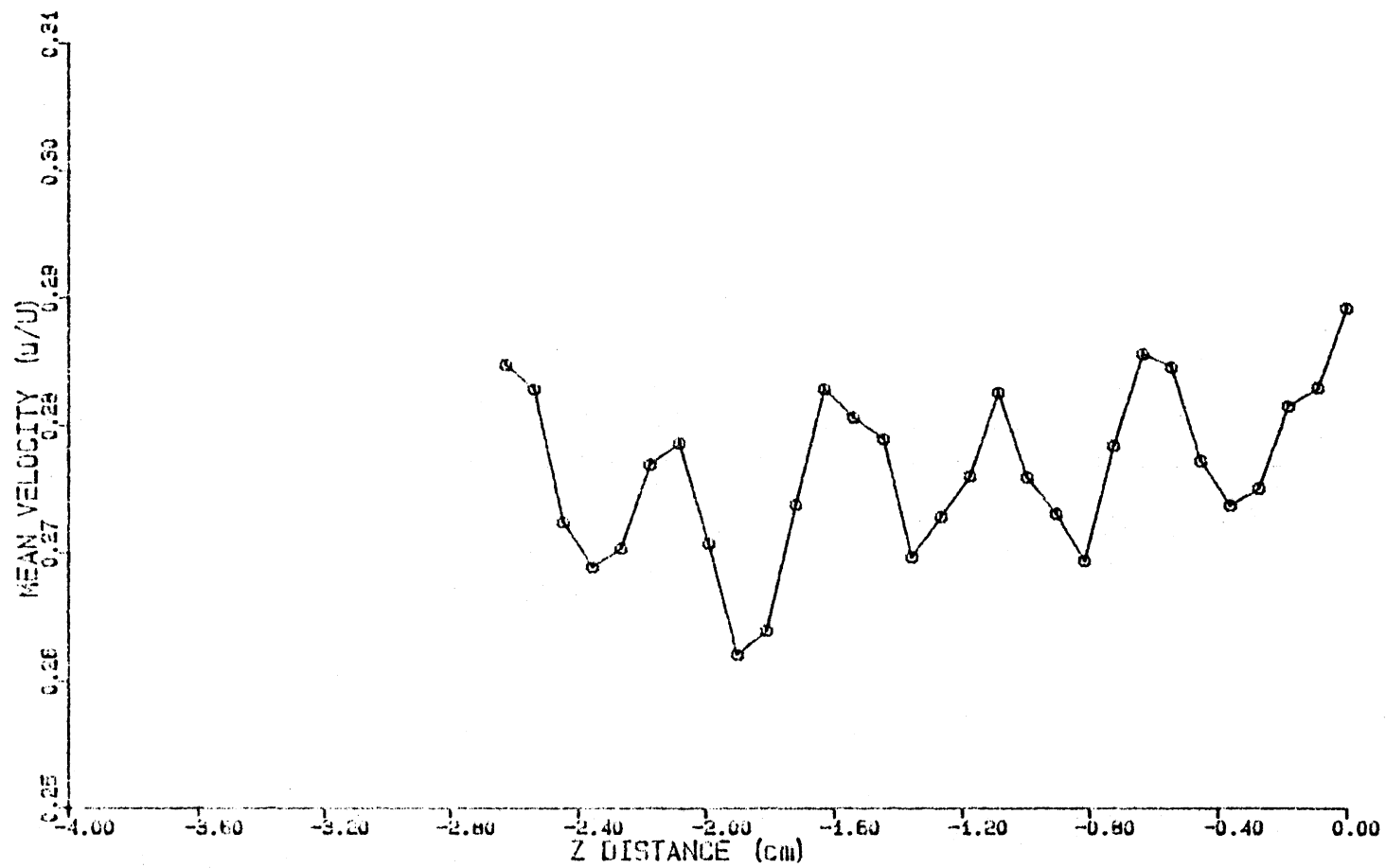


Figure 3.34 Spanwise variation of mean flow at $x=120$ cm.
Reference velocity of 10 m/s.

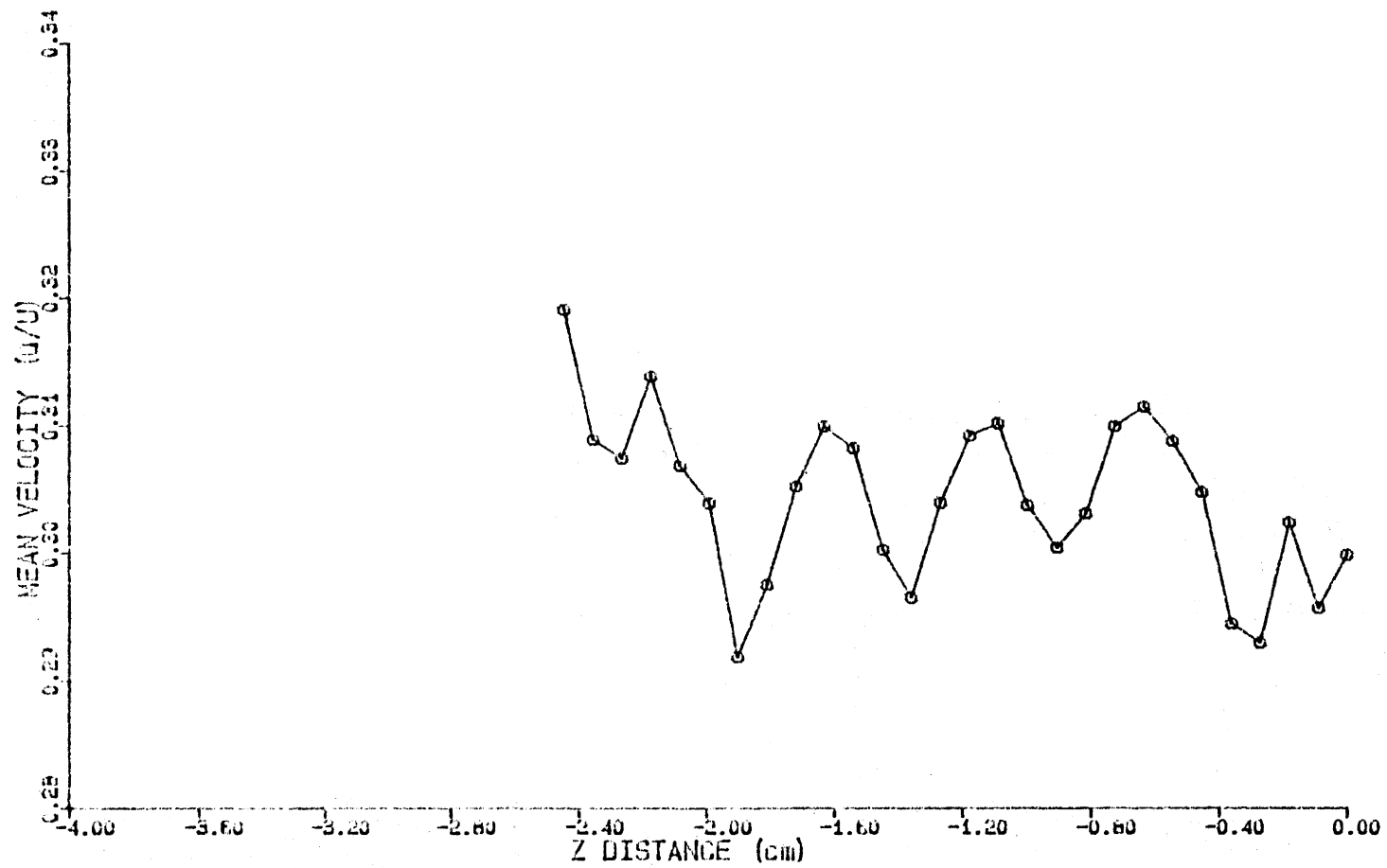


Figure 3.35 Spanwise variation of mean flow at $x=140$ cm.
Reference velocity of 10 m/s.

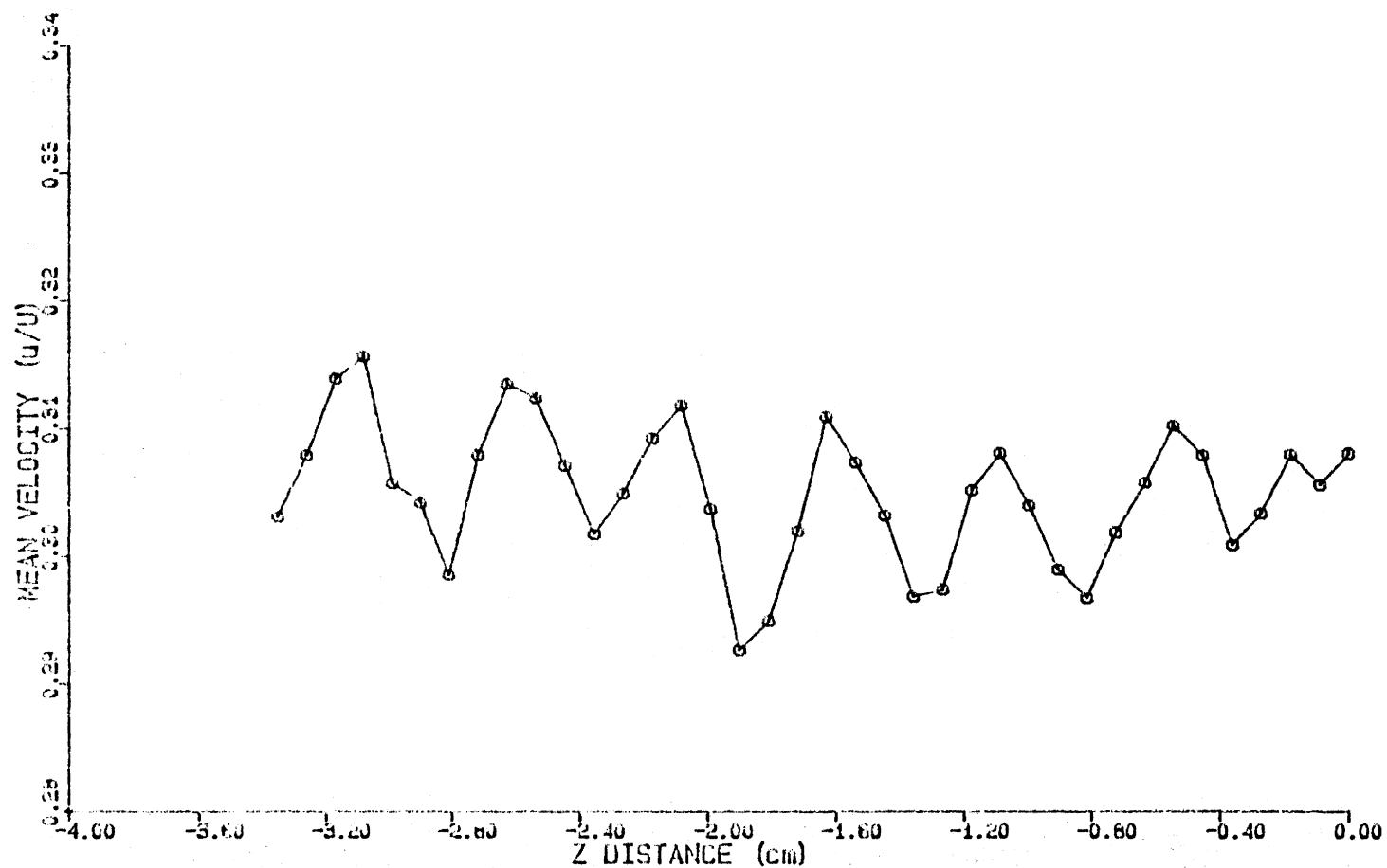


Figure 3.36 Spanwise variation of mean flow at $x=160$ cm.
Reference velocity of 10 m/s.

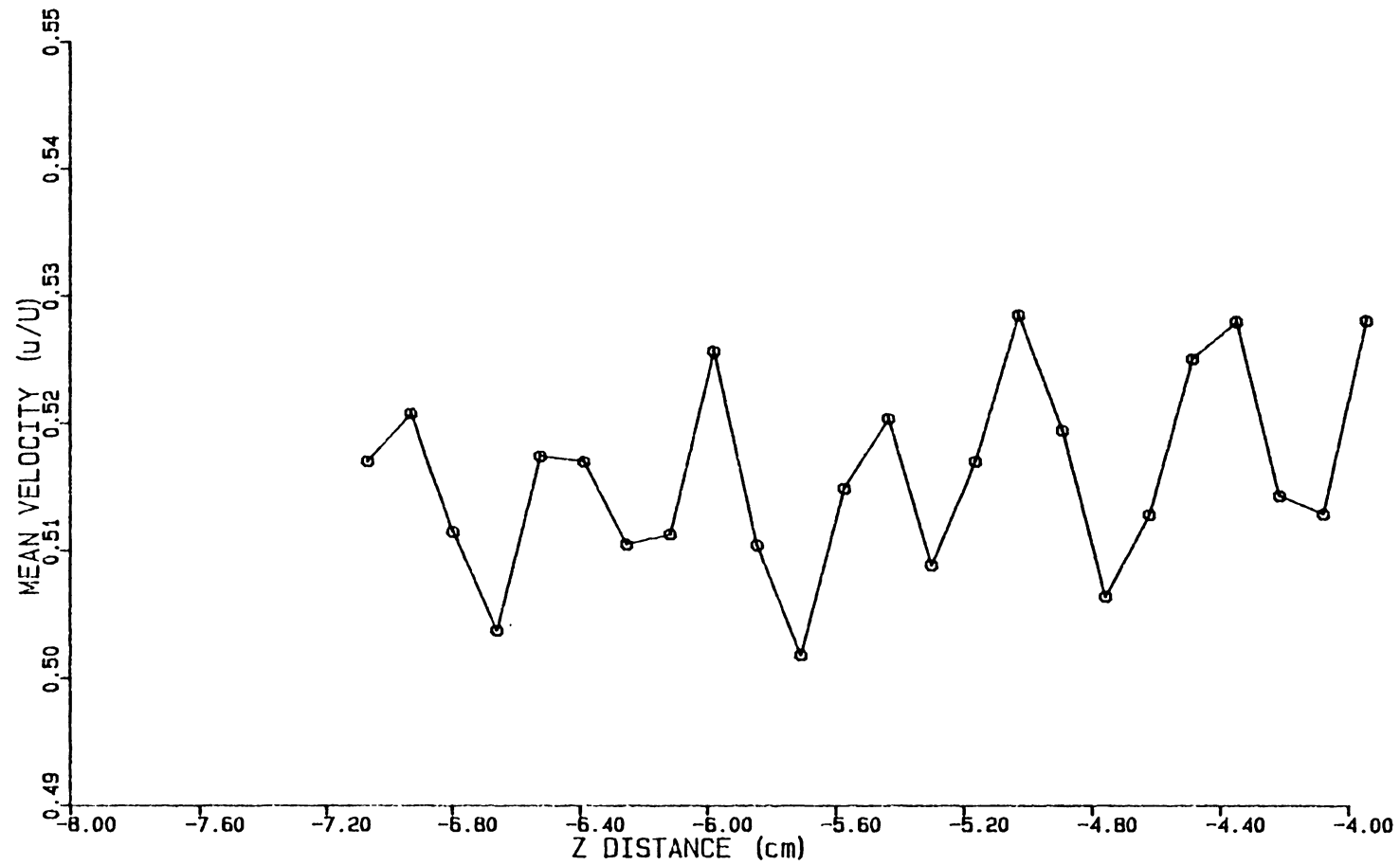


Figure 3.37 Spanwise variation of mean flow at $x=100$ cm.
Reference velocity of 14 m/s.

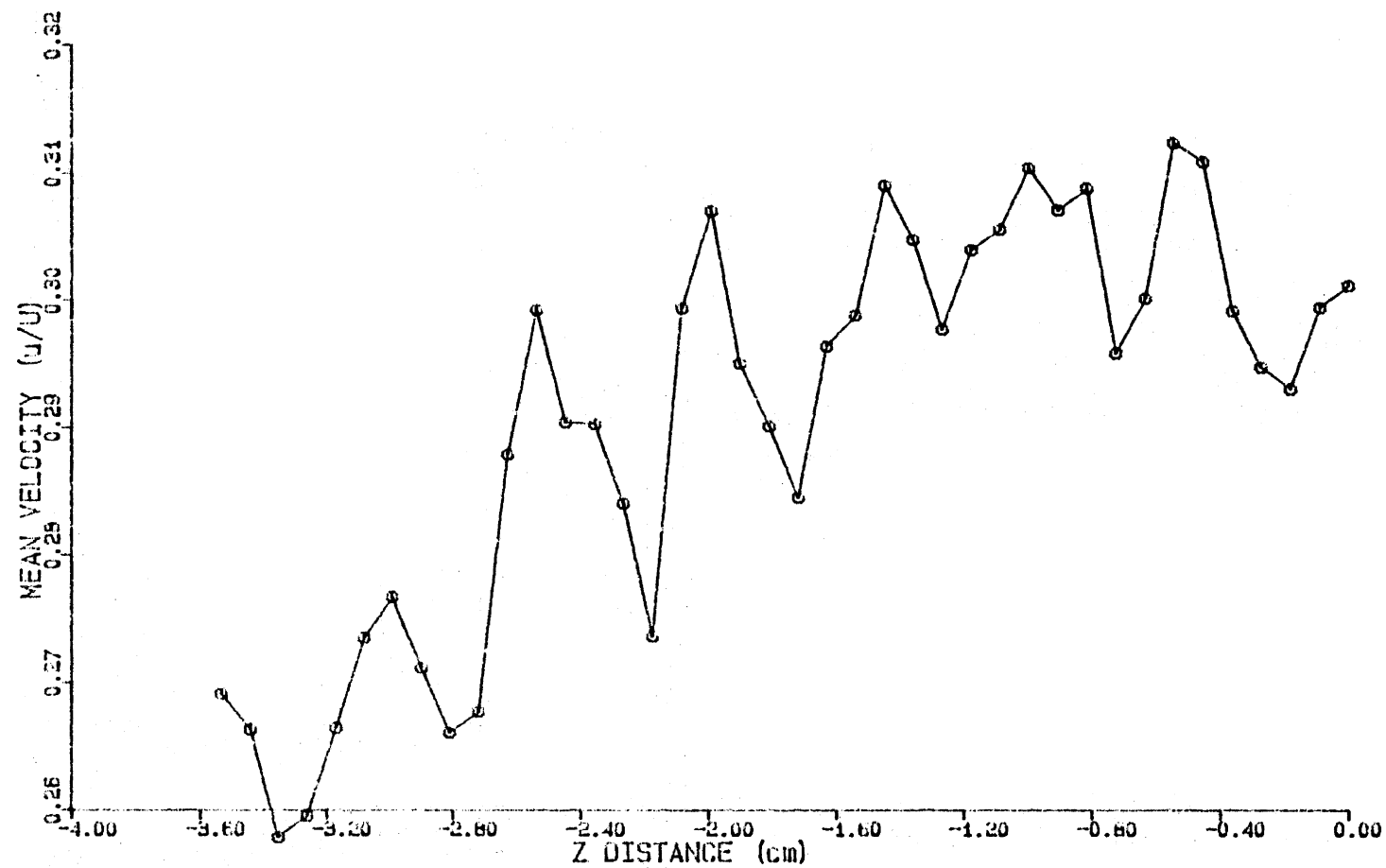


Figure 3.38 Spanwise variation of mean flow at $x=120$ cm.
Reference velocity of 14 m/s.

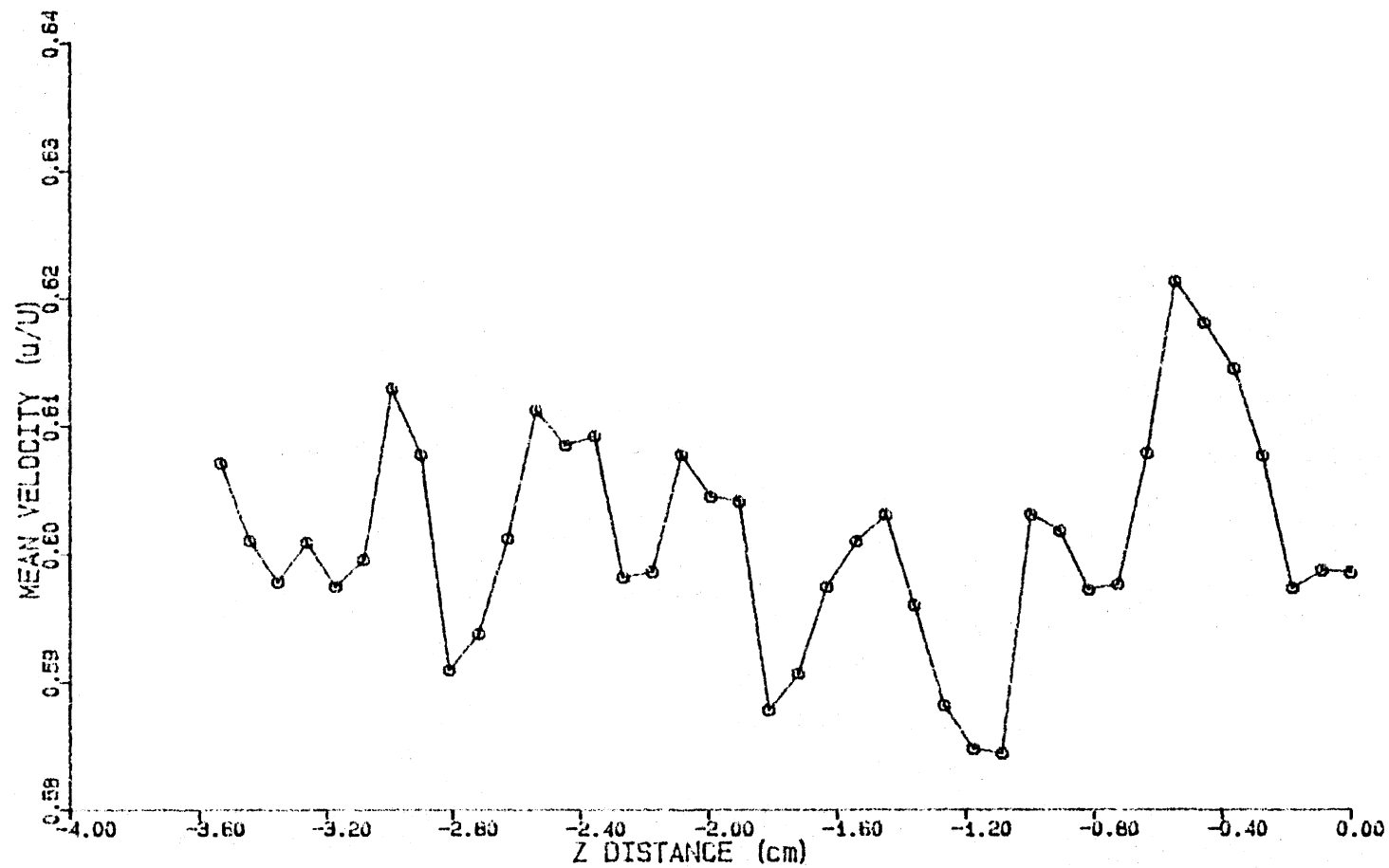


Figure 3.39 Spanwise variation of mean flow at $x=140$ cm.
Reference velocity of 14 m/s.

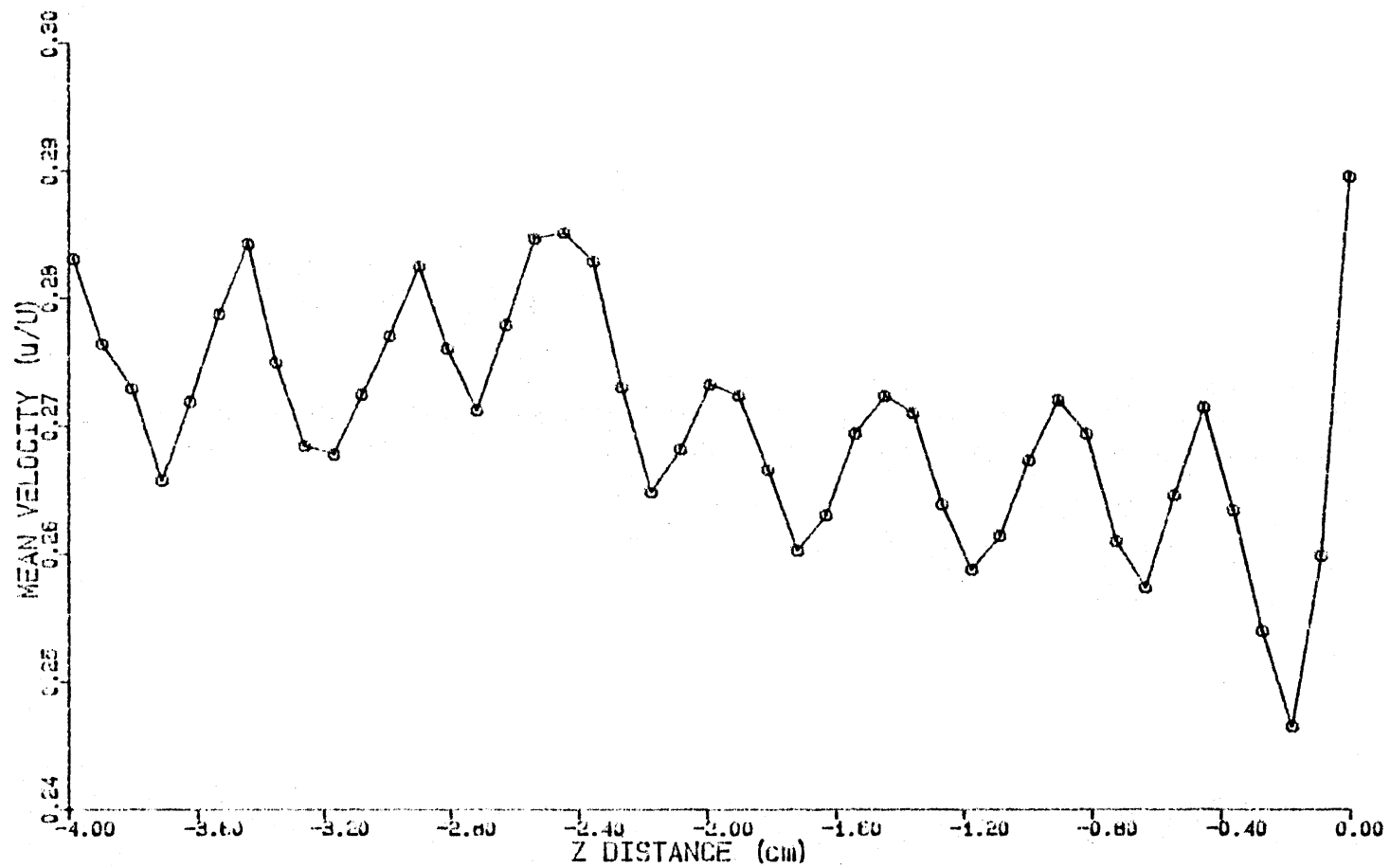


Figure 3.40 Spanwise variation of mean flow at $x=160$ cm.
Reference velocity of 14 m/s.

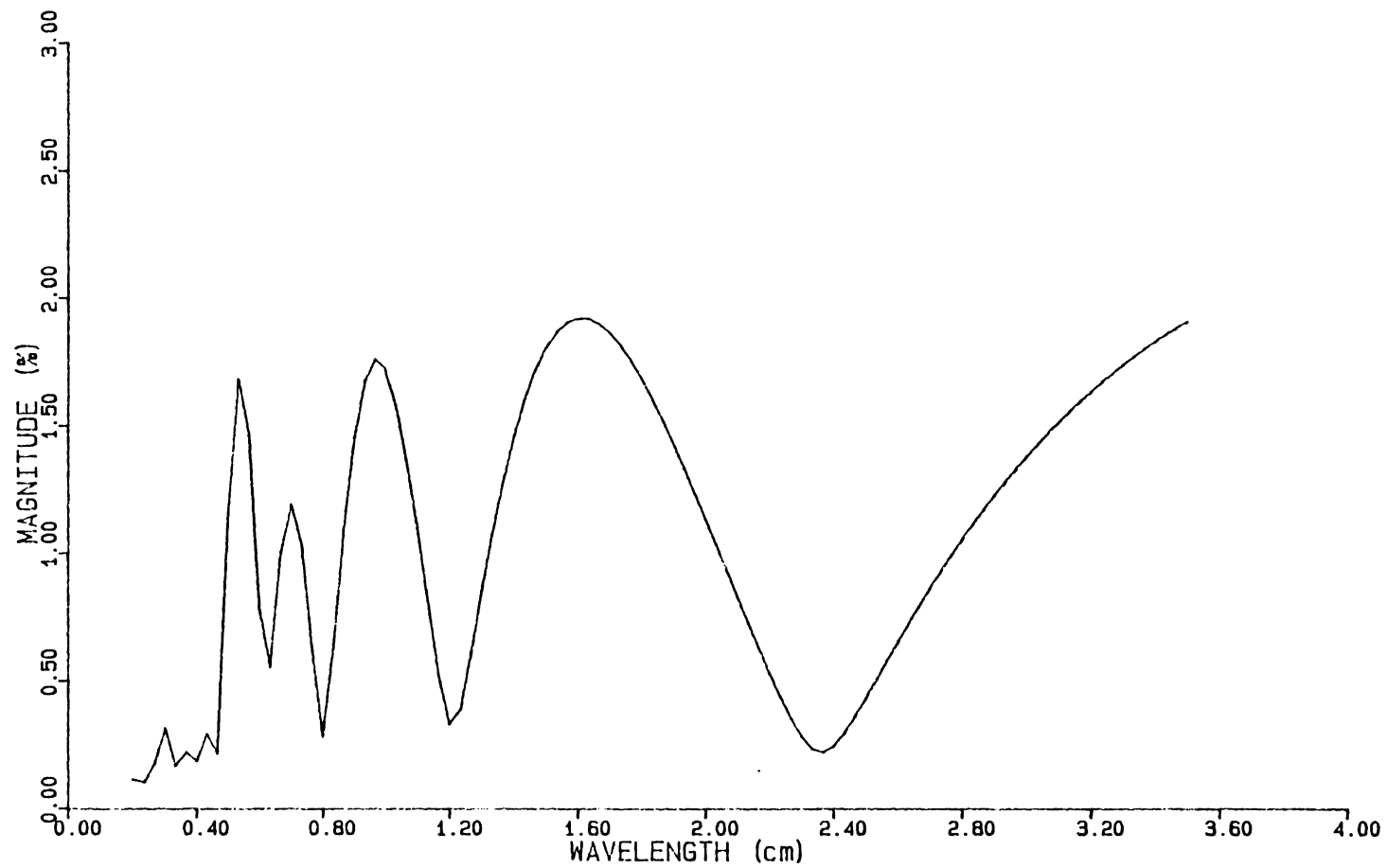


Figure 3.41 Spectra from disturbance measurements at $x=85\text{cm}$.
Reference velocity of 10m/s .

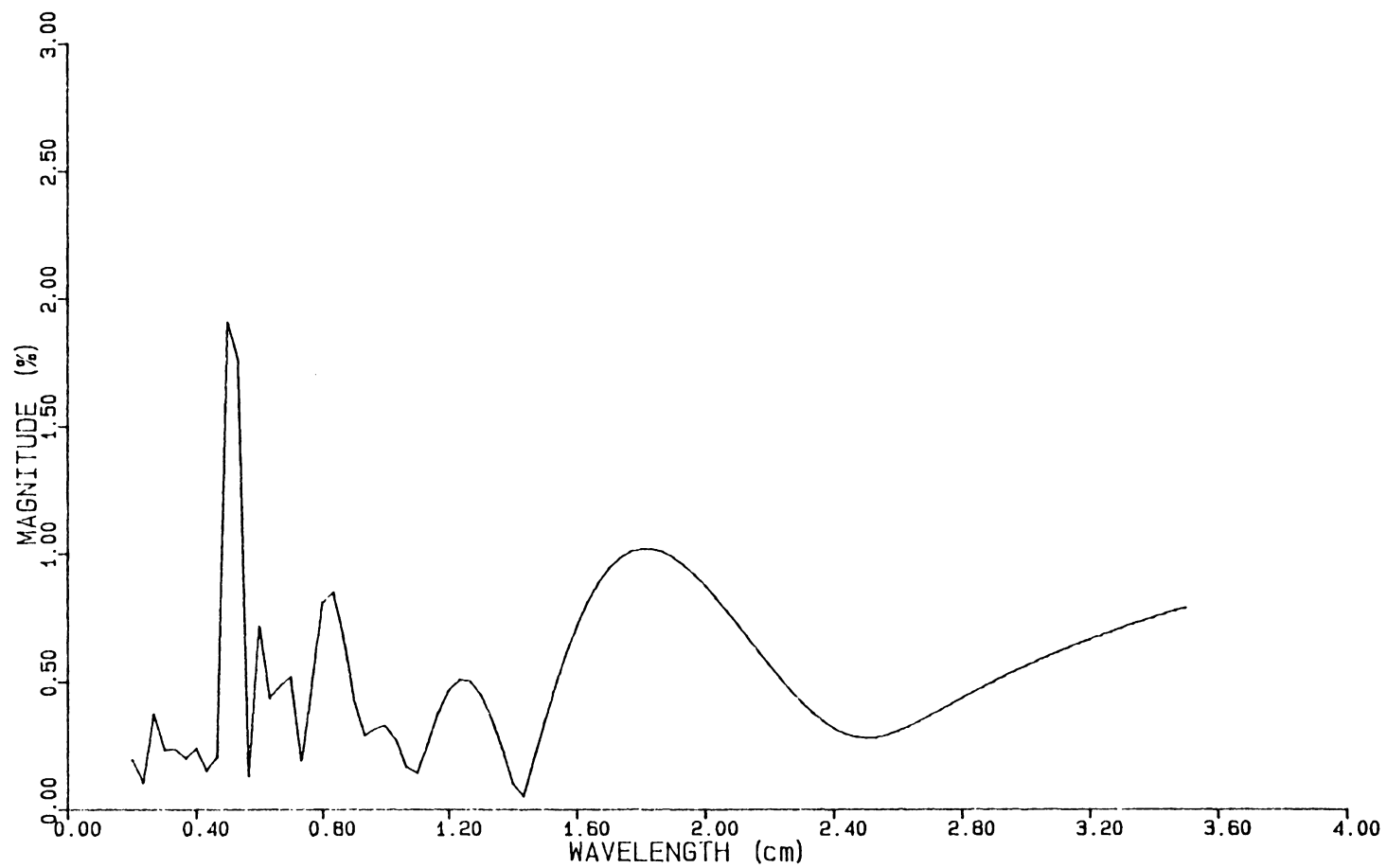


Figure 3.42 Spectra from disturbance measurements at $x=100\text{cm}$.
Reference velocity of 10m/s .

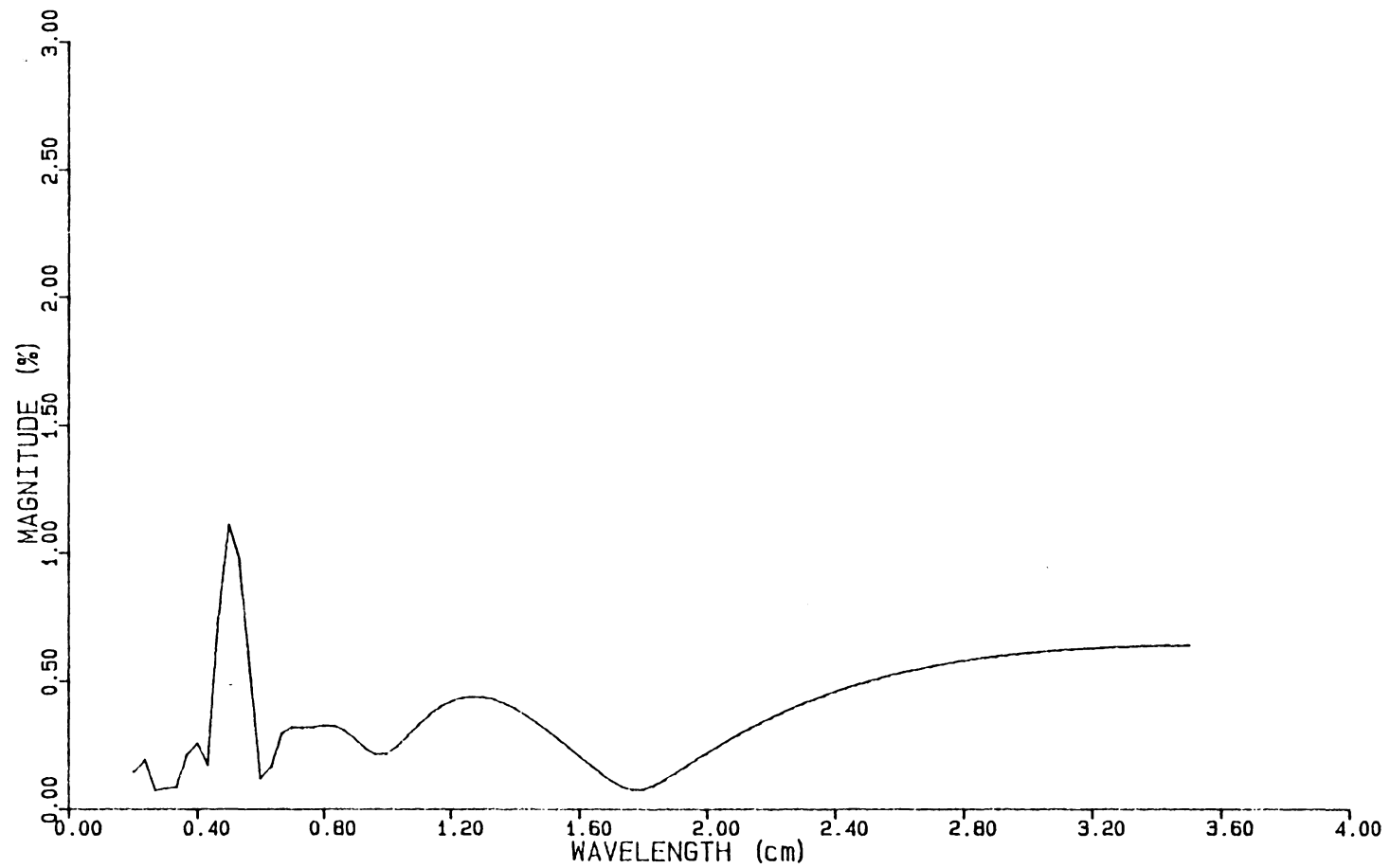


Figure 3.43 Spectra from disturbance measurements at $x=120\text{cm}$.
Reference velocity of 10m/s .

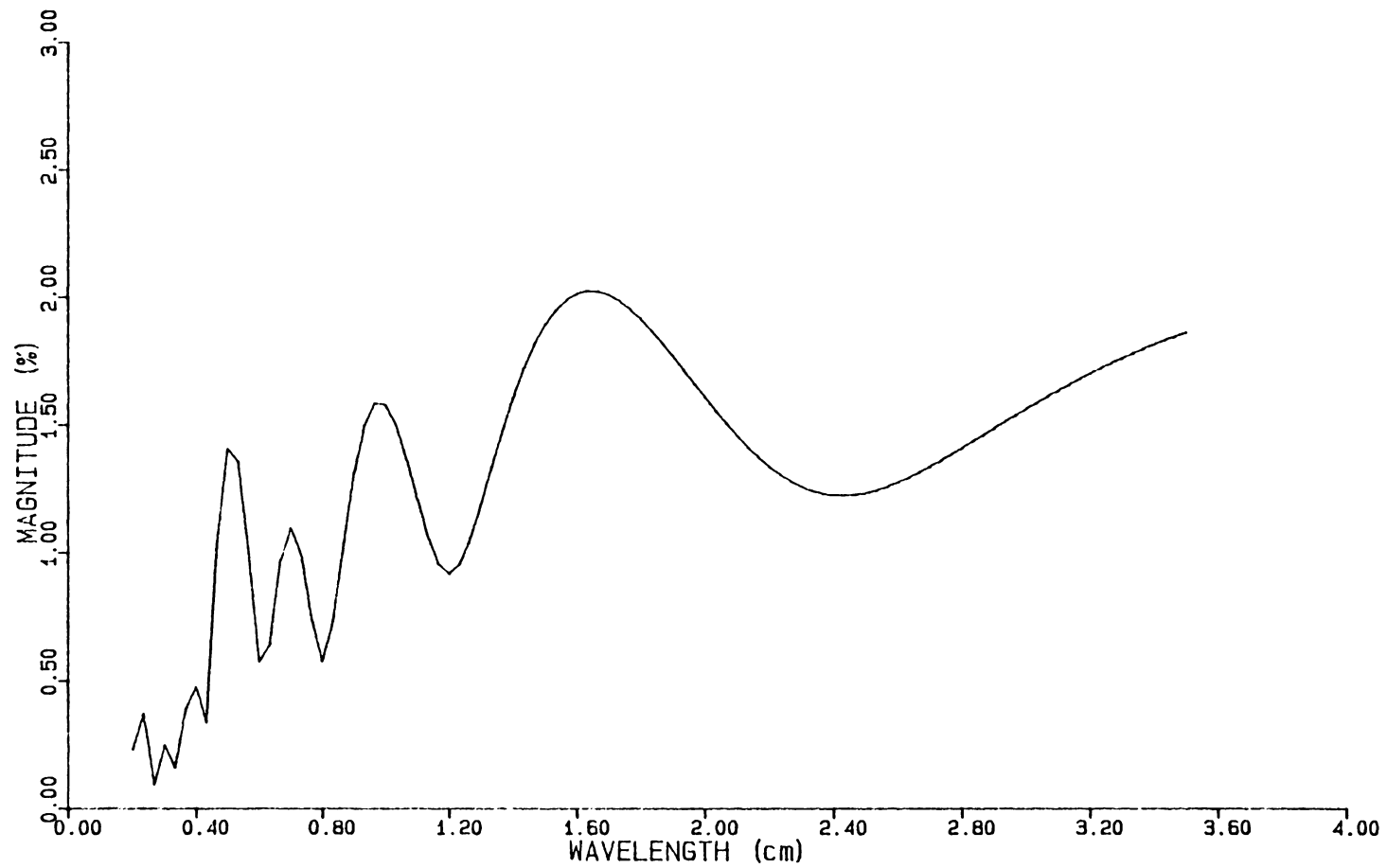


Figure 3.44 Spectra from disturbance measurements at $x=140\text{cm}$.
Reference velocity of 10m/s .

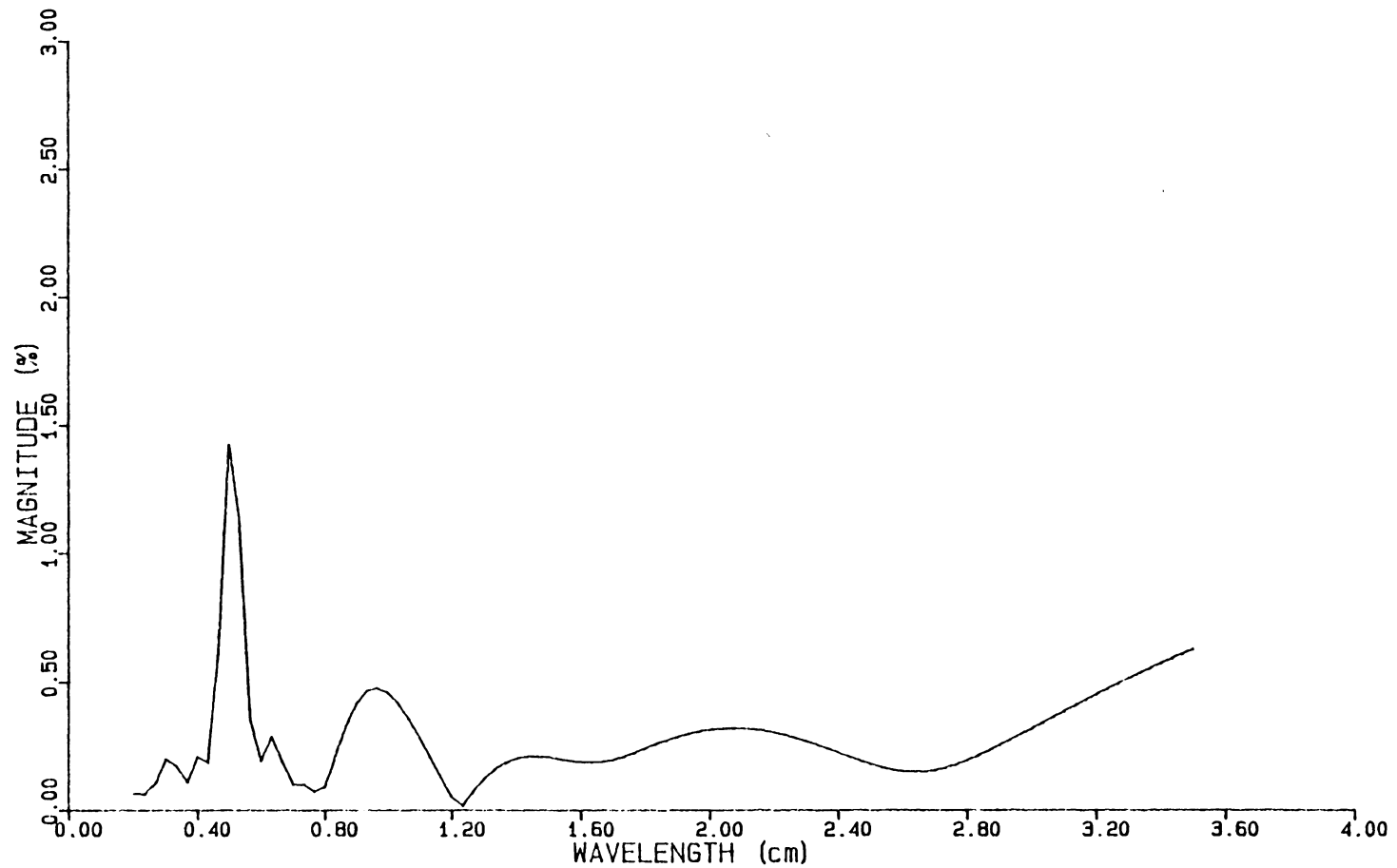


Figure 3.45 Spectra from disturbance measurements at $x=160\text{cm}$.
Reference velocity of 10m/s .

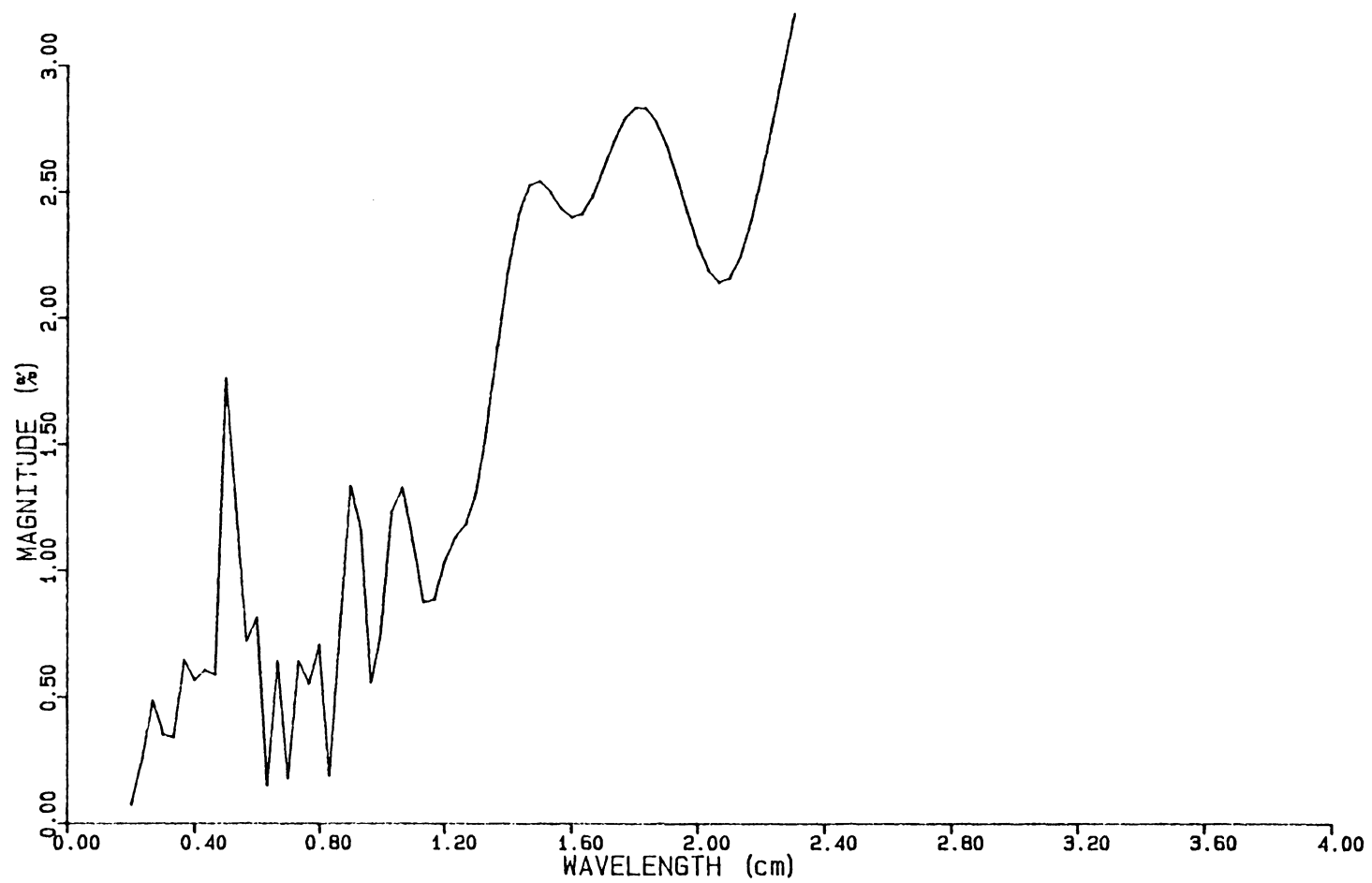


Figure 3.46 Spectra from disturbance measurements at $x=100\text{cm}$.
Reference velocity of 14m/s .

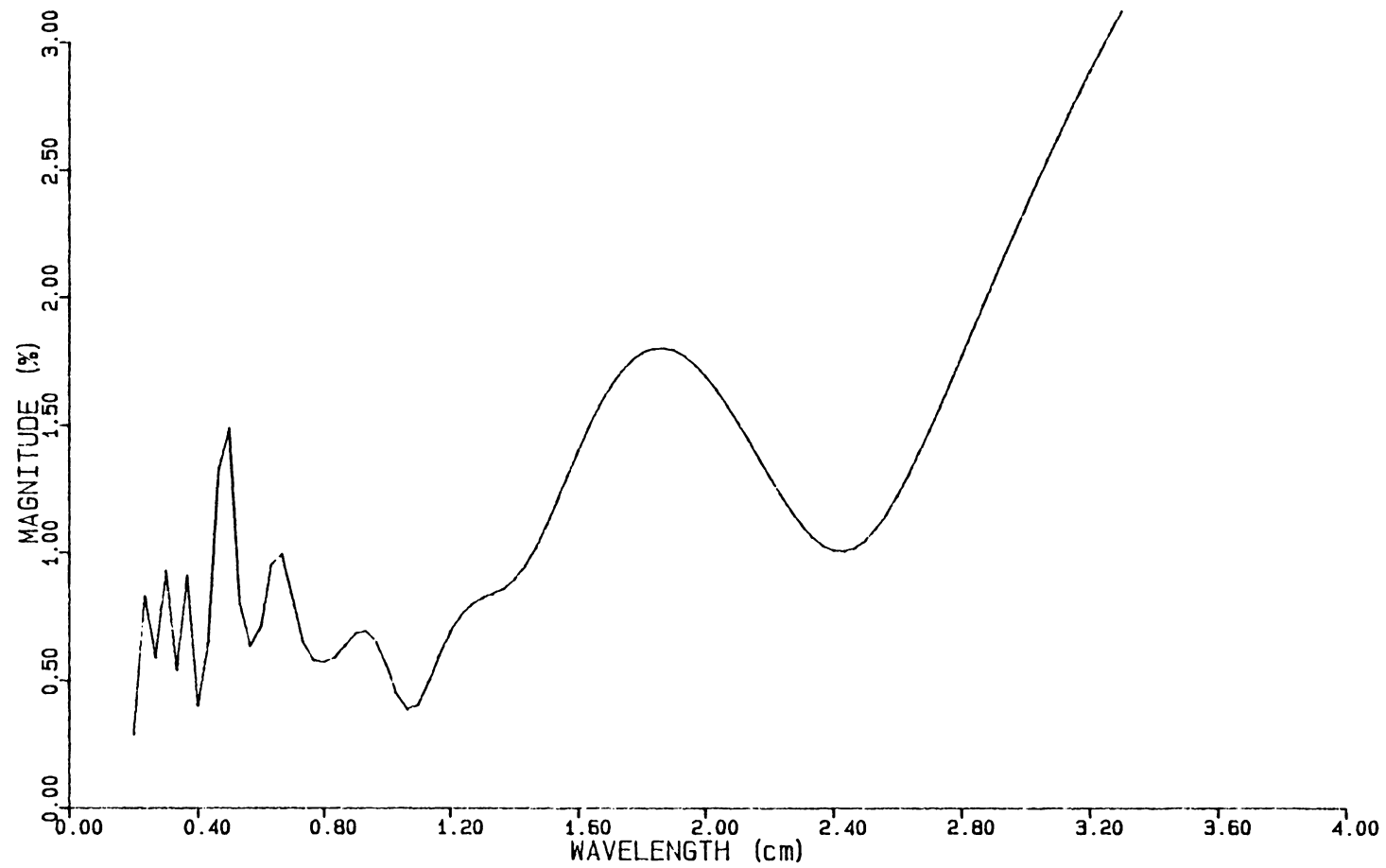


Figure 3.47 Spectra from disturbance measurements at $x=120\text{cm}$.
Reference velocity of 14m/s .

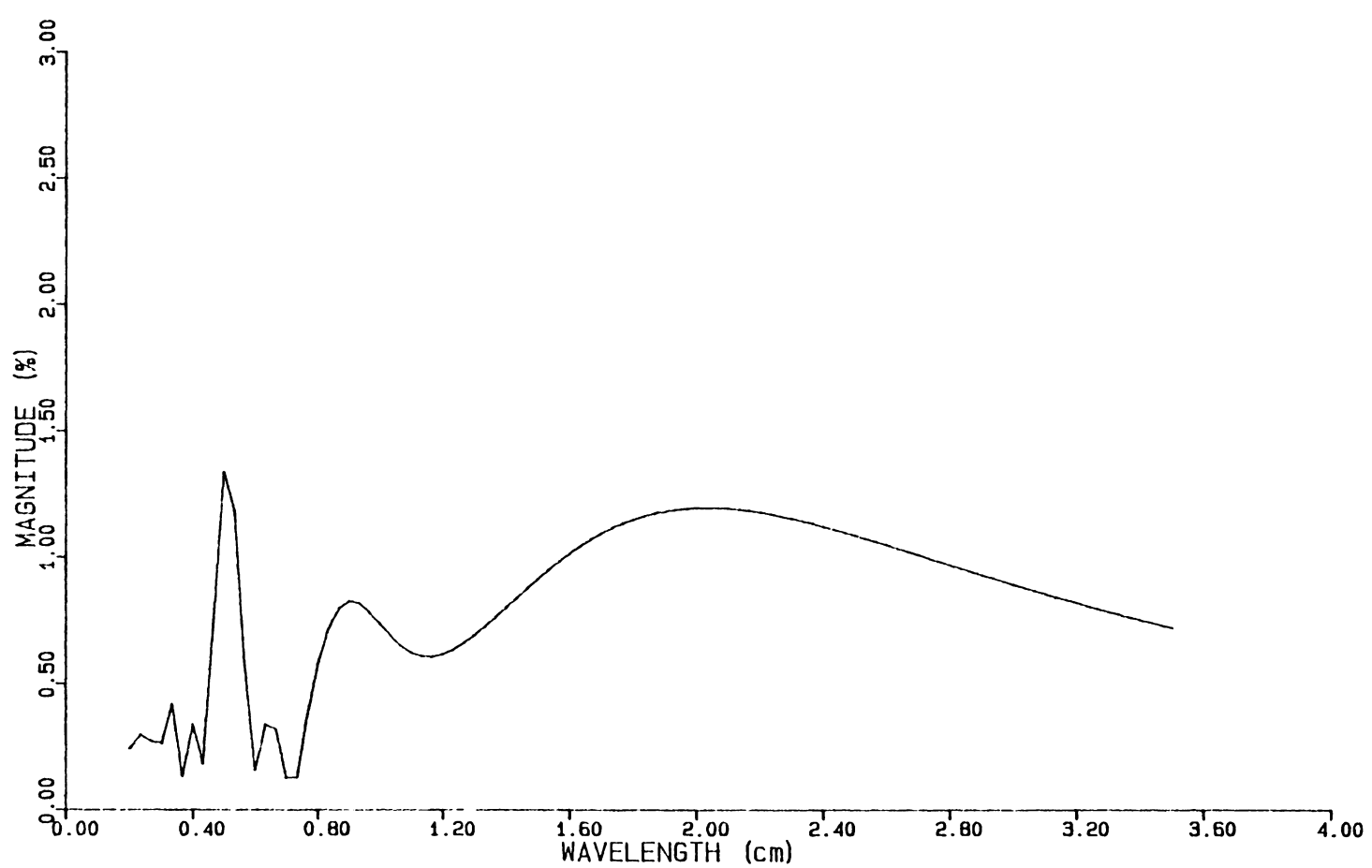


Figure 3.48 Spectra from disturbance measurements at $x=140\text{cm}$.
Reference velocity of 14m/s .

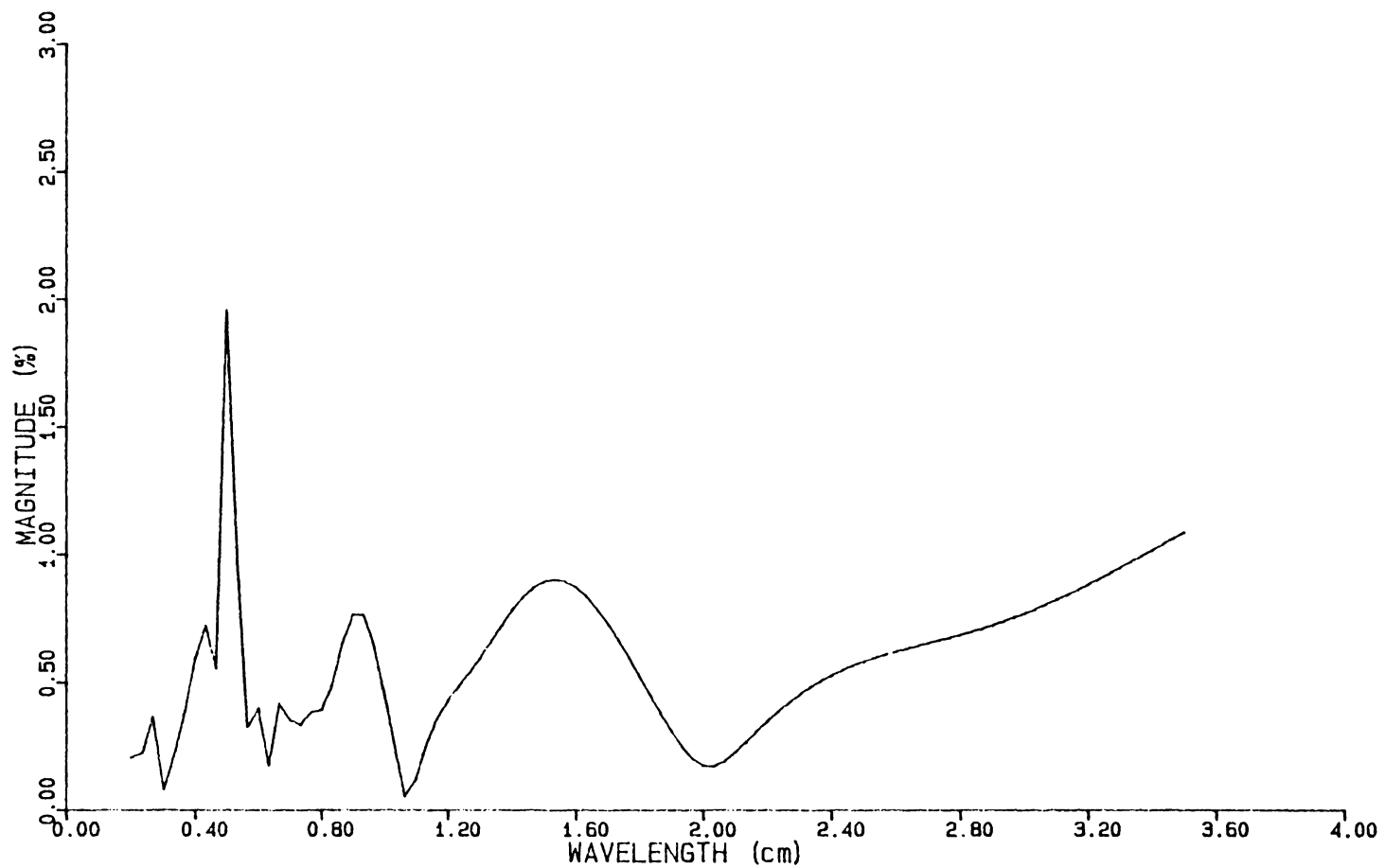


Figure 3.49 Spectra from disturbance measurements at $x=160\text{cm}$.
Reference velocity of 14m/s .

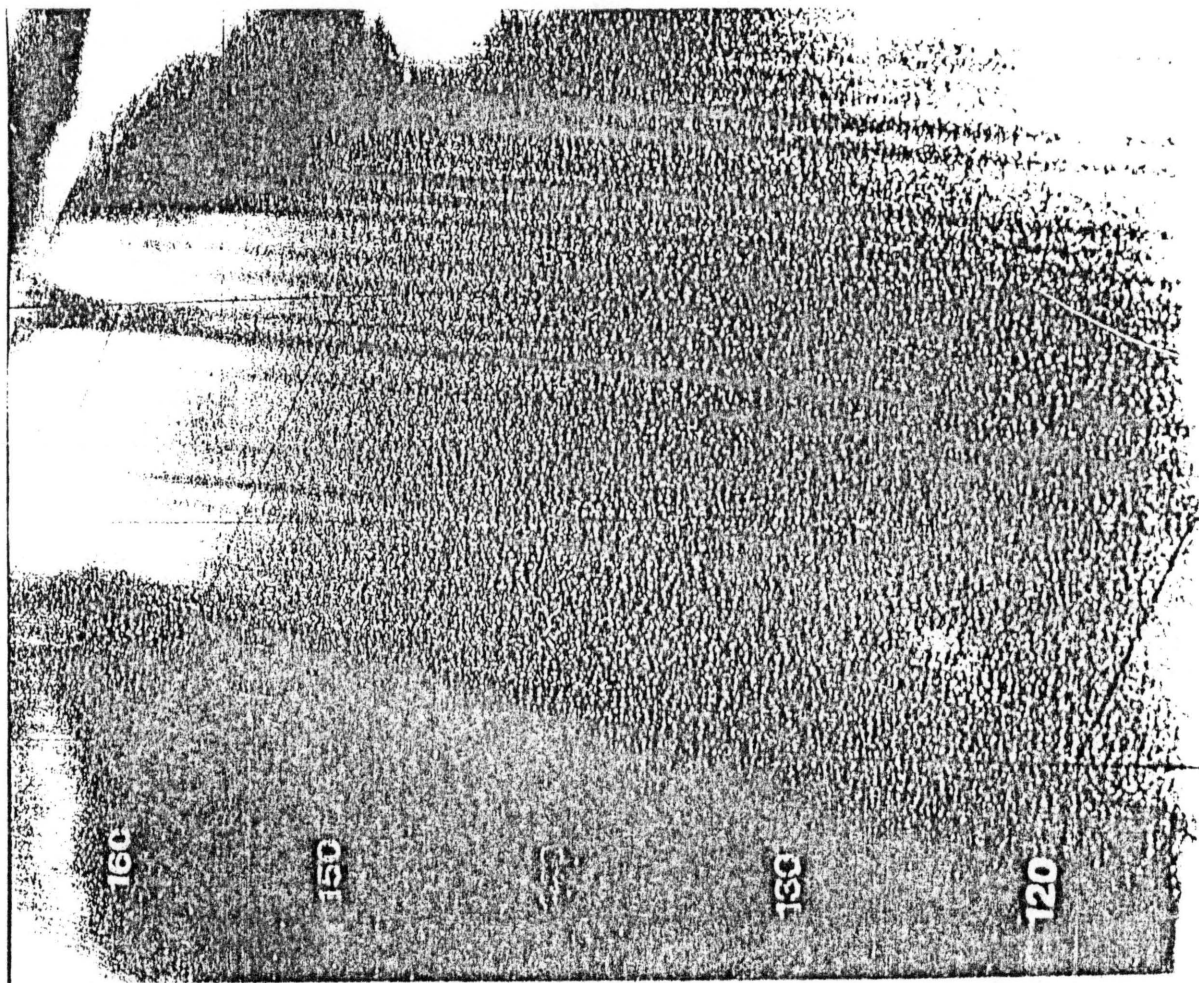


Figure 3.50 Naphthalene surface patterns. Flow from right to left.

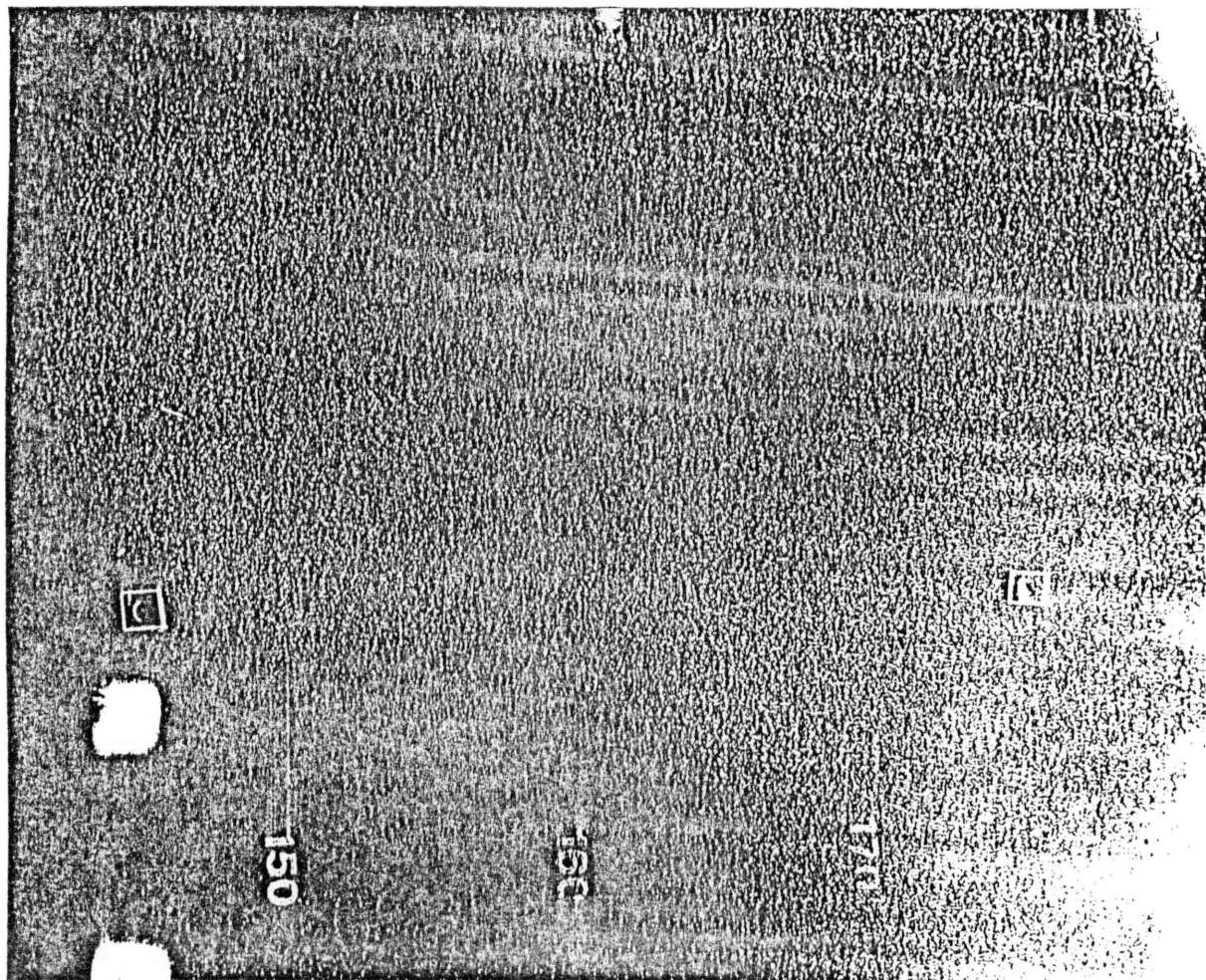


Figure 3.51 Naphthalene surface patterns. Flow from left to right.

**The vita has been removed from
the scanned document**